CONTROL OF A VARIABLE SHAFTSPEED WIND ENERGY CONVERSION AND BATTERY STORAGE SYSTEM

by

Harvey Roy Simkovits

S.B., Massachusetts Institute of Technology
(1976)

SUBMITTED IN PARTIAL FULFILLMENT OF THE

REQUIREMENTS FOR THE DEGREE OF

MASTER OF SCIENCE

at the

MASSACHUSETTS INSTITUTE OF TECHNOLOGY

September, 1977

Signature redacted

Signature of Author.....
Department of Electrical Engineering and Computer Science
July 8, 1977

Signature redacted

Certified by.....
Thesis Supervisor

Accepted by.....
Chairman, Departmental Committee on Graduate Students

CONTROL OF A VARIABLE SHAFTSPEED WIND ENERGY CONVERSION AND BATTERY STORAGE SYSTEM

by

Harvey Roy Simkovits

Submitted to the Department of Electrical Engineering and Computer Science on July 8, 1977 in partial fulfillment of the requirements for the Degree of Master of Science.

ABSTRACT

The design of an efficient wind energy conversion and battery storage system is presented. A detialed model of this windmill power system is constructed and then implemented on a digital computer to predict the steady-state and dynamic behavior of the system. The computer simulation is also employed to determine effective control algorithms for the system. Finally, the construction of a physical model windmill power system using a dc motor as a windmill simulator validates the behavior predicted by the computer model.

THESIS SUPERVISOR: John G. Kassakian

TITLE: Assistant Professor of Electrical Engineering

ACKNOWLEDGEMENTS

The author gratefully acknowledges the material support of this research provided by the Gould Foundation.

Much gratitude is also expressed to Professor John G. Kassakian for his enthusiasm, guidance and support in all facets of the project.

Lastly, I wish to thank all the members of EPSEL for their help and friendship during my association with them.

TABLE OF CONTENTS

	Page
TITLE PAGE	1
ABSTRACT	2
ACKNOWLEDGEMENTS	3
TABLE OF CONTENTS	4
LIST OF FIGURES	7
LIST OF TABLES	11
BACKGROUND AND INTRODUCTION	12
CHAPTER I SYSTEM DESCRIPTION AND MODELING	15
I.1 Windmill Characteristics	15
I.1.a Wind Power Extraction	15
I.1.b Windmill Power Loss Characterization	19
I.2 Generator and Load Characteristics	20
I.2.a Battery Characteristics	20
I.2.b Generator and Charging Circuit Characteristics	20
I.2.c Battery Charging Circuit Analysis	21
I.2.d Generator Power Loss Characterization	33
I.2.e Other Methods of Generator Load Control	35
(i) Generator Winding Switching	35
(ii) Rectifier Phase Control	40
CHAPTER II PHILOSOPHY OF WINDMILL POWER SYSTEM CONSTRUCTION AND COUPLED SYSTEM CONTROL AND BEHAVIOR	44
II.1 Windmill Power System Construction	44
II.2 Power System Steady-State Analysis	56
II.3 Power System Dynamic Analysis	65

	Page
CHAPTER III COMPUTER SIMULATION OF STEADY-STATE AND DYNAMIC BEHAVIOR OF WINDMILL POWER SYSTEM	73
III.1 Steady-State Windmill Power System Simulation	73
III.2 Dynamic System Simulation	93
III.2.a System Dynamics Associated with Changes in Wind Velocity	93
III.2.b System Dynamics Associated with Battery Load Switching	100
(i) Battery Switching Decision	100
(ii) Battery Switching Dynamics	106
III.2.c Summary and Conclusion of Dynamic Investigation	111
CHAPTER IV WINDMILL POWER SYSTEM CONTROL IMPLEMENTATION	113
VI.1 Control System Circuit Implementation	114
IV.1.a Analog-Control Implementation	115
IV.1.b Implementation of Battery Section Rotation and Battery Voltage Switching	121
IV.2 Control Circuitry Test Results	130
IV.3 Summary	137
CHAPTER V PHYSICAL SCALE MODEL SIMULATION OF STEADY-STATE AND DYNAMIC BEHAVIORS OF THE WINDMILL POWER SYSTEM	139
V.1 Steady-State Behavior of the Physical Model System	139
V.2 Dynamic Behavior of Physical Model System	154
V.2.a Dynamics Associated with Wind Velocity Changes	154
V.2.b Dynamics Associated with Battery Voltage Switching	160
APPENDIX A WINDMILL POWER SYSTEM DESCRIPTION AND WINDMILL MODELING	166

	Page
APPENDIX B PHYSICAL SCALE MODEL SYSTEM DESIGN	169
B.1 Generator Characteristics and the Choice of Base Quantities for the Windmill Power System	169
B.2 Battery Bank Design	173
B.3 Windmill Design	175
APPENDIX C BATTERY BANK DESCRIPTION AND CHARACTERISTICS	181
APPENDIX D WINDMILL SIMULATION AND SIMULATOR CHARACTERISTICS	186
D.1 Windmill Simulation	186
D.2 Motor Specifications and Choice of Base Quantities	190
D.3 Motor Power Loss Measurements	192
APPENDIX E GENERATOR POWER LOSS MEASUREMENTS	200
E.1 Mechanical Power Losses	200
E.2 Magnetic-Core Losses	202
E.3 Stray Losses	204
APPENDIX F DYNAMIC SYSTEM COMPUTER SIMULATION	208
APPENDIX G SMOOTHING CHOKE INDUCTANCE CALCULATION	217
REFERENCES	222

LIST OF FIGURES

		Page
Figure 1	Typical Windmill C_p Curve and Analytic Approximation	17
Figure 2	Wind Power Extraction as a Function of Shaftspeed and Wind Velocity	18
Figure 3	Single-Phase Battery Charging Circuit	22
Figure 4	Generalized Battery Charging Circuit Model	26
Figure 5	Complex Phasor Diagram of Generalized Circuit Model	30
Figure 6	Generator Power-Speed Characteristics as a Function of the Number of Charging Battery Sections	32
Figure 7	Charging Circuit Model for Machine with Multi-Voltage Armature	37
Figure 8	Power-Speed Characteristic for Multivoltage Generator	39
Figure 9	Complex-Phasor Diagram of a Phase-Control Bridge Circuit	41
Figure 10	Power-Speed Characteristics for Phase-Controlled Rectifier	41
Figure 11	Power System Characteristics at Rated Wind Velocity	51
Figure 12	Redesigned Windmill System	55
Figure 13	Schematic Diagram of Windmill Control System	69
Figure 14	Schematic Diagram of Augumented Windmill Control System	71
Figure 15	Generator Input and Output Characteristics	78
Figure 16	Generator Power Output and Stored Battery Power as a Function of Operating Wind Velocity for a Nominally Charged Battery Bank	81
Figure 17	System Operating and Extraction Efficiency as a Function of Operating Wind Velocity	83

		Page
Figure 18	Generator Power and Stored Battery Power as a Function of Wind Speed for a Low State-of-Charge Battery Bank	86
Figure 19	System Operating and Extraction Efficiencies as a Function of Wind Velocity for a Low State-of-Charge Battery Bank	87
Figure 20	Generator Power Output and Stored Battery Power as a Function of Wind Velocity for a High State-of-Charge Battery Bank	88
Figure 21	Generator Power Output and Stored Battery Power as a Function of Windspeed for a High State-of-Charge Battery Bank	89
Figure 22	Desired Operating Sahftspeed as a Function of Wind Velocity for Different Battery States-of-Charge	92
Figure 23	Shaftspeed Dynamics Associated with a 0.1 p.u. Step in Wind Velocity Initiated from a Speed of 0.6 p.u. for Four Values of τ_f	95
Figure 24	Shaftspeed Dynamics for a 0.1 p.u. Step in Wind Velocity with τ_f=0.5. Initial Wind Speed is Indicated on the Curves	97
Figure 25	Shaftspeed Dynamics for a 0.1 Step for Three Different Curvatures of the C_p Characteristic. Initial Windspeed is 0.7 p.u. For These Simulations, τ_f=1 sec.	99
Figure 26	System Dynamics for an Oscillating Wind Condition Centered Around v_w=0.81 p.u. with Amplitude 0.05 p.u. and Frequency 0.15/sec. For this simulation, τ_f = 1 sec.	103
Figure 27	Shaftspeed and Field Current Dynamics at the Occurrence of Battery Voltage Incrementation. Dynamics for Two Values of τ_f are Shown where Switching is Initiated by a Step in Wind	107
Figure 28	Shaftspeed and Field Current Dynamics at the Occurrence of Battery Voltage Incrementation. Dynamics are for Two Values of τ_f where Switching is Initiated by a Ramp in Wind	109
Figure 29	System Dynamics at the Occurrence of Battery Voltage Decrementation. Battery Switching is Initiated by a Decreasing Wind Velocity	110

		Page
Figure 30	Implemented Analog Control Circuitry	116
Figure 31	Battery Charging Circuit Showing Six SCR's to be Controlled	122
Figure 32	Implemented Logic Circuit	125
Figure 33	Implemented Logic Circuit	126
Figure 34	Decoding Logic and SCR Switch Implementation	131
Figure 35	Decoding Logic and SCR Switch Implementation	132
Figure 36	Generator Armature Current at the Occurrence of Battery Switching	134
Figure 37	Armature Current Limiter Dynamics	136
Figure 38	Measure Generator Power Output and Stored Battery Powers as a Function of Wind Velocity for a Nominally Charged Battery Bank	140
Figure 39	Measured System Operating and Extraction Efficiency as a Function of Wind Speed for a Nominal State-of-Charge Battery Bank	141
Figure 40	Measured Generator Output and Stored Battery Power as a Function of Wind Velocity for a Low State-of-Charge Battery Bank	147
Figure 41	Measured Operating and Extraction Efficiencies as a Function of Wind Speed for a Low State-of-Charge Battery Bank	148
Figure 42	Measured Generator Power Output and Stored Battery Power as a Function of Wind Speed for a High State-of-Charge Battery Bank	149
Figure 43	Measured System Operating and Extraction Efficiencies as a Function of Wind Velocity for a High State-of-Charge Battery Bank	150
Figure 44	Measured and Calculated Desired Shaftspeed as a Function of Wind Velocity	153
Figure 45	Shaftspeed and Field Current Dynamics for a 0.1 Step in Wind Speed from an Initial Speed of 0.7 p.u. The Value for τ_f is Marked for Each Case	156

		Page
Figure 46	Shaftspeed and Field Current Dynamics for a 0.1 Step in Wind Velocity from an Initial Speed of 0.9 p.u. for Two Charging Sections	159
Figure 47	Shaftspeed and Field Current Dynamics at the Occurrence of Battery Voltage Incrementation. Dynamics Shown are for Two Values of τ_f where Switching is Initiated by a Step in Wind	162
Figure 48	Shaftspeed and Field Current Dynamics at the Occurrence of Battery Voltage Decrementation. Battery Switching is Initiated by a Step Decrease in Wind Speed	164
Figure A.1	Simplified Block Diagram of Wind Energy Conversion and Storage System	167
Figure B.1	Generator Open-Circuit Armature Voltage and Short-Circuit Armature Current as a Function of Field Excitation	172
Figure B.2	Generator Armature Inductance as a Function of Field Excitation	174
Figure B.3	Wind-Power Extraction Characteristic Designed for Physical Scale Model System	179
Figure C.1	Variation in Battery Bank Parameters, Away from Nominal Values, as a Function of Battery State-of-Charge	185
Figure D.1	DC Motor Circuit Model	187
Figure D.2	DC Motor Magnetization Curve	194
Figure D.3	No-Load Motor Torque-Speed Characteristics	195
Figure D.4	No-Load Motor Losses as a Function of the Square of Motor Field Flux Level	197
Figure E.1	No-Load Generator Torque-Speed Characteristic	201
Figure E.2	Generator Core Losses as a Function of the Square of Generator Field Flux Level	203
Figure E.3	Equivalent Generator Stray-Loss Resistance as a Function of Shaftspeed	206
Figure G	Remodeled Charging Circuit and Input Waveform	218

LIST OF TABLES

		Page
Table 1	Positions of SCR Gate Switches as a Function of the States of X, T and R	129
Table B.1	Generator Ratings and Specifications	170
Table B.2	Generator Base Quantities	171
Table C.1	Internal Battery Parameter Measurements	182
Table C.2	Per-Unit Battery Bank Parameters as a Function of Battery State-of-Charge	183
Table D.1	Motor Parameters	188
Table D.2	Motor Ratings	190
Table D.3	Motor Base Quantities	191
Table F.1	Description of Computer Program Variables and Their Relation to Variables Used in the Text	211

BACKGROUND AND INTRODUCTION

Between September 1975 and May 1976, research supported by the New England Regional Commission had been done at M.I.T.'s Electric Power Systems Engineering Laboratory to develop an efficient wind-energy conversion and battery storage system (both References 1 and 2 document the work). In summary, the research consisted of a proposed control system that achieves maximum wind-to-electrical power conversion in a lossless windmill power system. The operational criterion is to maintain the ratio of windspeed to shaftspeed constant, thereby allowing maximum power conversion to be achieved. This then requires a load control that can continuously match the load to the existing wind conditions.

In the mentioned documentation, the methods of load control introduced were generator field current control and the switching of battery load voltage. Both controls were stated necessary due to the inability of either control alone to vary load sufficiently to achieve efficient energy conversion.

A control algorithm was developed to maintain optimum extraction efficiency in the case of the lossless system introduced. Also, coupled system dynamics, using a simple inertia model for the windmill and a first order pole field current control for the generator, were studied via computer simulation, again in the no-loss case.

The purpose of this thesis is the continued study of the proposed windmill power system leading to the construction of a scale model system. The study involves only the electromechanical conversion of wind derived energy and the storage of that energy in lead-acid

batteries. The aerodynamic effects of the windmill, i.e., blade dynamics, structural resonances, etc., are not considered. Also of minimal consideration is the load application for which the batteries will be used, i.e., conversion to 60 Hz or a dc application.

However, of major consideration are power system power-loss mechanisms. These losses are present in windmill, generator and batteries. The effect of these losses on system behavior and control is studied and evaluated. Due to system losses, the control criterion is not necessarily to maximize the energy extracted from the wind but to maximize the energy stored in the batteries.

Involved in the above criterion is the consideration of system load variations as a function of battery state-of-charge. Maximum power conversion, mechanical to electrochemical, can theoretically be maintained for as long as the batteries can present the required load to the system. However, if the power system has been designed for a nominal battery state-of-charge then the deviation from that state-of-charge will influence overall system efficiency, power conversion capability and relative dynamic stability. These effects are investigated in this thesis.

Also introduced in the thesis are alternate methods of system load control other than the methods previously mentioned, i.e., generator field current control and battery section switching. The two methods considered are phase control of the rectified generator output and the series-to-parallel switching of generator windings in a multivoltage machine.

The body of the thesis is divided into five chapters. The first chapter deals with a detailed description and modeling of the elements

of the proposed windmill power system. The second chapter deals with the philosophy of windmill power system design and with coupled system behavior. The third chapter presents the results of a computer simulation designed to evaluate both the steady-state and dynamic behavior of the windmill power system. Empirical data for the simulation are obtained from the elements used in the system implementation.

Chapter IV presents the implementation of the control system for the physical scale model simulation of the windmill power system. Finally, Chapter V involves the testing and evaluation of the scale model system and the comparison of the results with the results of the computer simulation.

Several appendices are also attached. Appendix A, previously mentioned, presents background research to this thesis. Appendix B deals with the implementation of the power system design of Chapter II on the physical scale model system. Appendices C, D, and E present the methods used in obtaining the empirical data used in both the computer simulation and physical system implementation. Appendix F presents the computer program used for the dynamic system simulation. Finally, Appendix G deals with the calculation of the smoothing choke inductance used in the battery charging circuit.

CHAPTER I

SYSTEM DESCRIPTION AND MODELING

Maximum power transfer from wind to batteries requires coordination in the design and operation of the component subsystems, i.e., windmill, generator and battery load. Figure A.1 in Appendix A shows a simplified block diagram for the proposed system. Simplified models for the components subsystems are presented in Reference 2.

In this chapter a more detailed description and modeling of the power system components will be presented. An important consideration will be sources of power loss within the system.

To maintain generality, all quantities have been per-unitized with base values chosen to correspond to rated generator quantities and rated, i.e., designed, wind speed.

I.1 Windmill Characteristics

I.1.a Wind Power Extraction

Both Appendix A and Section I.1 of Reference 1 derive an equation that relates the power extracted from the wind to wind velocity, windmill shaftspeed and parameters of the wind and windmill (see Eq. A.2, Appendix A). For a given windmill, if air density is assumed constant then the power extracted from the wind may be described as

$$\text{Wind Power Extraction} \equiv P_{ext} = b\left[C_p\left(\frac{\omega_s}{av_w}\right)\right] v_w^3 \qquad (1)$$

where ω_s and v_w are the per-unit shaftspeed and wind velocity, respectively. The quantity, C_p, a function of v_w, ω_s and the constant "a" is defined here as the per-unit power ratio, i.e., the ratio between actual wind-power extraction and maximum extractable wind-power for a given wind velocity. A typical windmill C_p curve is plotted in Figure 1. Note when shaftspeed is maintained proportional to wind velocity in the manner $\omega_s = av_w$ then C_p remains at its maximum value during changes in windspeed, i.e., $C_p(1) = 1$. In this way, maximum power is continuously extracted from the wind.

The quantities "a" and "b", Eq. 1, are per-unit windmill parameters. They can be more easily understood with reference to Figure 2 which shows P_{ext} plotted versus shaftspeed for different values of wind velocity. The parameters "a" and "b" are such that at rated wind velocity, i.e., $v_w = 1$, the maximum extractable wind power occurs at the shaftspeed $\omega_s = a$ and has the value $P_{ext} = b$.

The windmill parameters "a" and "b" relate windmill characteristics to rated generator quantities. The reason for this form of windmill description will become evident in Chapter II.

The nonanalytical form of the C_p curve makes detailed system analysis difficult. However, since system operation is desired only at the peak of the C_p curve, where maximum wind power is extracted, then this region of the curve can be approximated by a parabola. As a first approximation C_p may be represented as

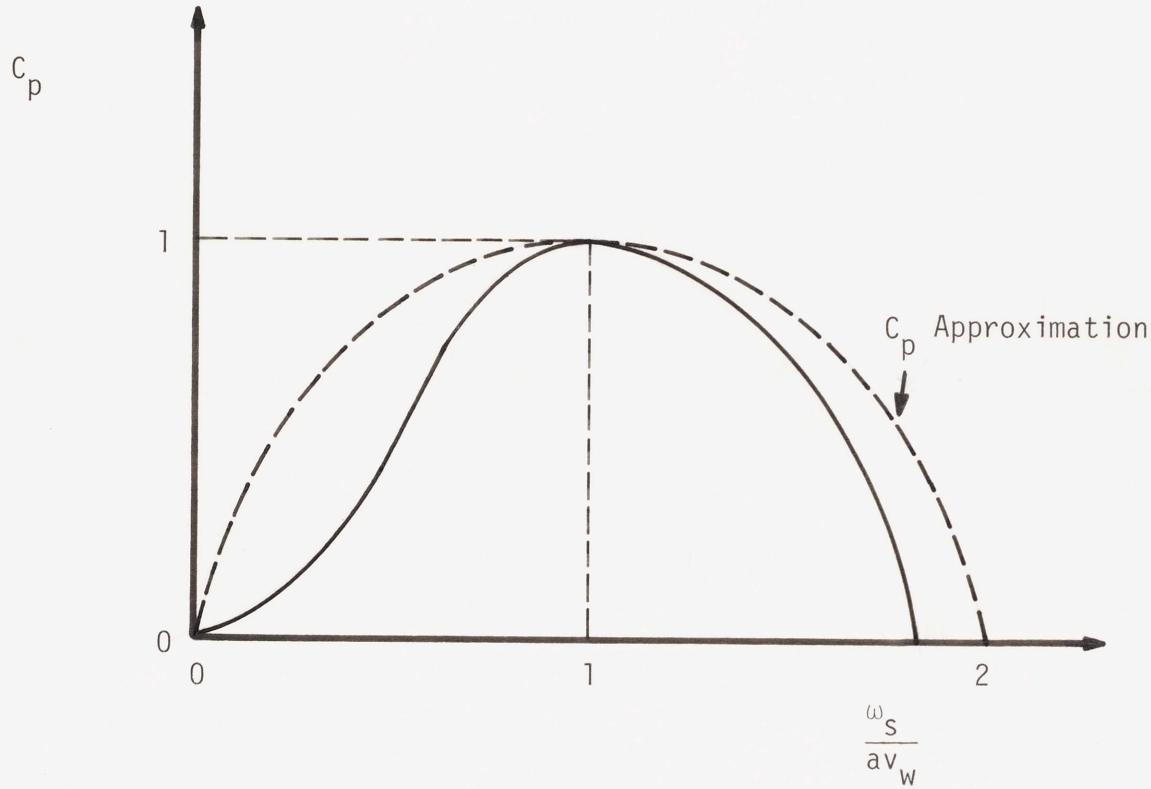

Figure 1 Typical Windmill C_p Curve and Analytic Approximation

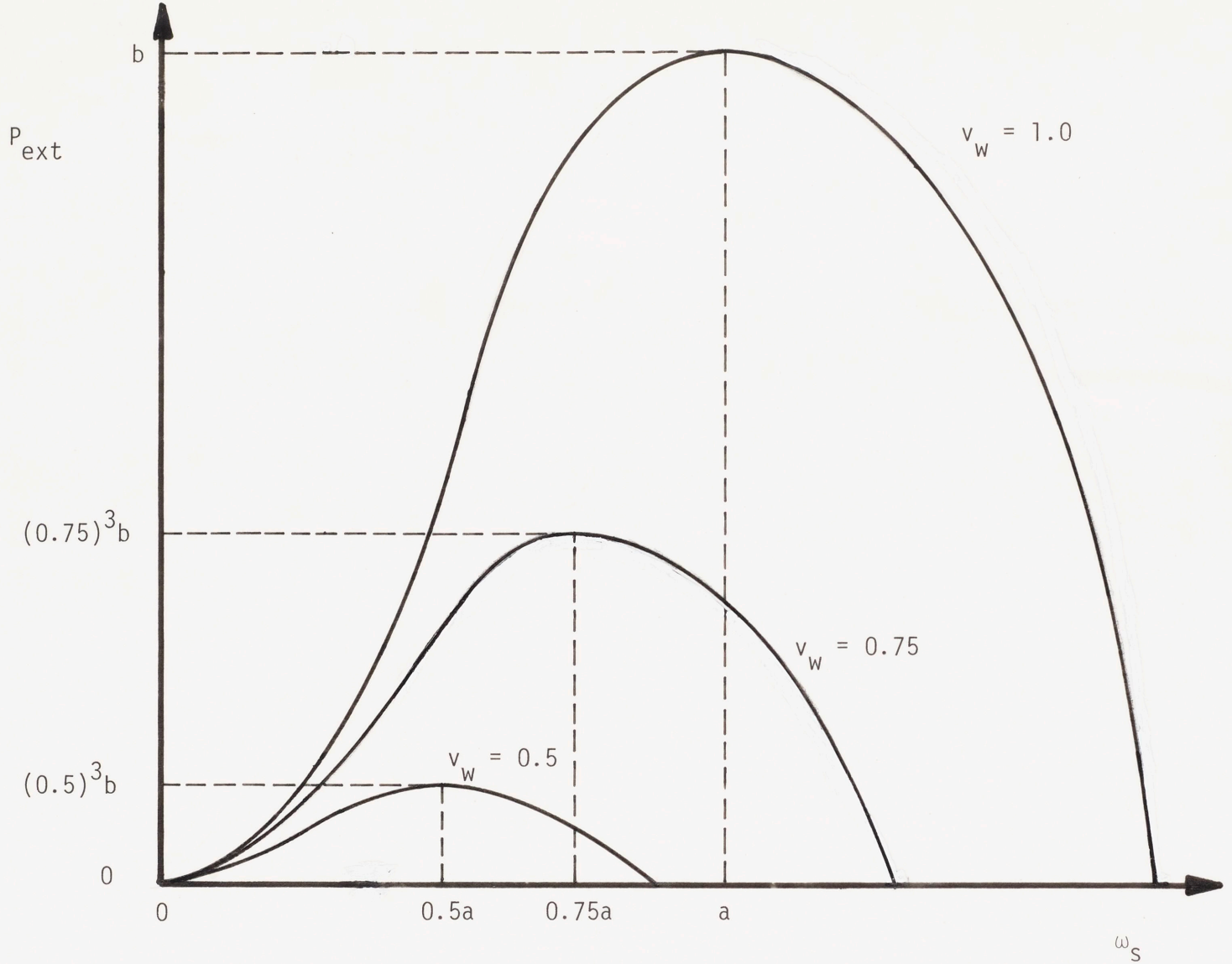

Figure 2 Wind Power Extraction as a Function of Shaftspeed and Wind Velocity

$$C_p \simeq \frac{1}{v_w^2}\left(\frac{2v_w\omega_s}{a} - \frac{\omega_s^2}{a^2}\right) \qquad (2)$$

This approximation to C_p is plotted in Figure 1 along with the typical curve. Note that the approximated curve has the desired property: $C_p(\omega_s = av_w) = 1$. Also notice that the approximate curve has less curvature than the actual windmill curve. However, a more accurate approximation for the given C_p curve may be of little value due to variations in these curves for different windmill designs. Thus the approximate curve will be considered sufficiently valid for further calculations. The effects of increased curvature of the C_p curve will be further discussed in Chapters II and III.

I.1.b Windmill Power Loss Characterization

The final topic of interest in terms of windmill characteristics is windmill mechanical power losses. These losses are largely due to bearing friction associated with the windmill shaft and gears, the gears being necessary to step-up the shaftspeed of the windmill to that acceptable to the generator. Analytically these losses may be modeled by two components; one that varies linearly with shaftspeed and the other that varies with the square of shaftspeed, i.e.,

$$\text{Windmill Mechanical Power Losses} \equiv P_{\ell wm} = C_{w1}\omega_s + C_{w2}\omega_s^2 \qquad (3)$$

where the loss coefficients, C_{w1} and C_{w2}, can be empirically determined for a given windmill.

Appendix D shows the calculation of C_{w1} and C_{w2} for the windmill used in the physical scale model simulation.

I.2 Generator and Load Characteristics

I.2.a Battery Characteristics

The battery sections to be employed in the system may be modeled as voltage sources in series with an internal resistance. The internal voltage of a single lead-acid cell is nominally about 2 volts and varies as a function of the state-of-charge of the cell. The internal resistance of a cell is dependent on several factors. These factors include the capacity of the cell, its state-of-charge, and the magnitude and direction of the current flowing through it. Detailed voltage and resistance measurements of the battery sections to be employed in the windmill power system can be found in Appendix C.

I.2.b Generator and Charging Circuit Characteristics

The preferred electromechanical converter for the proposed power system is a polyphase synchronous alternator with a full-wave rectified output. An ac machine is preferred to a dc machine due to its simplicity and greater efficiency. The rectification of the alternator output produces the dc necessary for battery storage.

A polyphase ac machine is preferred to a single-phase machine for several reasons. First, for the same line-to-line voltage rating, a polyphase machine produces a larger average-to-peak rectified voltage than a single-phase machine. The higher output voltage results in less sensitivity to power losses due to diode drops in the output circuit, i.e., the diodes associated with rectification. Additionally, for machines of the same voltage and power ratings, the rectified output of

the polyphase machine supplies a smaller current. The lower current results in lower power losses due to resistive elements in the generator output circuit, i.e., internal battery resistance and the resistance associated with a smoothing choke in the circuit.

A smoothing choke is used in series with the batteries to maintain a DC charging current. An additional advantage to polyphase rectification is a less stringent requirement on the value of this inductance necessary to maintain a certain ripple factor in the charging current. In general, a smaller series inductance has associated with it a smaller series resistance, resulting in lower power losses in the charging circuit.

In comparing full-wave to half-wave rectification of the generator output, the major advantage is in terms of machine flux levels. Full-wave rectification allows current to flow in both directions in each armature winding of the machine. The resulting lack of dc bias in the machine flux level produces greater generator utility.

I.2.c Battery Charging Circuit Analysis

In this section a detailed model for the generator and battery charging circuit is presented and analyzed. The analysis is generalized for a single-phase or polyphase alternator. However, in constructing the model, the simplest scheme, i.e., a single-phase alternator with full-wave rectified output, is considered. A single-phase machine is also the machine that is available for the scale model simulation of the windmill power system to be presented in Chapter 4.

Figure 3 shows a detailed circuit model for the proposed generator output circuit. E_f is the open-circuit terminal voltage of

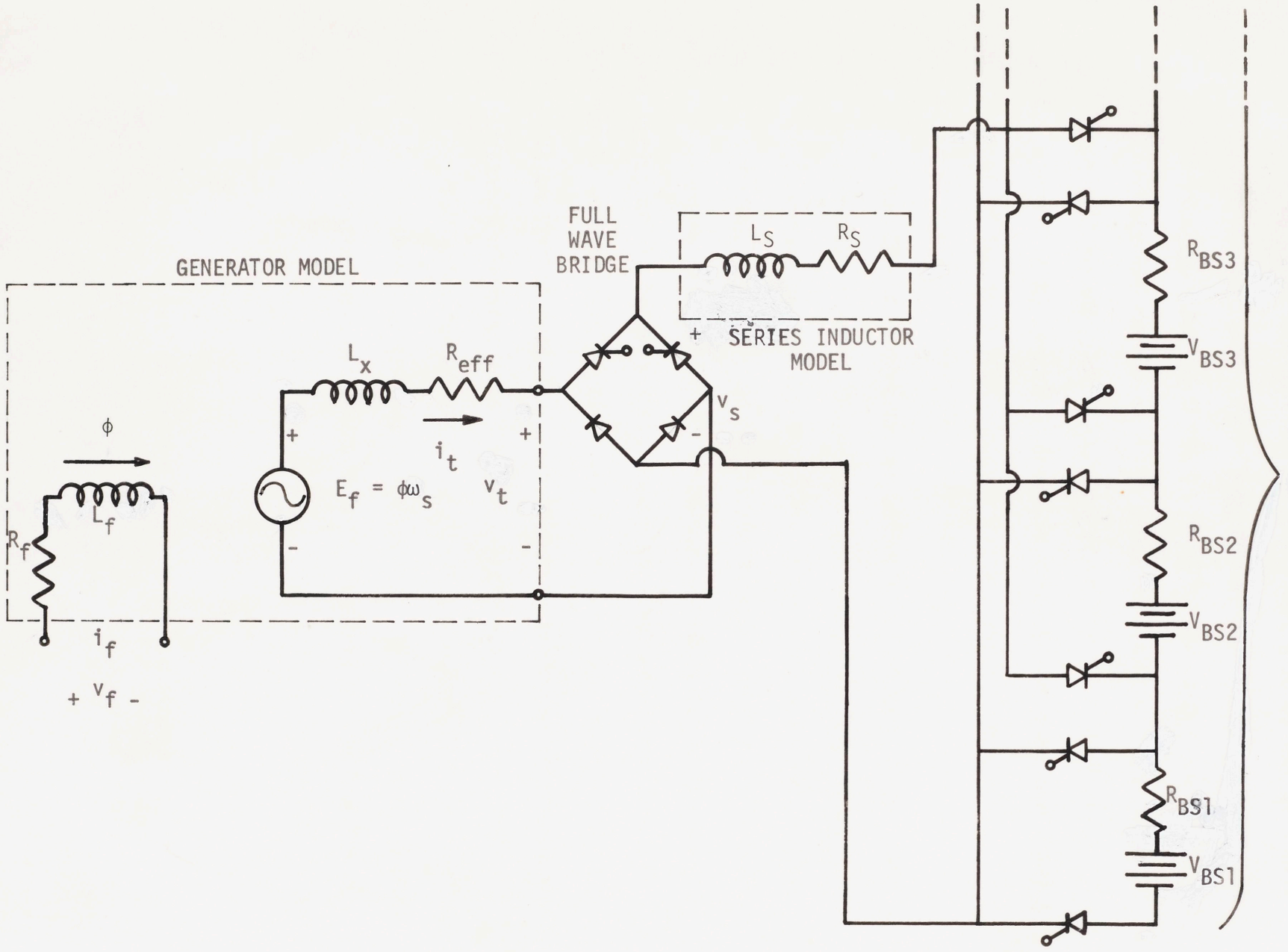

Figure 3 Single-Phase Battery Charging Circuit

the generator. L_x and R_{eff} are respectively the inductance and effective resistance "seen behind" the armature terminals of the generator.* L_f and R_f are respectively the inductance and resistance of the generator field winding. The quantities v_t and i_t are respectively the ac terminal voltage and current for the armature winding. Also v_f and i_f are the dc voltage and current for the generator field terminals. V_{BSn} and R_{BSn} (n = 1 to N) are the respective internal voltages and internal resistances of the individual battery section where N is the total number of sections.

The SCR's adjacent to the batteries, in Figure 3, are used as switches to series connect the battery sections depending on the required generator load. The two SCR's in the full-wave bridge also act as switches. They are used as a simple means to "turn off" the battery charging current to allow the battery SCR's to commutate. Commutation of the battery SCR's occurs when battery-load voltage is altered or when battery sections are electronically rotated such that each section charges equally. This battery rotation helps to maintain similar states-of-charge in all battery sections.

The series inductance, L_s, alters the output current waveform such that a higher average-to-peak current is attained. If L_s is made large enough, the current flowing into the batteries is virtually dc.

*The effective armature resistance consists of two components. One component is the actual armature resistance. The other component of R_{eff} models stray power losses within the machine. These stray losses will be further discussed in Section I.2.d.

The resistor, R_s, models the distributed resistance in the wire composing the inductor.

The voltage produced behind the terminals of the generator is related to the product of machine flux level and shaftspeed, i.e.,

$$E_f = \phi\omega_s \tag{4}$$

where ω_s is the per-unit shaftspeed and ϕ is the per-unit flux level within the machine produced by the generator field current. In this analysis, per-unit flux is defined as that flux necessary to produce 1 per-unit rms open-circuit voltage at 1 per-unit shaftspeed.

As previously stated, if the series inductance, L_s, is made large enough then the load current, on the battery side of the bridge circuit, is virtually dc. When continuous load current is flowing, the SCR's and diodes in the bridge conduct one pair at a time depending on the polarity of the sine-wave voltage, v_t. If the subtransient inductance of the armature winding is very much smaller than the synchronous inductance of the winding then the instantaneous reversal of the armature current, whenever v_t changes polarity, can be assumed. The result is square-wave armature current waveform.

The voltage, v_s, in Figure 3, is simply the full-wave rectification of the armature terminal voltage, less two diode drops due to the bridge rectifiers. The average value of v_s, i.e., $\langle v_s \rangle$, is

$$\langle v_s \rangle = \frac{2\sqrt{2}}{\pi}|v_t| - 2v_d \tag{5}$$

where $|v_t|$ is the rms terminal voltage and v_d is the forward voltage across a single conducting diode. The factor $2\sqrt{2}/\pi$ is just the ratio

of the average-to-rms value of a rectified sine-wave. Using Eq. 5 the circuit model shown in Figure 4 can be constructed. In this model the ideal transformer, the ideal ac-to-dc converter and the dc voltage source replace the bridge circuit in Figure 3. The ac-to-dc converter converts the rms value of the alternating voltage, v_r, to the average voltage, v_a such that $v_r = v_a$. Note that the series inductance, L_s in Figure 3, has been removed since its effect is implied by the converter. Also, in the model, the separate battery sections have been replaced by a single battery voltage, V_{BM}, and resistance, R_{BM}, where $V_{BM} = \sum_{n=1}^{M} V_{BSn}$ and $R_{BM} = \sum_{n=1}^{M} R_{BSn}$, M being the number of discrete sections charging. The dc voltage sources in the model represent the voltage drops due to the SCR's and diodes in the actual bridge rectifier and battery switches.

The turns ratio, 1:r, of the perfect transformer reflects the linear relationship between the rms generator terminal voltage, $|v_t|$, and the average voltage at the output of the rectifiers, $\langle v_s \rangle$. This relationship is given by Eq. 5 for a single-phase generator where r is $2\sqrt{2}/\pi$.

The conceptual advantage to the battery charging circuit of Figure 4 is that the model can also represent battery charging from a polyphase generator. If the previous analysis is reproduced for a polyphase machine the result is a similar single-phase model with the only major difference being in the transformer turns ratio, 1:r. For a two-phase machine, with phases separated by 90° (electrical), r, i.e., the ratio of average full-wave rectified armature voltage to rms

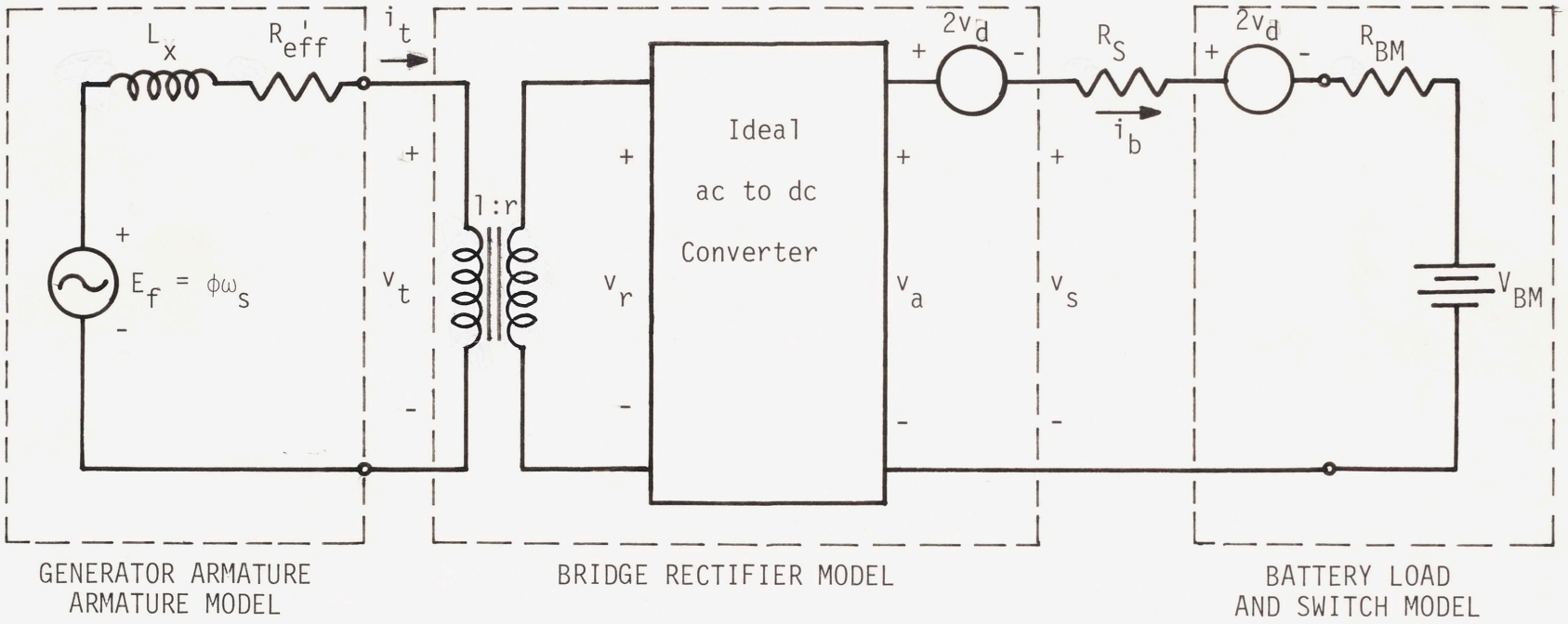

Figure 4 Generalized Battery Charging Circuit Model

line-to-line armature voltage, is $4/\pi$. For a three-phase balanced machine r is $3\sqrt{2}/\pi$.

When dealing in per-unit quantities, the transformer turns ratio in the charging circuit model is unity. In this case the factor r is used to reflect base quantities from one side of the transformer to the other.

The major disadvantage of the circuit model of Figure 4 is its inability to adequately represent the actual current in the generator armature. In the single-phase machine model of Figure 3, the armature current is a square wave with peak, or rms, value equal to the dc current flowing into the batteries. However, the generalized model shows the rms value of the armature current to be less than the battery current by the factor 1/r. This smaller armature current derived from the generalized model is, in actuality, the rms value of the fundamental component of the actual armature current waveform. This is more easily seen from the fact that power must be conserved through the ideal transformer and converter. On the dc side of the bridge model, power output is the product of the average values of voltage and current. On the ac side, however, power input is the product of the rms values of the fundamental components of the voltage and current waveforms. The higher harmonics of the actual armature current waveform contribute no average power flow through the bridge. Thus, since it is the fundamental component of the armature current that produces power then the current, i_t, in Figure 4, must represent this fundamental component.

There are other effects not adequately represented in the generalized circuit model presented. Firstly, the harmonic currents

in the armature winding produce harmonic fluxes within the machine. Due to these harmonic flux distributions, the inductance, L_x, "seen behind" the terminals of the generator may be different from the synchronous inductance of the machine. However, the internal voltage of the machine, E_f, is known for open-circuit conditions, i.e., Eq. 4 where ϕ is a known function of generator field current. Thus, by knowing E_f, L_x can be measured for the appropriate load conditions.*

The harmonic currents in the generator armature also add to power dissipation in the effective resistance of the armature winding. For the model to adequately represent these armature resistance losses the effective armature resistance must be increased by a correction factor $(1/r)^2$, i.e., the square of the ratio of actual rms armature current to the rms armature current modeled in Figure 4. Thus R_{eff} must be replaced by $R'_{eff} = R_{eff}/r^2$ for armature resistance power losses to be correctly modeled.**

*With the machine under battery load, L_x can be calculated from the armature voltage relationship: $|E_f|^2 = |v_t|^2 + (\omega_e L_x)^2 |i_t|^2$ where $|v_t|$ and $|i_t|$ are the rms voltage and current depicted in Figure 4, i.e., the fundamental components of the armature terminal waveforms, and ω_e, as previously defined, is the electrical frequency of v_t or i_t. Since v_t, i_t and ω_e can be measured and E_f is known, from Eq. 4, then L_x can be calculated.

**Note that R_{eff} is the effective resistance of one line-to-neutral phase in a polyphase machine.

The battery charging circuit model is now complete. The power output of the machine can now be calculated as a function of the circuit parameters. A per-unitized complex phasor diagram can be constructed for the generalized circuit model of Figure 4. This diagram is shown in Figure 5.

The phasor diagram shows generator terminal voltage and current in phase, which agrees with the fact that only real power is supplied by the generator. From the phasor diagram, the current out of the generator can be calculated. From Figure 5,

$$|E_f|^2 = |V_{BM} + 4v_d + (R_{BM} + R_S)i_b + R'_{eff}\, i_t|^2 + |\omega_e L_x i_t|^2 \quad (6)$$

Since, in per unit, $|i_b| = |i_t|$ and $\omega_s = \omega_e$ then Eq. 6 can be solved for $|i_t|$.

$$|i_t| = \frac{-V_L R_x + \sqrt{E_f{}^2(R_x{}^2 + X^2) - V_L{}^2 X^2}}{R_x{}^2 + X^2}; \quad |i_t| \geq 0 \quad (7)$$

where $V_L = V_{BM} + 4v_d$

$R_x = R_{BM} + R_S + R'_{eff}$

$X = \omega_s L_x$

$E_f = \phi\omega_s$

The power out of the generator terminals is:

$$\text{Generator Power Output} \equiv P_t = |v_t||i_t| \quad (8)$$

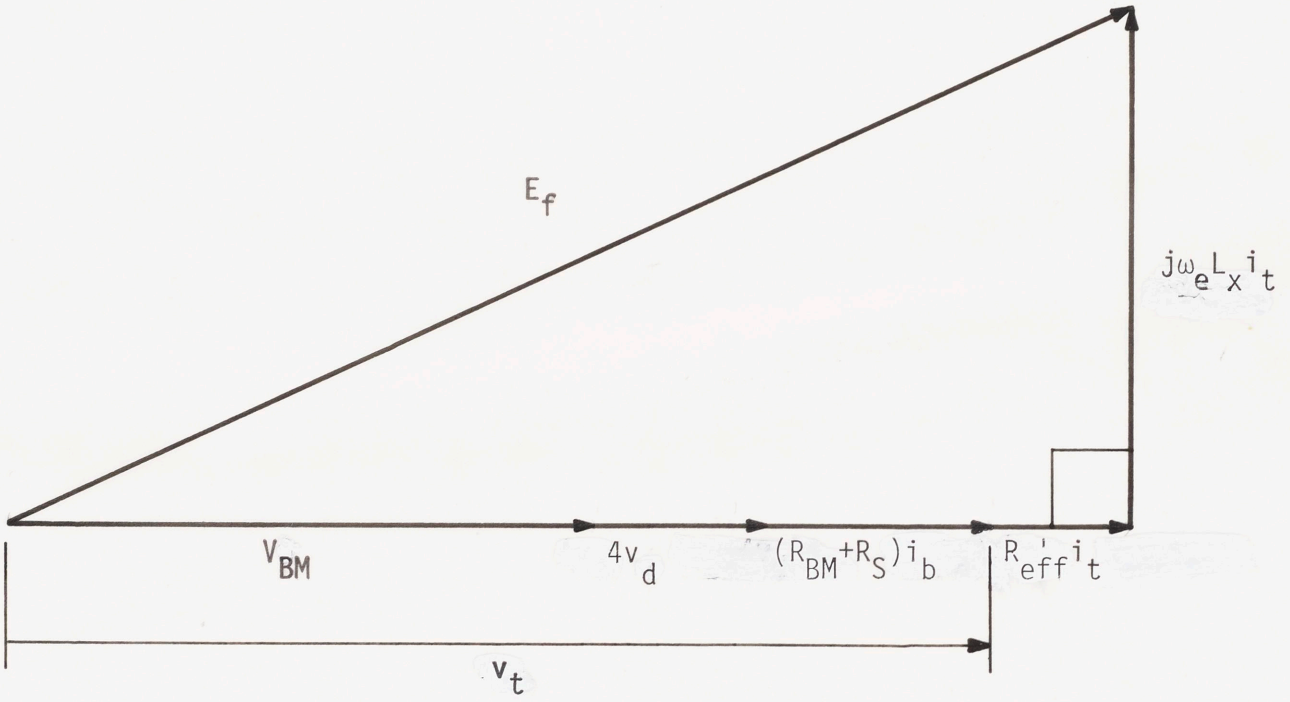

Figure 5 Complex Phasor Diagram of Generalized Circuit Model

where $|v_t|$ can also be calculated from the phasor diagram of Figure 5, i.e.,

$$|v_t| = V_L + (R_{BM} + R_S)|i_t| \tag{9}$$

Equations 7 and 9 can be substituted into Eq. 8 resulting in the generator power output as a function of generator shaftspeed, generator field excitation, battery characteristics and parameters of the charging circuit. The resulting equation is the output power-speed characteristic of the generator and can be plotted as a function of the number of battery sections charging. Figure 6 shows this plot for one, two and three battery sections charging, i.e., P_{t1}, P_{t2} and P_{t3}, respectively. The horizontal-axis intercepts are calculated from setting $|i_t|$ to zero, in Eq. 7, and solving for the zero-power shaft-speed.

The generator armature current and voltage limit lines, Figure 6, reflect that both rated machine armature current and rated machine power cannot be exceeded.

The maximum generator power output for a given battery load, P_{XM}, can be calculated from Eqs. 8 and 9 with $|i_t|$ set to 1, i.e.,

$$\begin{aligned} \text{Generator Output Limit} \equiv P_{XM} &= V_L + R_{BM} + R_S \\ &= V_{BM} + R_{BM} + 4v_d + R_S \\ &= M(V_{BS} + R_{BS}) + 4v_d + R_S \end{aligned} \tag{10}$$

where M is the number of charging battery section and V_{BS} and R_{BS} are the internal voltage and resistance of a single section, assuming all sections are at an equal state-of-charge. Maximum generator power

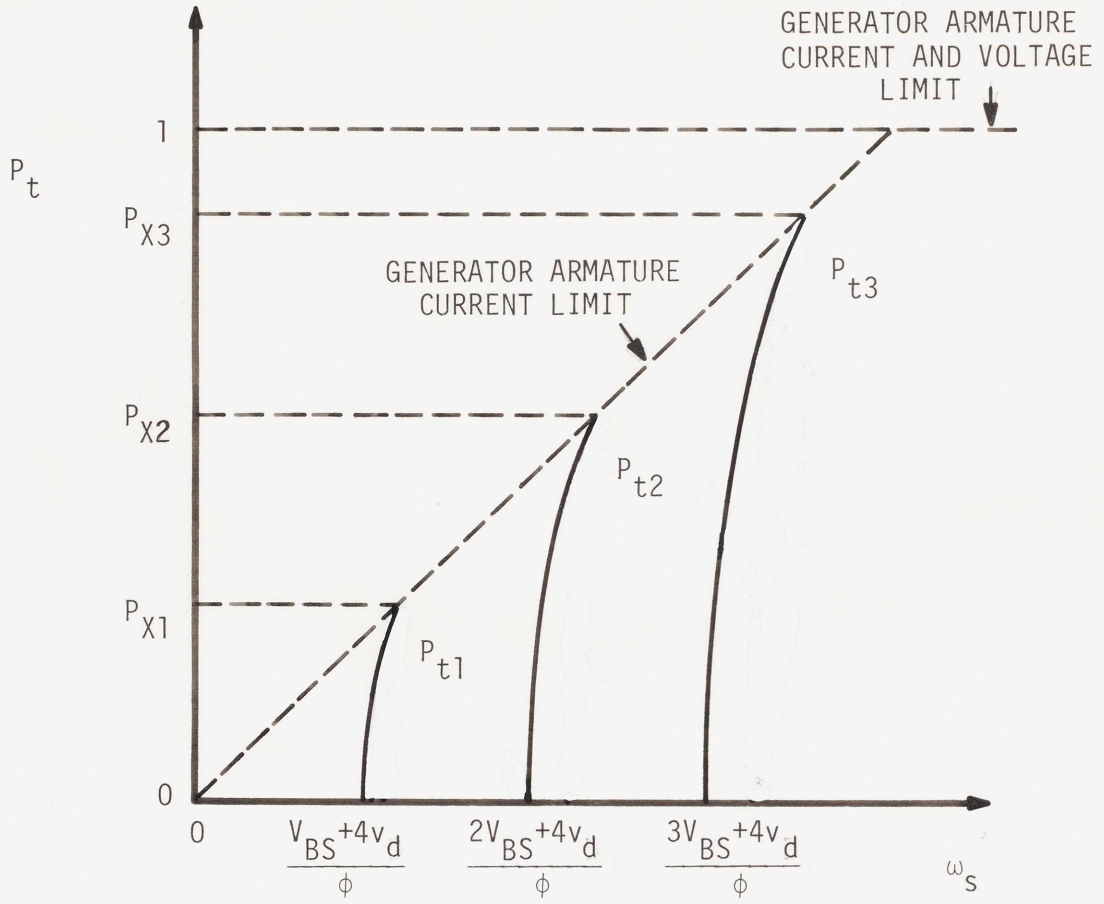

Figure 6 Generator Power-Speed Characteristics as a Function of the Number of Charging Battery Sections.

outputs for the three respective battery loads in Figure 6 are also shown in the same figure.

Two important observations can be made about the power characteristics of Figure 6. Firstly, as generator flux level, ϕ, is increased by increasing generator field current, both the power characteristics and generator armature current limit line move to the left in the figure. However, there is a limit to how far these characteristics can move. Flux saturation in the machine iron does not allow the air-gap flux to exceed a maximum level, ϕ_m. Thus generator operation is restricted to the right of the characteristic curves $P_{tM}(\phi = \phi_m)$.

A second observation on Figure 6 is in the variation in the power characteristics as a function of battery state-of-charge. As internal battery voltage increases, i.e., via increased battery state-of-charge, the power characteristics shift to the right along the existing generator limit line. Thus possible regions of generator operation vary also as a function of battery state-of-charge.

I.2.d Generator Power Loss Characterization

There are several sources of power loss in an ac machine. Mechanical losses consist of brush and bearing friction and windage. In a manner similar to Section I.1.b, these losses can be modeled by components varying linearly and with the square of shaftspeed. Thus

$$\text{Generator Mechanical Losses} \equiv P_{\ell gm} = C_{g1}\omega_s + C_{g2}\omega_s^2 \qquad (11)$$

where C_{g1} and C_{g2} are the mechanical-power-loss coefficients for the generator.

A second source of generator power loss is magnetic-core loss. This consists of hysteresis and eddy-current power losses arising from changing flux distributions in the iron of the machine.

Eddy-current loss is dependent on the product of the squares of both generator flux density and shaftspeed, i.e.,

$$\text{Eddy-Current Losses} \equiv P_{\ell e} = C_e \phi^2 \omega_s^2 \tag{12}$$

where C_e is the loss coefficient for these eddy-currents. C_e is a function of the lamination thickness, volume, and the resistivity of the iron.

Hysteresis loss can be analytically expressed as

$$\text{Hysteresis Power Losses} \equiv P_{\ell h} = C_h \phi^k \omega_s^2 \tag{13}$$

where C_h is the loss coefficient for these losses. C_h is dependent also on the characteristics and volume of the machine iron. The constant, k, ranges from 1.5 to 2.5 depending, again, on the characteristics of the iron. A value of 2 for k is often used for estimation purposes.

Another source of machine power loss, stray loss, arises from both nonuniform current distributions in the copper windings and core losses produced by the distortion of the magnetic flux wave when the machine is under load. These losses can be related to the square of the armature current and thus may be expressed as an additional resistive component in the armature winding.[3] These stray losses also vary as a function of generator shaftspeed. The appropriate stray-loss resistance can be combined with the copper resistance of the armature winding to create an effective armature resistance, R_{eff},

i.e., the resistance depicted in the circuit model of Figure 3. Thus

$$R_{eff} = R_a + R_{st}(\omega_s)$$

and (14)

$$R'_{eff} = R_{eff}/r^2 = (R_a + R_{st}(\omega_s))/r^2$$

where R'_{eff} is the resistance modeled in Figure 4. R_a is the copper resistance of the armature winding and $R_{st}(\omega_s)$ is the equivalent stray-loss resistance as a function of generator shaftspeed.

Detailed power-loss measurements and methods of calculation are described in Appendix E for the synchronous alternator used in the scale model power system. Parameter measurements for the battery charging circuit of Figure 4 are also found in Appendix E.

I.2.e Other Methods of Generator Load Control

Two alternative methods of generator load variation will be introduced in this section. The first is the series-to-parallel switching of generator windings in a machine with a multivoltage armature. The second is phase control of the bridge rectifier.

(i) Generator Winding Switching

The series-to-parallel switching of generator armature windings in a multivoltage machine can be an alternative to battery voltage switching for the purpose of accomplishing generator load control. In this case only one battery section is required in the power system. A charging circuit model similar to Figure 4 can be created for the

multivoltage generator. Figure 7 shows the model. In this case, E_f, L_x, and R'_{eff} are respectively the internal voltage, inductance and resistance associated with a single set of machine windings, i.e., one winding from each phase. The variable transformer, with turns ratio $1:M'$, models the discrete variation in both generator terminal voltage and current ratings as a function of the number of series connected windings. M' may vary from 1 to N', where N' is the total number of duplicate windings. However, if the machine is to maintain the same power rating for all possible series-parallel winding connections, then M' must be a factor of N', i.e., M' sets of winding connected in series, with each set consisting of N'/M' windings connected in parallel.

The power output of the multivoltage generator, P_t', can be calculated in a manner similar to that employed for the circuit in Figure 4. Keeping M' as a parameter in the system, the generator power output, P_t', is

$$P_t' = |v_t||i_t| \tag{15}$$

$$|v_t| = \frac{V_L'}{M'} + \frac{(R_B + R_S)}{M'^2}|i_t| \tag{16}$$

and

$$|i_t| = \frac{-V_L' R_x' + \sqrt{M'^2 E_f^2 (R_x'^2 + X'^2) - V_L'^2 X'^2}}{R_x'^2 + X'^2} \tag{17}$$

and where

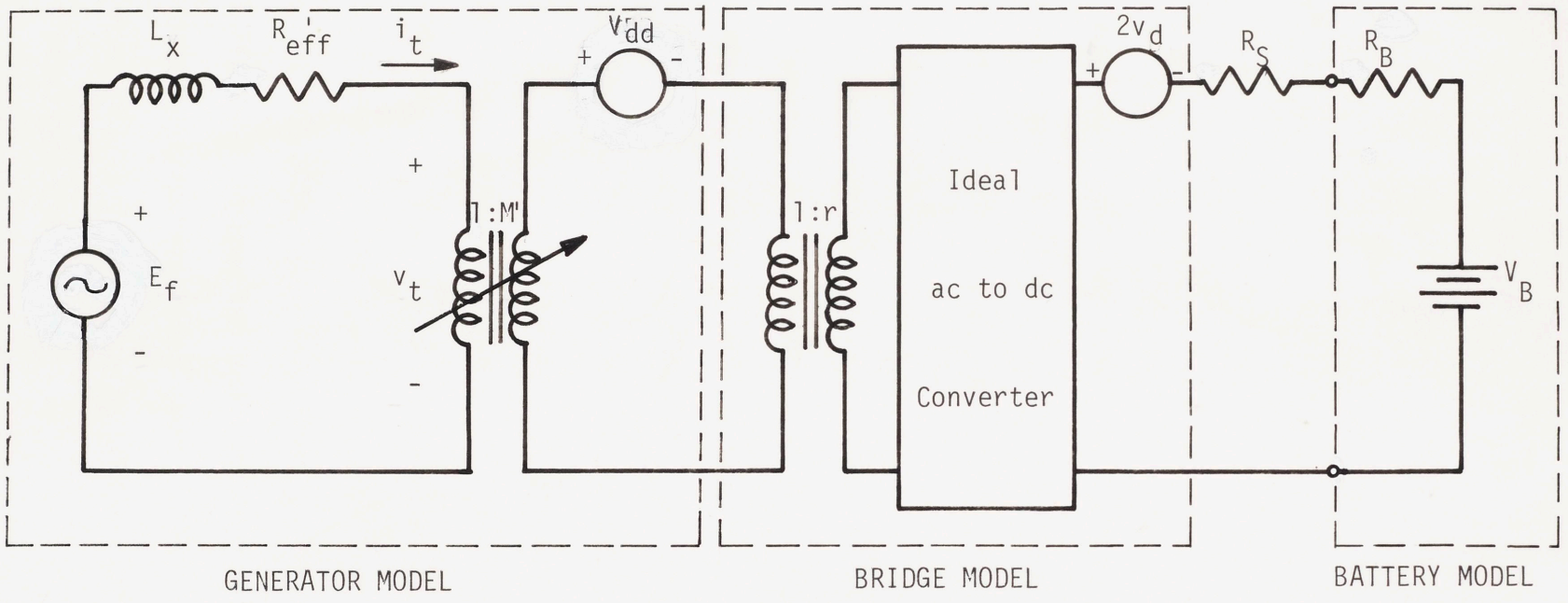

Figure 7 Charging Circuit Model for Machine with Multivoltage Armature

$$V_L' = V_B + 2v_d + v_{dd}$$

$$R_x' = R_B + R_S + M'^2 R_{eff}'$$

$$X' = \omega_s M'^2 L_x$$

$$E_f = \phi\omega_s$$

All the unprimed quantities have been defined previously, Section II.2.c, or are shown in Figure 7. The quantity v_{dd}, shown as a voltage source in Figure 7, is the sum of all voltage drops associated with the armature winding switches.

As was done in Figure 6, the power-speed characteristic, P_t', can be plotted as a function of generator field flux excitation and number of series-connected armature windings, i.e., M'. Figure 8 shows this plot for N', the total number of duplicate windings, equal to six.

The horizonal-axis intercepts are calculated from setting $|i_t|$ to zero in Eq. 17. The power limits, P_{XM}', are plotted on the vertical axis. These limits are calculated for the different values of M' by substituting Eq. 16 into Eq. 15 and setting $|i_t| = 1$, the rated current in each armature winding, in the result.

Note that as a function of field flux, ϕ, the power-speed characteristics of Figure 8 produce the same behavior as the characteristics for the battery-switching model shown in Figure 6. The major difference, however, is in the spacing of the characteristics in the generator's operating region.

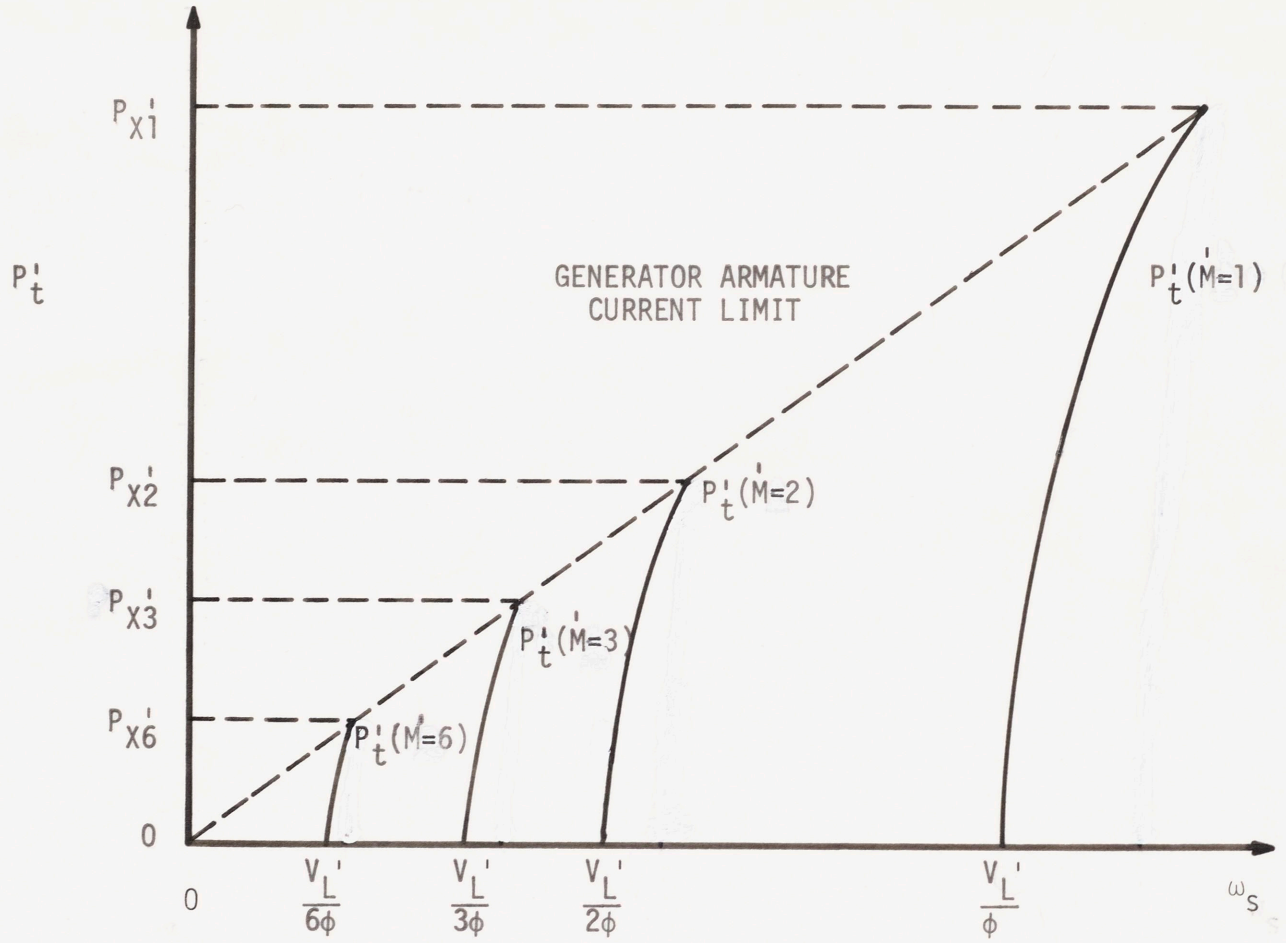

Figure 8 Power-Speed Characteristic for Multivoltage Generator

(ii) Rectifier Phase Control

Phase control of the bridge rectifier is an alternative to generator field current control in achieving a continuous means of varying generator load. The phase control function can be implemented in the single-phase charging circuit of Figure 3. Two effects result from this implementation. First, the average voltage on the battery side of the bridge is now $\langle v_s \rangle = \frac{2\sqrt{2}}{\pi}|v_t|\cos\alpha - 2v_d$ where α is the phase firing angle of the bridge. Second, the fundamental components of the voltage and current waveforms at the terminals of the generator are now α degrees out of phase, with the current lagging the voltage. This effect is due to the delay in generator armature current reversal produced by the delayed firing of the bridge rectifiers. A model similar to the one shown in Figure 4 can be constructed for the phase-controlled rectifier bridge. The result includes a multiplicative factor in the ideal ac-to-dc converter such that $v_a = v_r \cos\alpha$, and a phase shift element at the terminals of the generator which forces the current to lag the voltage by α degrees. As in Figure 5, a complex phasor diagram can be drawn for the ac side of the charging circuit model. This diagram is shown in Figure 9 with variables defined as in Figure 4.

Using the phasor diagram and the fact that now the generator terminal voltage is

$$|v_t| = v_r \cos\alpha = [V_{BM} + 4v_d + (R_{BM} + R_S)|i_t|]\cos\alpha \qquad (18)$$

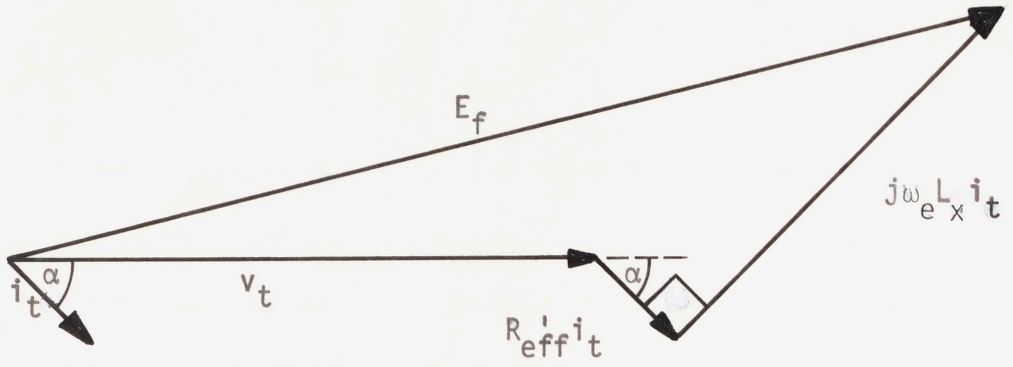

Figure 9 Complex-Phasor Diagram of a Phase-Control Bridge Circuit

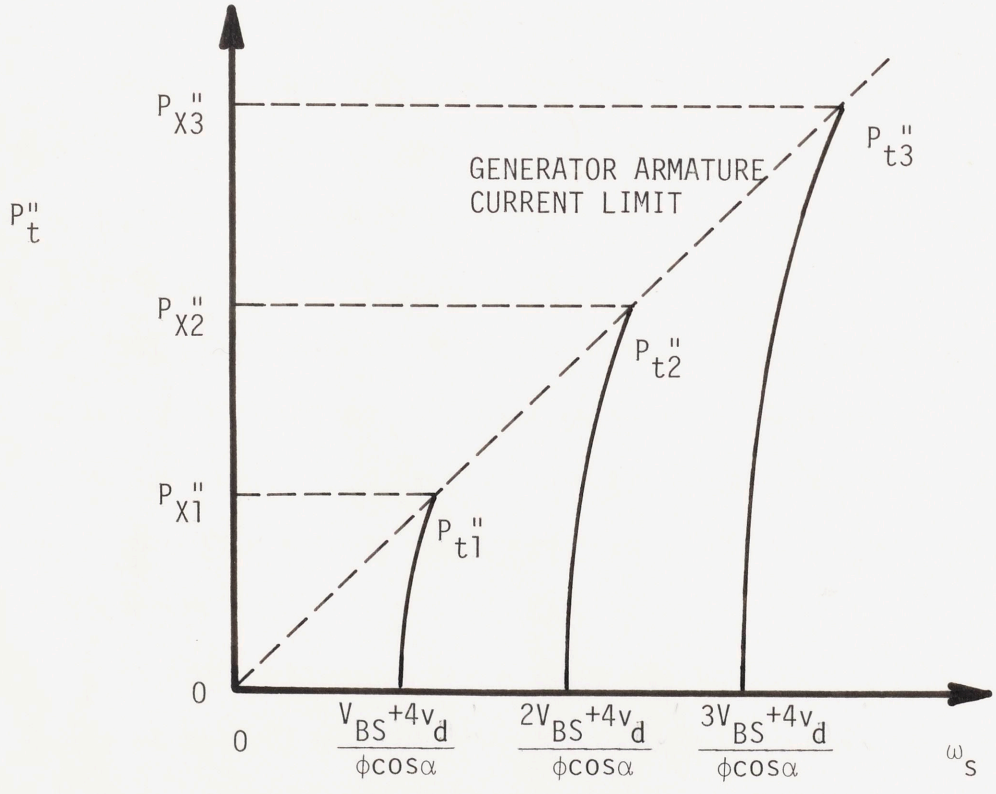

Figure 10 Power-Speed Characteristics for Phase-Controlled Rectifier

the armature current, $|i_t|$, can be calculated. The real power out of the generator terminals, P_t'', is now

$$P_t'' = |v_t||i_t|\cos \alpha \tag{19}$$

where the factor cos α is due to the phase shift between the armature voltage and current waveforms.

The power-speed characteristics defined by P_t'' can be plotted as a function of number of charging battery sections, the generator field flux level and the phase angle, α. The plots are shown in Figure 10 for one, two and three charging battery sections. The horizontal-axis intercepts are calculated by setting $|i_t|$ to zero in Eq. 18 and noting, from the phasor diagram, that $|v_t| = |E_f| = |\omega_s \phi|$ when $|i_t| = 0$. The vertical-axis power limits, P_{XM}'', of Figure 10 are calculated by substituting Eq. 18 into Eq. 19 and setting $|i_t| = 1$ in the result.

Note the similarity in characteristics of Figures 6 and 10. However, in Figure 10, the position of the characteristics now vary as a function of the product of generator flux, ϕ, and firing angle, cos α. Thus there is a redundancy in generator load control if both phase control and field flux control are implemented. If phase control alone is used to vary generator load then the generator flux level can be set to its saturation level, ϕ_m. In this way, phase control can achieve the identical generator output characteristics as field current variation did in Figure 6.

In the scale model power system to be designed, both generator field current control and battery voltage switching have been chosen to control generator load. The advantage of generator field control to

phase control of the bridge rectifiers is that, with the former control, generator operation is maintained at unity power factor. Battery voltage switching is chosen over the switching of generator windings in a multivoltage machine due to the former's greater simplicity in circuit implementation. However, with the latter control, only one battery section is required in the battery bank thus removing any anomalies in system performance due to unequal states-of-charge among the individual battery sections.

CHAPTER II

PHILOSOPHY OF WINDMILL POWER SYSTEM CONSTRUCTION AND COUPLED SYSTEM CONTROL AND BEHAVIOR

In Chapter I the elements composing the proposed windmill power system were presented and modeled in detail. The purpose of this chapter is to coordinate windmill power system design such that an efficient and compatible conversion system is achieved.

To maintain generality, all quantities have been per-unitized. The advantage of a per-unit system is that very little importance is given to the absolute values of the base quantities.

II.1 Windmill Power System Construction

In the design of a practical wind energy conversion system a detailed study of load application and wind profile must be carried out before a compatible system can be constructed. However, the results of a wind and load analysis have little importance to the present study. This is because, in keeping with the philosophy of a per-unit system, a value of 1 per unit can be arbitrarily assigned to the desired power output of the windmill-coupled generator when the wind velocity is at its designed, i.e., 1 per-unit, value.

At the designed wind velocity, the operation of the generator at its rated capability is also desirable. In this way, full generator utility is achieved, at least at rated wind velocity. Thus one per-unit generator power output corresponds to rated machine armature-terminal variables, rated, or maximum, machine flux level and rated machine shaftspeed. In keeping with the per-unit convention, all

these rated quantities, except machine flux, are also assigned the value of 1 per unit. For the generator field excitation, however, one per-unit machine flux was previously defined to be that flux necessary to produce 1 per-unit open-circuit armature terminal voltage at 1 per-unit shaftspeed. Thus, to be consistent with this definition, rated machine flux must be greater than one per unit by the amount that overcomes the reactive voltage drops within the machine when the machine is under rated load.

Now that a numerical assignment has been made to generator output at rated windspeed, i.e., 1 per unit, design of both the battery load and windmill can be effected such that a compatible system is attained at this rated windspeed.

For the generator to deliver rated power to the battery load at rated wind velocity, the characteristics of the battery bank, i.e., internal voltage and resistance, are chosen such that the batteries accept the required power. However, battery characteristics vary as a function of battery state-of-charge. Thus nominal values for these battery parameters must be chosen, preferably at some intermediate state-of-charge, where desired generator loading is achieved. Variation of these battery parameters away from their nominal values alters generator loading and may be detrimental to overall system efficiency and power conversion capability. The effect of battery state-of-charge on power system behavior will be further studied in Chapter III.

Nominal values for the battery parameters can be chosen with the aid of Figures 4 or 5. From the figures

$$|v_t| = V_{BM} + 4v_d + (R_{BM} + R_S)|i_t| \tag{20}$$

(The turns ratio, r, in Figure 4, is unimportant since the quantities in Eq. 20 are per-unitized.)

At 1 per-unit wind velocity, with all battery sections charging and each at a nominal state-of-charge, rated armature terminal voltage and current is desired. Thus replacing this constraint, i.e., $|v_t| = |i_t| = 1$, into Eq. 20 and noting that M = N, the total number of battery sections, results in the relationship

$$1 = V_{BN(NOM)} + 4v_d + R_{BN(NOM)} + R_S$$

or

$$V_{BN(NOM)} + R_{BN(NOM)} = 1 - 4v_d - R_S \tag{21}$$

where $V_{BN(NOM)}$ and $R_{BN(NOM)}$ are respectively the nominal internal voltage and resistance of the complete battery bank.

The relationship expressed by Eq. 21 is a design constraint for the battery bank. The nominal battery bank parameters, internal voltage and resistance, must be chosen according to Eq. 21 if the battery bank is to be capable of loading the generator properly at 1 per-unit wind velocity.

At an intermediate state-of-charge, $V_{BN(NOM)}$ is only proportional to the total number of cells in the battery bank. For the same state-of-charge, $R_{BN(NOM)}$ is both proportional to the number of cells and a function of the capacity and physical construction of the cells.

In general a battery with small internal resistance is desirable to maintain low power losses. However, being related to cell capacity, and thus load application, $R_{BN(NOM)}$ cannot always be made arbitrarily small.

As the result of the above analysis, the nominal values of internal voltage and resistance of a single battery section, i.e., $V_{BS(NOM)}$ and $R_{BS(NOM)}$, are

$$V_{BS(NOM)} = \frac{V_{BN(NOM)}}{N} \; ; \; R_{BS(NOM)} = \frac{R_{BN(NOM)}}{N} \tag{22}$$

where N is, again, the total number of battery sections in the battery bank.

Now that a compatible battery load is designed to accept maximum generator power output, a compatible windmill must be designed to deliver the required power to the generator during rated generator operation at rated wind speed.

If the generator is to supply rated power at both rated wind velocity and rated shaftspeed then the power extracted from the wind must supply, in addition to this rated power, all the power losses associated with the coupled windmill and generator. This required wind power extraction can be calculated from summing this desired generator power and all the power loss components, given by Eqs. 3, 11, 12, 13 and 14 with the generator parameters at their ratings. Thus for these rated conditions, i.e., $v_w = \omega_s = i_t = v_t = 1$ and $\phi = \phi_m$

Required Wind-Power Extraction $\equiv P_{RW}$ = Desired Generator Output + Armature Winding Losses + Generator Core Losses + Generator and Windmill Mechanical Losses

$$P_{RW} = 1 + R_{eff}' + (C_e + C_h)\phi_m^2 + C_{g1} + C_{g2} + C_{w1} + C_{w2} \quad (23)$$

The value of the rated generator flux level, ϕ_m, may be calculated from Figure 4 or from the complex phasor diagram of Figure 5. From the Figure,

$$|E_f|^2 = |\phi\omega_s|^2 = (|v_t| + R_{eff}'|i_t|)^2 + (\omega_s L_x|i_t|)^2 \quad (24)$$

where Eq. 4 has also been used.

For rated generator and wind conditions, i.e., $v_w = \omega_s = v_t = i_t = 1$ and $\phi = \phi_m$, Eq. 24 becomes

$$\phi_m^2 = (1 + R_{eff}')^2 + L_x^2 \quad (25)$$

where R_{eff}' as defined in Eq. 14, is determined for $\omega_s = 1$, i.e., rated shaftspeed.

Thus the required wind power extraction, at rated wind speed, as a function of the system loss coefficients and generator parameters is

$$P_{RW} = 1 + (C_e + C_h)[(1 + R_{eff}')^2 + L_x^2] + R_{eff}' + C_{g1} + C_{g2} + C_{w1} + C_{w2} \quad (26)$$

where Eq. 25 has been substituted into Eq. 23.

Eq. 26 provides a constraint on the choice of windmill for the power system. In terms of windmill parameters "a" and "b", defined in Section I.1.a, the power P_{RW} must be extracted from the wind at rated wind speed to maintain rated generator operation. Thus, using Eqs. 1 and 2, the following relationship for "a" and "b" results

$$P_{ext}\ (v_w = \omega_s = 1) = b\left(\frac{2}{a} - \frac{1}{a^2}\right) = P_{RW} \tag{27}$$

Solving Eq. 27 for "a" results in

$$a = \frac{b \pm \sqrt{b(b-P_{RW})}}{P_{RW}} \tag{28}$$

Since the parameter "b" is a measure of windmill size, i.e., "b" is the maximum extracted wind power at rated wind velocity, then the smallest value of "b", leading to a solution of Eq. 28, is desired. Choosing $b = P_{RW}$ leads to the solution $a = 1$.*

Thus the smallest windmill that, at rated wind velocity, saturates the power capability of the coupled generator for a chosen nominal battery load is a windmill with the power-speed characteristic

$$P_{ext} = P_{RW} v_w (2\omega_s v_w - \omega_s^2) \tag{29}$$

*Note that since the windmill power loss coefficients, C_{w1} and C_{w2}, are components of P_{RW} then the choice of "b" must be done in coordination with expected values of these windmill parameters.

At rated wind velocity and shaftspeed, i.e., $\omega_s = v_w = 1$, the windmill defined by Eq. 29 extracts the power P_{RW} from the wind. This power is also the maximum possible power that the windmill can extract at rated wind velocity, i.e., the windmill is operating at the peak of its C_p curve.

However, assuring the saturation of the generator's power output at rated wind velocity does not necessarily imply that the overall power system is at its most efficient point of operation.* Since system losses increase with shaftspeed, as described in Section I.1.b and I.2.d, one may conceive that system efficiency can be improved by operating the generator at a lower shaftspeed. At this lower shaftspeed, wind power extraction is decreased since operation is no longer at the peak of the C_p curve. Yet decreased losses may more than offset this lesser extraction resulting in an increased output. Figure 11 depicts the situation for the power system designed in this chapter. for rated wind velocity condition.

The curve, P_{ext}, in Figure 11, is the power-speed characteristic of the windmill, given by Eq. 29. The curve, P_g, is the generator terminal power vs. shaftspeed characteristic. P_g is formed by subtracting all the windmill and generator power losses from P_{ext} for every value of operating shaftspeed. For convenience a power-speed characteristic relating the power, at a point in the power system, to operating shaftspeed, wind velocity and system parameters will be

*Power system efficiency is defined as the ratio of power stored in the batteries to wind power extraction.

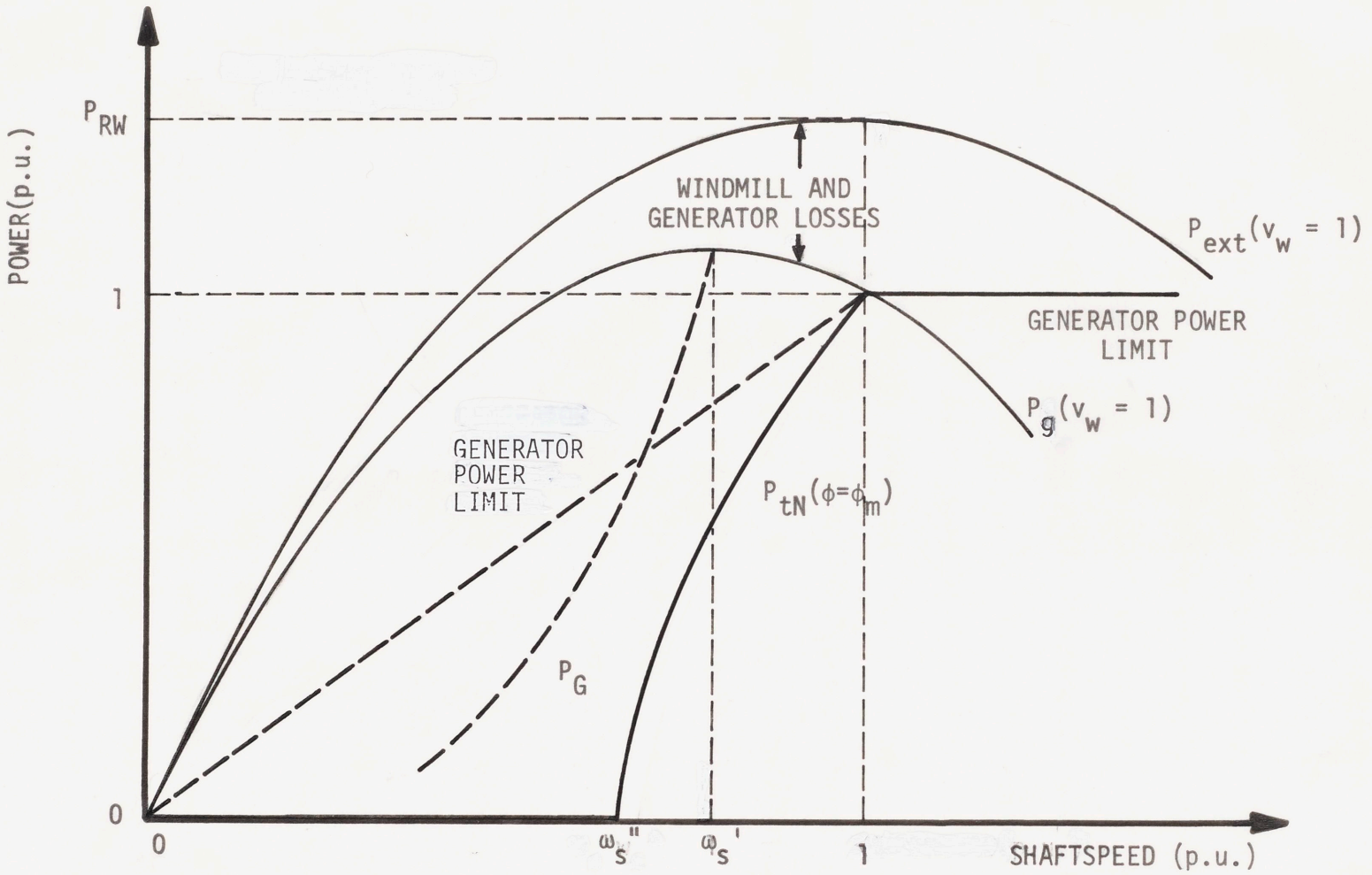

Figure 11 Power System Characteristics at Rated Wind Velocity

referred to as the "input" characteristic for that specific point in the system. Thus P_{ext} and P_g are, respectively, the windmill and generator-terminal "input" characteristics.

The curve, P_{tN}, in Figure 11, denotes the electrical power-speed characteristic of the generator. This curve is given by substituting Eqs. 7 and 9 into Eq. 8. The P_{tN} characteristic in Figure 11 is plotted for maximum machine flux ($\phi = \phi_m$) and nominal battery characteristics ($V_{BN} = V_{BN(NOM)}$, $R_{BN} = R_{BN(NOM)}$). Again, for convenience, a power-speed characteristic relating power, at a point in the power system, to operating shaftspeed, generator flux level and charging circuit parameters will be referred to as the "output" characteristic for that point in the system. Thus P_{tN} is the generator terminal "output" characteristic. The curve P_G will be introduced later.

Below the shaftspeed $\omega_s" = (V_{BN(NOM)} + 4v_d)/\phi_m$, calculated from Eq. 7 with $i_t = 0$ and $\phi = \phi_m$, the generator output is zero. At these speeds the generator cannot produce enough voltage to charge the batteries. Above $\omega_s = 1$ the generator output is 1 per unit due to generator power limitations.

System steady-state operation must occur at the intersection of the P_g and P_{tN} curves, i.e., intersection of the "input" and "output" characteristics. At this point, the power supplied by the windmill to the generator terminals exactly equals the power supplied by the generator to the battery charging circuit. If, at some time, P_g is not equal to P_{tN} then a dynamic response results in the system causing a change in operating shaftspeed driving the system to where $P_g = P_{tN}$,

assuming a stable system. Dynamic system behavior will be treated in Section II.3.

Returning to Figure 11, notice that generator power output appears to be improved by operating the power system at the lower shaftspeed, ω_s'. This is due to windmill and generator losses being significantly less at this lower shaftspeed. Since steady-state system operation occurs at the intersection of the P_g and P_{tN} curves then altering system operation from $\omega_s = 1$ to $\omega_s = \omega_s'$ requires displacing the P_{tN} curve to the left in Figure 11. As was shown in Section I.2.c, this is achieved by either increasing generator field excitation or decreasing battery load voltage. However, since the P_{tN} characteristic in Figure 11 is designed for maximum machine flux, then P_{tN} cannot be further displaced to the left via field excitation control. Also, due to generator current limitation, no advantage can be gained by decreasing the nominal battery voltage. This can be easily seen by realizing that system operation cannot occur above the generator power limit lines in Figure 11, i.e., where both rated generator field and armature currents result. By altering nominal battery voltage P_{tN} is dispaced leftwards only underneath the generator power limit line. Since the peak of the $P_g(v_w = 1)$ curve is located above the generator power limit line then system operation cannot occur at this point of maximum generator output.

Considering the generator limits discussed above, the maximum power output for the power system, depicted in Figure 11 for rated wind velocity, is where the generator power limit line intersects the $P_g(v_w = 1)$ curve. The result is that generator power output cannot be maximized at rated wind velocity, i.e., operation cannot occur at the

peak of the $P_g(v_w = 1)$ curve. However, one may suggest redesigning the power system such that generator efficiency is maximized, i.e., locating the peak of $P_g(v_w = 1)$ at $\omega_s = 1$. This is possible by relocating the peak-power shaftspeed of the $P_{ext}(v_w = 1)$ curve to a higher per-unit shaftspeed.* However, with this peak-power shaftspeed moved away from $\omega_s = 1$, the power extracted from the wind at this shaftspeed and at rated wind velocity is now less than P_{RW}. This reduced power extraction at rated shaftspeed becomes insufficient to support both rated generator power and system power losses. Thus generator output is reduced. To return generator output to rating requires increasing the peak of the P_{ext} curve until wind power extraction, at $\omega_s = 1$, returns to the value P_{RW}, i.e., the extraction necessary to simultaneously achieve rated generator output and support losses. Figure 12 depicts this new windmill system design. Note that in Figure 12, "b", the peak of the $P_{ext}(v_w = 1)$ curve, is now greater than P_{RW}. Since the parameter "b" is a measure of windmill size then the redesigned windmill system requires a larger and, therefore, more costly windmill to extract the power P_{RW} at rated wind velocity and shaftspeed. Since a larger windmill is undesirable, the windmill power system design depicted in Figure 11, where the peak of the $P_{ext}(v_w = 1)$ curve occurs at $\omega_s = 1$, is the more cost-efficient of the two designs. With this design the generator cannot operate at maximum efficiency at rated wind velocity, i.e., operation cannot occur at the peak of $P_g(v_w = 1)$. However,

*Relocating the peak-power shaftspeed of P_{ext} is done by increasing the gearing ratio between windmill and generator shafts.

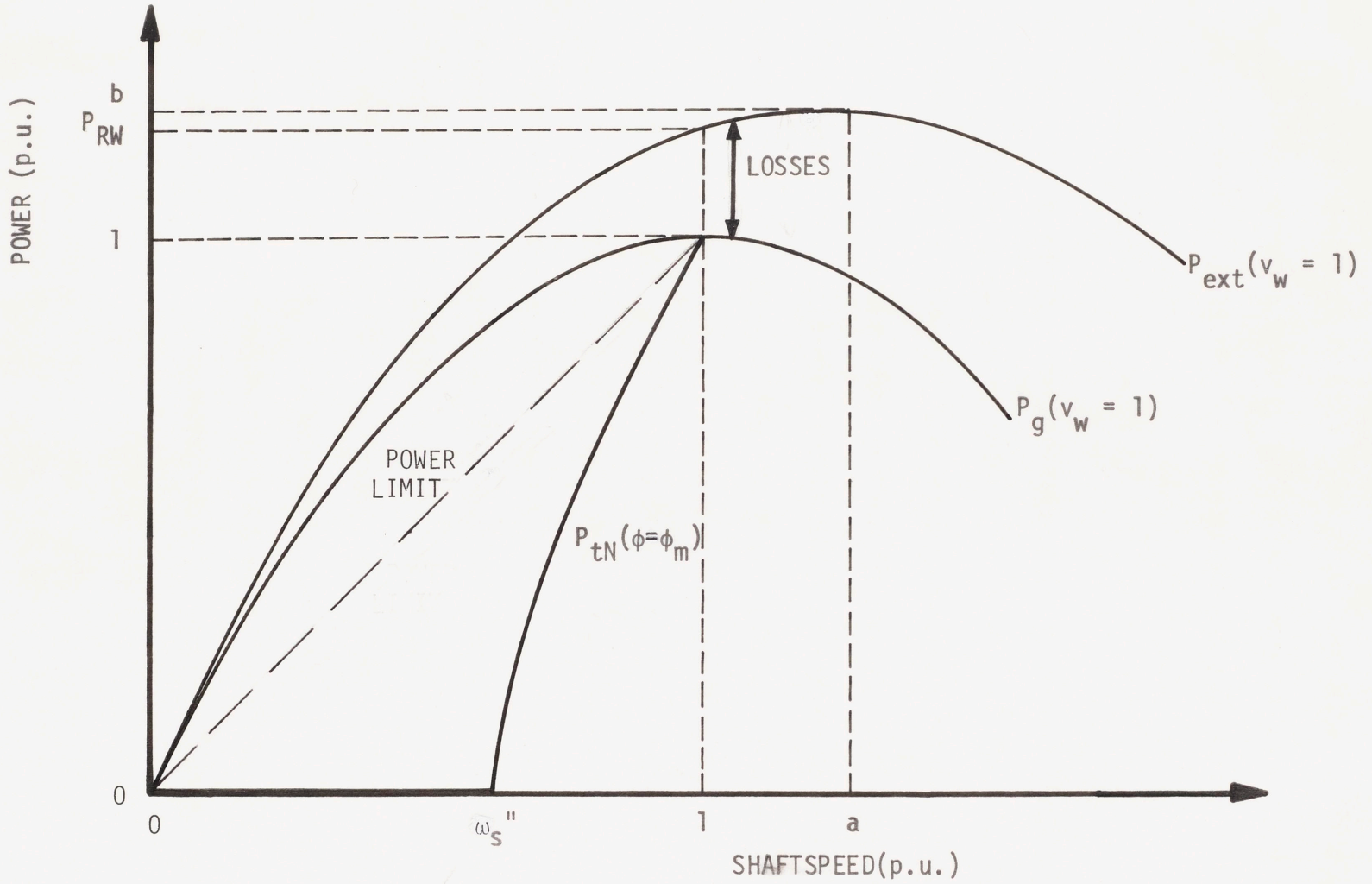

Figure 12 Redesigned Windmill System

the system design does guarantee rated generator output at rated wind velocity with the smallest windmill, i.e., smallest value for the peak of $P_{ext}(v_w = 1)$. Appendix B presents the implementation of the design procedure developed in this section on a physical scale model system.

II.2 Power System Steady-State Analysis

In the previous section the windmill power system was designed to deliver rated generator output at rated wind velocity. The most cost-efficient design was developed. The objective of this section is to maximize the energy transfer from the wind to the batteries for all wind velocities below rated. This is done in coordination with the system design constraints developed in the previous section.

Steady-state system operation occurs at the intersection of the relevant input and output power-vs-speed characteristics for the system, i.e., P_g and P_{tN} in Figure 11 for the case of generator terminal power at rated wind velocity. As wind velocity decreases, the position of the P_g curve moves downward since wind power extraction at all operating shaftspeeds is reduced. A line may be drawn joining the peaks of the P_g curves as wind velocity decreases. This curve is shown in Figure 11 as P_G.* However, as wind velocity varies, the P_{tN} characteristic remains unchanged since none of the parameters in the generator-output circuit has changed. As a result of P_{tN} remaining

*As shown in Section I.1.a, the peak of the P_{ext} curve decreases with the cube of wind velocity. Also, the peak-power shaftspeed of P_{ext} decreases in proportion to wind velocity. In a well designed system, power losses are not expected to dominate system steady-state behavior. Thus the peak of the P_g curve is expected to behave in a manner similar to that of the P_{ext} curve as wind velocity varies.

fixed, the system operation must occur along this P_{tN} curve for all wind velocities unless a charging-circuit parameter is altered, i.e., generator flux level or battery voltage. Also note that as wind velocity decreases the peak of the P_g curve, moving down P_G in Figure 11, moves continually further away from P_{tN}. Since system steady-state operation occurs where P_g and P_{tN} intersect, the result is lower system efficiency as wind velocity decreases, i.e., operation is further away from P_G.

By decreasing the battery voltage impressed on the generator output through the discrete switching of battery sections, the possible region of system operation is increased, as was shown in Section I.2.d and Figure 6. In theory, the possible region of system operation can include the total area underneath the generator power limit lines in Figure 11. However, this requires the ability to vary battery load voltage continuously from zero to full nominal voltage. If this voltage control were possible then maximum generator output can be achieved for that range of wind velocities where P_G, i.e., the locus of the peaks of the P_g curves as a function of wind velocity, falls below the generator power limit line (see Figure 11). In this case no other load control is necessary since system operation can be relocated anywhere under the generator limit.

However, the fine incrementation of battery load voltage is costly. Many battery switches are required and the electrical rotation of the battery sections to maintain uniform battery state-of-charge grows more complex with increasing number of sections. Also the control of generator field excitation is available to vary

the generator output characteristic, as shown in Figure 6 and related text. Therefore, a battery bank consisting of many battery sections may not result in the most cost-efficient system even though generator operating region is increased. A cost-benefit analysis may be required to determine the exact number of battery sections to employ in the system.

For the remainder of this section, an analytical procedure will be developed to evaluate the increased system efficiencies associated with the abilities to alter both battery load voltage and generator field excitation as a function of varying wind velocity. An important issue is how to coordinate the use of these controls such that "good" system efficiency is maintained.

The desired system requirement is not just the maximization of generator power output but the maximization of the power absorbed by the batteries. This is not always possible due to generator limitation, as was shown in the case of system design at rated wind velocity. However, one objective of this analysis is to determine when system inefficiencies occur and their affect on system power conversion capability.

The power absorbed by the batteries is the product of battery voltage and charging current. For a given battery state-of-charge the internal voltage of a battery section can be considered constant. Thus, for a given number of charging section, the desired objective is to locate the operating shaftspeed where battery charging current is a maximum. If this can be done for all wind velocities and all battery states-of-charge then, by measuring these variables, the desired operating shaftspeed can be determined. Once this shaftspeed is

known for a given battery-section load, generator field current control can be used to alter system operating point until the desired shaftspeed is attained.

Using the power system models developed in Chapter I, the steady-state power absorbed by the batteries can be expressed as a function of wind power extraction less all system losses.

Power Absorbed by Batteries $\equiv P_B$

= Wind Power Extracted - Windmill Mechanical Power Losses

- Generator Mechanical Power Losses - Generator Core Power Losses - Charging Circuit Power Losses

$$P_B = P_{ext} - P_{\ell wm} - P_{\ell gm} - P_{\ell gc} - P_{\ell ckt} \tag{30}$$

where $P_{ext} = P_{RW} v_w (2 v_w \omega_s - \omega_s^2)$

$$P_{\ell wm} = C_{w1} \omega_s + C_{w2} \omega_s^2$$

$$P_{\ell gm} = C_{g1} \omega_s + C_{g2} \omega_s^2$$

$$P_{\ell gc} = P_{\ell h} + P_{\ell e} = C_h \phi^2 \omega_s + C_e \phi^2 \omega_s^2$$

$$P_{\ell ckt}^{*} = R_x i_b^2 + 4 v_d i_b$$

*The charging circuit losses are just the power losses due to resistances and diode drops in the circuit.

All quantities have been previously defined in Chapter I. For reference, the equations used are Eqs. 3, 11, 12, 13, 29, and part of Eq. 7.

The power into the batteries is also equal to the product of battery voltage and charging current, i.e.,

$$P_B = V_{BM} i_b \tag{31}$$

The battery charging current, i_b, was previously derived as a function of charging circuit parameters and is reproduced here

$$i_b = |i_t| = \frac{-V_L R_x + \sqrt{\omega_s^2 \phi^2 (R_x^2 + X^2) - V_L^2 X^2}}{R_x^2 + X^2} \tag{7}$$

where $V_L = V_{BM} + 4v_d$

$$R_x = R_{BM} + R_s + R_{eff}'$$

$$X = \omega_s L_x$$

Substituting Eq. 7 into Eq. 31 results in a battery power-vs-speed characteristic that is a function of generator field flux, battery characteristics, and charging circuit parameters. This equation is the battery "output" characteristic.

However, Eq. 7 can be solved for generator flux yielding

$$\phi^2 = \frac{(R_x^2 + X^2) i_b^2 + 2 V_L R_x i_b + V_L^2}{\omega_s^2} \tag{32}$$

Eqs. 31 and 32 can be substituted into Eq. 30 resulting in the following quadradic equation for i_b.

$$\left[\frac{(C_h + C_e\omega_s)(R_x^2 + X^2)}{\omega_s} + R_x \right] i_b^2 + \left[\frac{2V_L R_x (C_h + C_e\omega_s)}{\omega_s} + V_L \right] i_b$$

$$- \left[P_{RW} v_w (2v_w\omega_s - \omega_s^2) - K_1\omega_s - K_2\omega_s^2 - \frac{V_L^2 (C_h + C_e\omega_s)}{\omega_s} \right] = 0 \tag{33}$$

where $K_1 = C_{w1} + C_{g1}$ and $K_2 = C_{w2} + C_{g2}$.

Solving Eq. 33 for i_b yields

$$i_b = \frac{-B + \sqrt{B^2 - 4AC}}{2A} \tag{34}$$

where A, B, and C are respectively the i_b^2, i_b and i_b^0 coefficients in Eq. 33. Also the nonextraneous solution has been chosen.

Substituting Eq. 34 into Eq. 31 results in another battery power-vs-speed characteristic that is now a function of wind velocity, battery characteristics, and system parameters. This equation is the battery "input" characteristic.

Differentiating Eq. 34 with respect to shaftspeed, setting the result to zero, and solving for shaftspeed results in the desired operating shaftspeed for the system as a function of wind velocity, battery characteristics, and system constants. By sensing the error between actual and desired shaftspeed, the generator field current can

be driven in the appropriate direction until system operation is relocated at the desired system shaftspeed. In this way, maximum power transfer from the wind to the batteries can be maintained for as long as no generator constraints, or limitations, are reached.

A decision to alter the number of charging battery sections is considered when a generator constraint is reached, i.e., generator flux saturation or generator armature current limitations. Generator flux saturation occurs at low wind velocities where the generator cannot produce enough voltage to charge the batteries. Here a decision is made to decrement battery voltage such that battery charging is again possible. Armature current limiting occurs at high wind velocities when the battery voltage is too low to accept the power converted from the wind. Here a decision is made to increment battery voltage such that desired system loading can again be achieved. In these limiting cases field current alteration can no longer drive the system to desired operating shaftspeed. The altering of battery voltage, however, results in a relocation of system operating region, as was described in Section I.2.c. In this new region of operation field current control may again be used either to drive system operation to maximum efficiency or, due to constraints associated with the new operating region, to improve system efficiency from its value prior to battery switching.

The decision when to alter battery voltage must also take into account system power losses. During switching a redistribution of system losses occurs due to changes in both generator flux and armature current levels. Thus a decision on when to switch must consider expected values of system power losses such that system efficiency is increased, and not decreased, by battery switching.

Before closing this section of the chapter, a few observations will be made regarding the effects of battery state-of-charge on power system steady-state behavior.

Both internal battery voltage and resistance vary as a function of battery state-of-charge. Appendix C shows typical variations in these parameters for the battery banks to be employed in the physical scale-model system (Chapter 4). Previously noted in Section I.2.c was that variations in internal battery parameters effect changes in the regions of system operation.

However, battery state-of-charge also affects the desired system operating point. This can be seen from the battery input characteristic, i.e., Eq. 34 substituted into Eq. 31. Since the charging current, i_b in Eq. 34, is a function of battery parameters, variations in the peak value of i_b, as a function of these parameters, is expected. The result is that the desired system operating point, i.e., operating shaftspeed, varies as a function of battery state-of-charge. Thus to maintain maximum system efficiency the measurement of battery state-of-charge is necessary such that the system can be driven to the desired operating shaftspeed. However, this measurement is difficult to make accurately. Therefore operating at the peak of the battery input characteristic may not always be possible.

One possible way to estimate the battery parameters is by measuring battery open-circuit-voltage and internal resistance* when a battery section is rotated out of the charging circuit.

*Internal resistance can be measured by noting the difference in battery terminal voltage before and after the charging current is removed and then dividing by the charging current.

However, before an intricate control scheme is constructed to calculate the desired system operating point as a function of battery state-of-charge, it is necessary to know how system efficiency is affected by these varying battery parameters.

The equations developed in this section, Eqs. 30 to 34, can be used to determine the desired system operating shaftspeed as a function of wind velocity, battery bank characteristics, system parameters and loss coefficients. Also from these equations acceptable regions of system operation can be calculated. With this information, it is possible to determine when maximum power transfer from the wind to the batteries is achievable, i.e., when generator constraints do not compromise system power conversion capability.

The equations developed in this section will be directly applied in Chapter III to a computer simulation of a physical scale model power system. Through this application, a better understanding of steady-state system operation can be obtained. Issues to be resolved include:

1) When to switch battery bank voltage such that maximum system efficiency is always attained.

2) The effect of battery state-of-charge on system operation.

3) The number of battery sections to incorporate into the system.

II.3 Power System Dynamic Analysis

The previous section showed that maximum windmill power conversion is attained by varying generator load, via generator field current control, until desired operating shaftspeed is reached. Also, via battery voltage switching, system operation can be optimized with respect to wind power transfer for larger ranges of wind velocities.

The operating shaftspeed of the system cannot, however, change instantaneously. Associated with the coupled windmill-generator shaft is an inertia which prevents desired shaftspeed changes to occur until the required kinetic energy is stored in the rotating system.

The rate of change of kinetic energy in the windmill system is the difference between the power extracted from the wind and the sum of the generator power output and all the power losses associated with the windmill and generator. Thus, using Eqs. 3, 7, 8, 9, 11, 12, 13, and 29, one can write

$$\text{Rate of Change of Kinetic Energy} = \frac{1}{2}J\frac{d\omega_s^2}{dt}$$

$$= P_{ext}(v_w,\omega_s) - P_{\ell wm}(\omega_s) - P_{\ell gm}(\omega_s) - P_{\ell e}(\phi,\omega_s)$$

$$- P_{\ell h}(\phi,\omega_s) - P_t(i_b,M,soc) \qquad (35)$$

where all the power components have been expressed as a function of their varying parameters. The variable, J, is the moment of inertia of the coupled windmill-generator shaft. The variable, "soc" (state-of-charge), is a number varying between 0 and 1 depending on the

battery state-of-charge, i.e., fully discharged to fully charged. The variable "soc" relates variations in the battery parameters, from nominal values, to the state-of-charge of the battery sections. Thus the internal voltage and resistance of the battery sections in the charging circuit may be expressed as

$$V_{BM} = M \cdot V_{BS(NOM)} \cdot (1 + \varepsilon_1)$$

$$R_{BM} = M \cdot R_{BS(NOM)} \cdot (1 + \varepsilon_2) \tag{36}$$

where $\varepsilon_1 = \varepsilon_1(soc)$; $\varepsilon_2 = \varepsilon_2(soc)$.

Appendix C shows how ε_1 and ε_2 are related to battery state-of-charge in an actual battery bank.

From the redefinitions of the battery parameters expressed in Eq. 36, the current flowing in the charging circuit may be written from Eq. 7 as

$$i_b = i_b(\omega_s, \phi, M, soc) \tag{37}$$

Using Eq. 37, Eq. 35 may be written as

$$\frac{1}{2} J \frac{d\, s^2}{dt} = P_{ext}(v_w, \omega_s) - P_{\ell m}(\omega_s) - P_{\ell gc}(\phi, \omega_s) - P_t(\omega_s, \phi, M, soc) \tag{38}$$

where $P_{\ell m} = P_{\ell gm} + P_{\ell wm}$ and $P_{\ell gc} = P_{\ell e} + P_{\ell h}$.

In review, Eq. 38 shows that the steady-state operating shaftspeed of the system, obtained from setting $\frac{d}{dt}$ to zero, is a function of the generator flux level and the state of the battery bank load. By varying generator flux, or battery bank voltage, the operating shaftspeed can be altered. However, due to the derivative in Eq. 38, the operating shaftspeed cannot change instantaneously.

The generator field flux level in Eq. 38 is an increasing function of generator field current, i_f, i.e.,

$$\phi = \phi(i_f) \quad ; \quad \frac{\partial \phi}{\partial i_f} > 0 \tag{39}$$

If the assumption is made that the time constant associated with the generator field winding, i.e., L_f/R_f in Figure 3, is small compared to the rate of change of an applied variation in the field terminal voltage, v_f, then an integral controller can be used to control the current in the field winding. The integral controller is of the form

$$i_f = \int \left(\frac{\omega_s - \omega_{so}}{\tau_f}\right) dt \tag{40}$$

where τ_f is a constant. This control drives the field current in proportion to the error between actual and desired shaftspeed, i.e., $\omega_s - \omega_{so}$. The value of ω_{so} was shown to be derivable from Eq. 34 by setting $\frac{\partial i_b}{\partial \omega_s}$ to zero and solving for shaftspeed. The result is the operating shaftspeed where maximum charging current flows. This shaftspeed is a function of wind velocity and battery bank characteristics, i.e.,

$$\omega_{so} = \omega_{so}(v_w, M, soc) \tag{41}$$

The feedback control implied by Eq. 40 adjusts generator load until the desired point of system operation is reached, when $\omega_s = \omega_{so}$. The sign of the feedback is correct. If desired shaftspeed is less than actual shaftspeed then, through the implementation of Eq. 40, generator field current is increased. The result is an increase in generator loading leading to a decrease in system shaftspeed.

Since all the variables, in Eq. 40 are per-unitized, and thus unitless, the constant τ_f has the units of time and may be considered as a field current time constant. The value of τ_f controls the speed at which the field current reacts to errors between actual and desired system shaftspeed.

The closed-loop control system described by Eqs. 38 to 41 is schematically shown in Figure 13. The function f' is the right-hand side of Eq. 38.

Note that the system depicted in Figure 13 is second order in nature due to the two integrations in the control loop. Also note the nonlinearity in the system due to the gain around the loop being a function of system operating point. The loop gain is also proportional to the reciprocal of the field current time constant, i.e., $1/\tau_f$. Thus the relative stability of the system is dependent on the choice of τ_f. operation is further complicated by the nonlinearity in the loop gain. Thus a choice of τ_f leading to "good" system performance at one operating point does not guarantee the same performance at another system operating point.

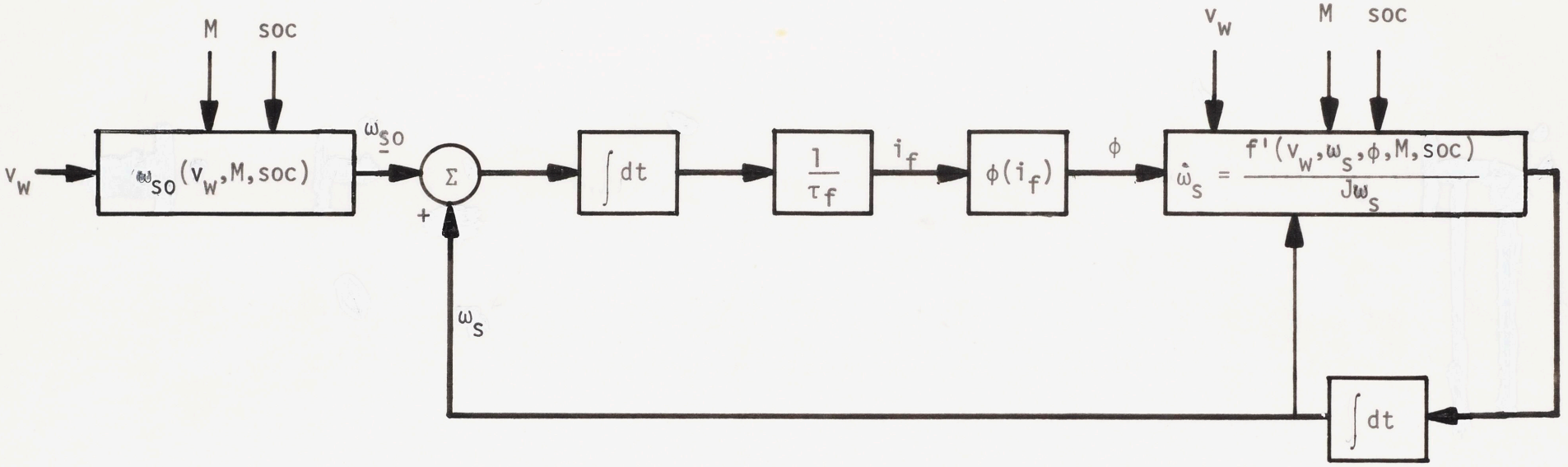

Figure 13 Schematic Diagram of Windmill Control System

The control system of Figure 13 is still incomplete. Not included are the generator armature current and field flux constraints. The field flux constraint may be added by way of a dynamicless limiting on generator field current. An armature current limit may also be added by reducing field drive when rated current is exceeded. However, since the armature current is dependent on the value of the parameters within the control loop, then the limiting of armature current, via field current reduction, creates another feedback path in the control system. This additional feedback path as well as the field current limit are shown in the augmented control system of Figure 14.

The function f'' relates the generator armature current to control loop variables given by Eq. 7. The switch in the feedback paths emphasizes that the armature current path becomes the dominant control loop when rated armature current is exceeded. The reason for a switch instead of a summing junction is to prevent competition between the two feedback loops. When the armature current is exceeded, then the field current control law becomes

$$i_f = -\int \left(\frac{i_b - 1}{\tau_{ac}} \right) dt \quad ; \quad i_b > 1 \tag{42}$$

The constant, τ_{ac}, has an effect similar to that of the field current time constant, τ_f, i.e., τ_{ac} controls the gain of the armature current feedback path. Thus the relative stability of this loop is dependent on the choice of τ_{ac}.

Two types of dynamics are associated with the control system of Figure 14. The first is system behavior related to changes in

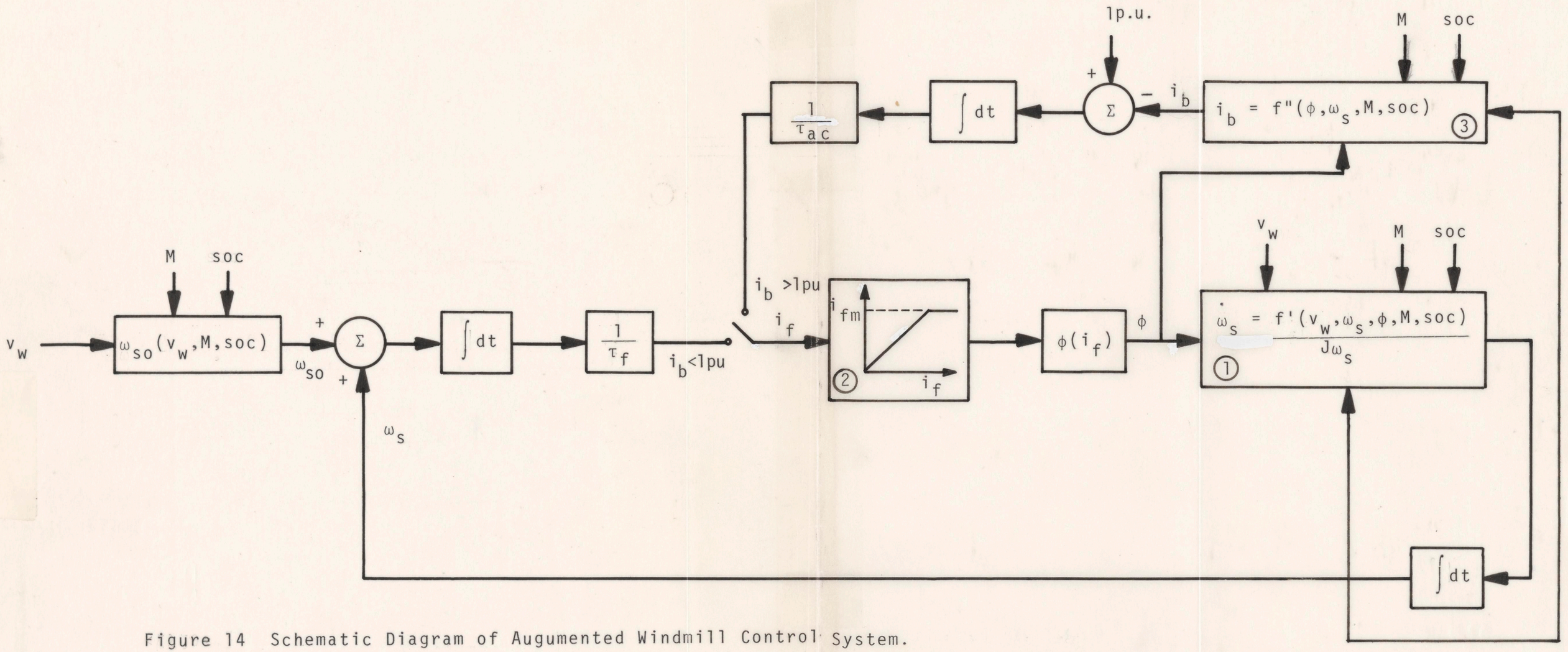

Figure 14 Schematic Diagram of Augumented Windmill Control System.

3 1/4"

wind velocity alone. The objective of the control system, in this case, is to allow system operating point to track changes in wind velocity, and thus desired operating point, with "good" dynamic performance.

The second type of system dynamics is related to the discrete switching of battery bank voltage. The decision to switch battery bank voltage, i.e., discretely varying M in the control system, was discussed in Section II.2. However, as seen from the generator output characteristics, Figure 6, an instantaneous change in battery voltage produces a substantial change in the generator load characteristic. In this case, "good" system performance may require that the system loop gain be different from its value in the case of wind velocity variations. Changing system loop gain is achieved by varying the field current time constant, τ_f.

To study the effects of the dynamics associated with changes in both wind velocity and battery bank voltage, the control system of Figure 14 has been simulated on a digital computer. The results of the simulation for an actual scale model windmill power system are discussed in Chapter III.

CHAPTER III

COMPUTER SIMULATION OF STEADY-STATE AND DYNAMIC BEHAVIOR OF WINDMILL POWER SYSTEM

The purpose of this chapter is to employ the steady-state and dynamic system equations, developed in the previous chapter, in a computer simulation of the scale model windmill power system. The system parameters used in both the steady-state and dynamic simulations have been empirically determined from the actual elements of the physical scale model system. These parameters and their methods of calculation are shown in Appendices C, D, and E.

III.1 Steady-State Windmill Power System Simulation

This section deals with calculating desired steady-state system operation such that most efficient wind-to-battery power transfer is attained. Issues of concern in this section are: 1) System inefficiencies due to generator limitations in field flux and armature current, 2) the effect of battery state-of-charge on system operation, 3) when to switch battery bank voltage such that maximum system efficiency is maintained, 4) the number of battery sections to incorporate in the system, and 5) effects on system efficiency and dynamics due to increased curvature of the windmill C_p curve.

From the equations developed in Chapter II, the allowable regions of generator operation can be calculated, i.e., using Eqs. 7 and 31. Secondly, from differentiating Eq. 34, the location of the peak of the input power characteristic for the batteries, where maximum system power

transfer is attained, can be calculated. Thirdly, from these equations both the battery input and output characteristics can be calculated as a function of the battery bank parameters, M and soc. The expected result is characteristics similar to those shown in Figure 6. Lastly, the equations provide information as to when maximum system efficiency cannot be achieved.

From solving

$$\left.\frac{\partial i_b(v_w,\omega_s,M,soc)}{\partial \omega_s}\right|_{\omega_s = \omega_{so}} = 0 \text{ for } \omega_{so},$$

where $i_b(v_w,\omega_s,M,soc)$ is Eq. 34, the desired operating shaftspeed is determined. Substituting ω_{so} into Eq. 34 results in the maximum charging current, i_{bm}, as a function of wind velocity and battery bank characteristics, i.e.,

$$i_{bm} = i_b(v_w,\omega_{so},M,soc) \tag{43}$$

If i_{bm} is less than the rated generator armature current, then the generator current constraint has not been violated. Also, by substituting i_{bm} and ω_{so} into Eq. 32, the operating generator flux level can be calculated. If this flux level is less than the maximum flux level of the machine, ϕ_m, then the generator field constraint is not violated. If both the generator field and armature constraints are not exceeded, for a specific wind velocity and battery load, then maximum power transfer for the system is achievable. Thus the system can operate at

the peak of the battery input characteristic where, by definition, maximum system operating efficiency is achieved.

However, if i_{bm} exceeds one per unit at a certain wind and battery bank condition, then system operating efficiency must be decreased such that i_b is maintained at its rating. This is done by decreasing generator field excitation and thus decreasing generator loading. In this case, the shaftspeed where 1 per-unit charging current is maintained, for the particular wind and battery load condition, can be calculated from Eq. 34 with i_b set to 1. For steady-state system operation away from the peak of the battery input characteristic, a quantitative measure of operating efficiency is needed to evaluate system performance. This operating efficiency will be defined as the ratio of actual power absorbed by the batteries, in the presence of generator constraints, to the maximum power that can theoretically be absorbed had no constraints existed. This maximum theoretical power is the peak of the battery input characteristics. For convenience, system operating efficiency will be abbreviated as η_{op}.

During those wind velocity and battery bank conditions that result in generator armature current limiting the maximum power delivered to the batteries is given by Eq. 31 with $i_b = 1$. For the same conditions, the theoretical maximum power transfer is also given by Eq. 31 but with i_b replaced by Eq. 43. Thus system operating efficiency during generator armature current limiting is

$$\text{Operating Efficiency} = \frac{\text{Actual Stored Power}}{\text{Theoretical Maximum Power}} \equiv \eta_{op}$$

$$\eta_{op} = \frac{V_{BM} \cdot 1}{V_{BM} i_{bm}} = \frac{1}{i_{bm}} \quad ; \quad i_{bm} > 1 \tag{44}$$

System operating efficiency can also be calculated for the wind and battery bank conditions that result in generator flux saturation. Generator flux saturation is known to occur for those wind velocities and battery bank conditions when the solution of Eq. 32, with $i_b = i_{bm}$ (maximum theoretical charging current) and $\omega_s = \omega_{so}$ (shaftspeed where i_{bm} occurs) yields a generator flux that is larger than ϕ_m. Here maximum system efficiency is prevented by saturation of generator loading ability. Under these conditions, both generator operating current and shaftspeed can be obtained by simultaneously solving Eqs. 32 and 34 with $\phi = \phi_m$, the maximum machine flux level. The resulting operating current, to be referred to as i_b', is used to calculate system operating efficiency for the condition of generator flux saturation. This efficiency, as defined in Eq. 44, is

$$\eta_{op} = \frac{V_{BM} i_b'}{V_{BM} i_{bm}} = \frac{i_b'}{i_{bm}} \quad ; \quad \phi = \phi_m \tag{45}$$

From the definition of system operating efficiency, if neither generator current limiting or flux saturation occurs, then $\eta_{op} = 1$, its maximum value.

Now that system operating efficiency has been defined, this quantity can be used to determine the steady-state performance of any windmill power system.

The equations used in calculating and evaluating windmill power system operation, developed above and in Section II.2, can be employed in a computer simulation of an actual system. For the remainder of this section, the results of such a simulation are presented for the constructed scale model system. The elements of the scale model system, i.e., windmill, generator, and battery bank have been designed according to the design procedure in Section II.1 (see Appendix B). All empirical data for the simulation are shown in Appendices C, D, and E.

For this presentation of power system steady-state behavior, the battery bank consists of two discrete battery sections. As will be seen in this section, system efficiency is not substantially improved by employing more than two battery sections. However, the observations made for this two battery-section system are general and can be directly applied to a system with a larger number of sections.

Figures 15, 16, and 17 show the results of a steady-state simulation for a battery bank consisting of two nominally charged battery sections. Figure 15 shows generator terminal input and output characteristics for the simulated system. The curves P_{g1} and P_{g2} in Figure 15 are the input characteristics for one and two charging battery sections, respectively. Several of these curves are plotted in the figure for different values of wind velocity. The curves P_{G1} and P_{G2} are the lines that join the peaks of the input characteristics again for one and two charging battery sections, respectively. For a

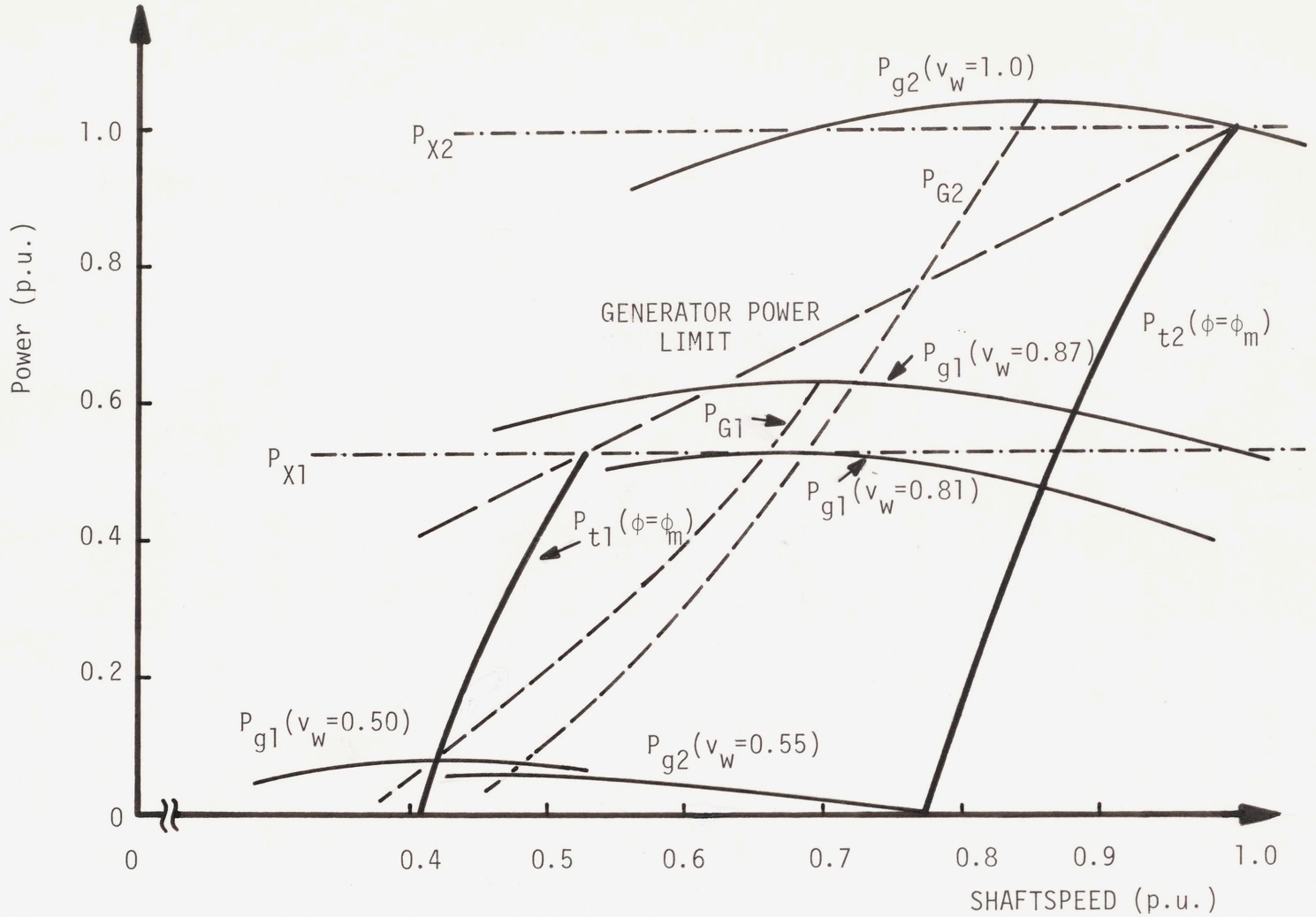

Figure 15 Generator Input and Output Characteristics

totally lossless system P_{G1} and P_{G2} coincide (see discussion, Appendix A). However, P_{G1} and P_{G2} do not coincide due to different power losses when different numbers of battery sections are charging.

The lines P_{X1} and P_{X2} in Figure 15 are the maximum generator outputs for one and two battery-section loads, respectively. Load cannot be increased above these lines without exceeding the generator armature current limit. Lastly, the curves P_{t1} and P_{t2} are the generator output characteristics for one and two charging battery sections, respectively. In Figure 15, P_{t1} and P_{t2} are plotted for maximum machine flux level.

As previously discussed in Section I.2.c system operation, with one charging battery section, must occur to the right of $P_{t1}(\phi = \phi_m)$ and below P_{X1}. Similarly for two charging sections, operation occurs to the right of $P_{t2}(\phi = \phi_m)$ and below P_{X2}. Thus, for one charging section, maximum generator efficiency can occur only where P_{G1} falls within the allowable region of generator operation. From Figure 15, the range of wind velocities where this maximum generator efficiency occurs is $0.50 \leq v_w \leq 0.81$. Only between these wind velocities do the peak of the $P_{g1}(v_w)$ curves fall within the allowable generator operating region. For $v_w \leq 0.5$ system operation follows the $P_{t1}(\phi = \phi_m)$ characteristic and for $v_w \geq 0.81$ system operation follows the P_{X1} line. However, at $v_w = 0.87$ system operation, for one charging battery section, is forced to 1 per-unit shaftspeed, i.e., the intersection of the $P_{g1}(v_w = 0.87)$ and P_{X1} curves of Figure 15. Any higher wind velocities result in shaft overspeed.

For two charging battery sections P_{G2} is never located to the right of $P_{t2}(\phi = \phi_m)$. System operation then occurs either on the $P_{t2}(\phi = \phi_m)$

characteristic or at zero generator output for $v_w \leq 0.55$, where the P_{g2} characteristic no longer intersects $P_{t2}(\phi = \phi_m)$ in Figure 15. Thus, as predicted in Section II.2, maximum generator efficiency is never achieved for full nominal battery bank voltage.

Figure 16 shows both the generator power output and stored battery power as a function of wind velocity. These curves are plotted for the same power system depicted in Figure 15. P_{T1} and P_{T2} are the generator power outputs for one and two charging battery sections, respectively. P_{B1} and P_{B2} are the stored battery powers for, again, one and two charging sections, respectively. The power difference between respective P_T and P_B curves reflects power losses in the charging circuit including internal battery losses. All the curves in Figure 16 have been plotted only up to those wind velocites where rated system shaftspeed is attained for the respective battery loads. As seen in Figure 15, rated shaftspeed is attained at $v_w = 0.87$ and $v_w = 1$ for one and two sections, respectively.

Note the flat portions of the P_{T1} and P_{B1} curves in Figure 16. These portions of the curve are due to generator armature current limiting. With reference to Figure 15 this portion of P_{T1} and P_{B1} corresponds to generator operation along P_{X1} for $0.66 \leq \omega_s \leq 1$. Figure 16 also shows that with one battery section charging, energy can be transferred to the battery for all wind velocities above $v_w = 0.36$. For full battery bank load, however, energy can be transferred to the batteries only for wind velocities above $v_w = 0.55$. Lastly, at a wind velocity of $v_w = 0.82$ the P_{B1} and P_{B2} curves intersect. In terms of maximizing power into the batteries, this means

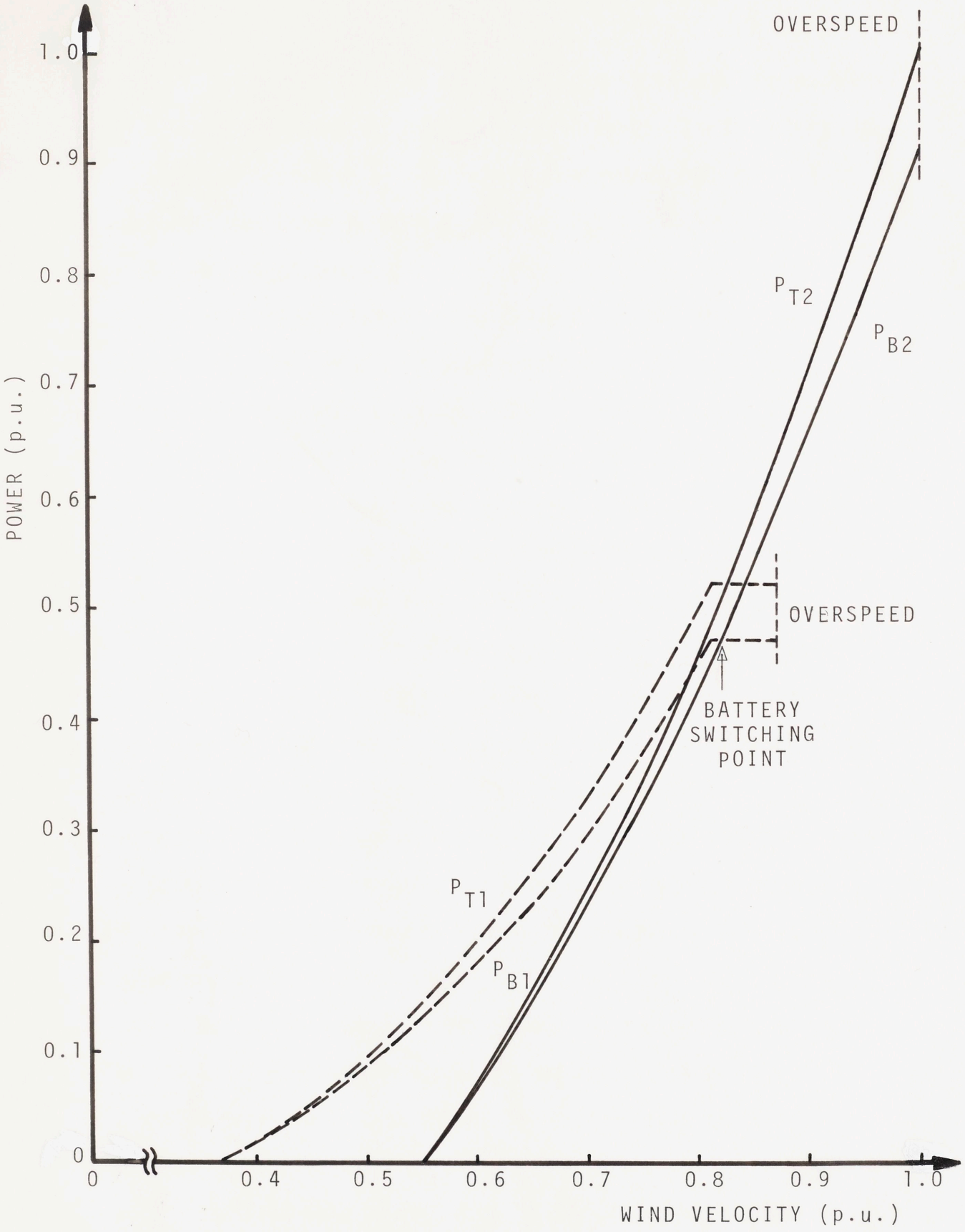

Figure 16 Generator Power Output and Stored Battery Power as a Function of Operating Wind Velocity for a Nominally Charged Battery Bank.

that for all wind velocities below $v_w = 0.82$ only one battery section should be charging, since $P_{B1} > P_{B2}$ for this range of wind velocities. For wind velocities above $v_w = 0.82$, greater system efficiency is achieved with two charging sections, since $P_{B2} > P_{B1}$ for this range of wind velocities.

System operating efficiency, as defined in Eqs. 44 and 45, as well as other system efficiencies are plotted in Figure 17 with respect to operating wind velocity. The curves η_{op1} and η_{op2} are the system operating efficiencies for one and two battery sections, respectively. The curves η_{et1} and η_{et2} are defined as the "generator-terminal extraction efficiencies" for the respective charging sections. This efficiency is the ratio of generator power output to power extracted from the wind. The curves η_{eb1} and η_{eb2} are the "battery extraction efficiencies". This efficiency is the ratio of stored battery power to wind power extraction and thus reflects overall power system efficiency. Note that the difference in respective η_{et} and η_{eb} curves reflect lost system efficiency due to power losses incurred in the battery charging circuit, again including internal battery losses. All the efficiencies in Figure 17 are plotted only up to the rated system shaftspeed.

Note that system operating efficiency for one charging battery section is a maximum for the range of wind velocities $0.5 \leq v_w \leq 0.81$, i.e., the range where P_{G1}, in Figure 15, falls within the allowed generator operating region. Below $v_w = 0.5$ generator flux saturation causes η_{op1} to fall below unity, i.e., where the generator output characteristic, P_{t1} in Figure 15, can no longer track the peaks of

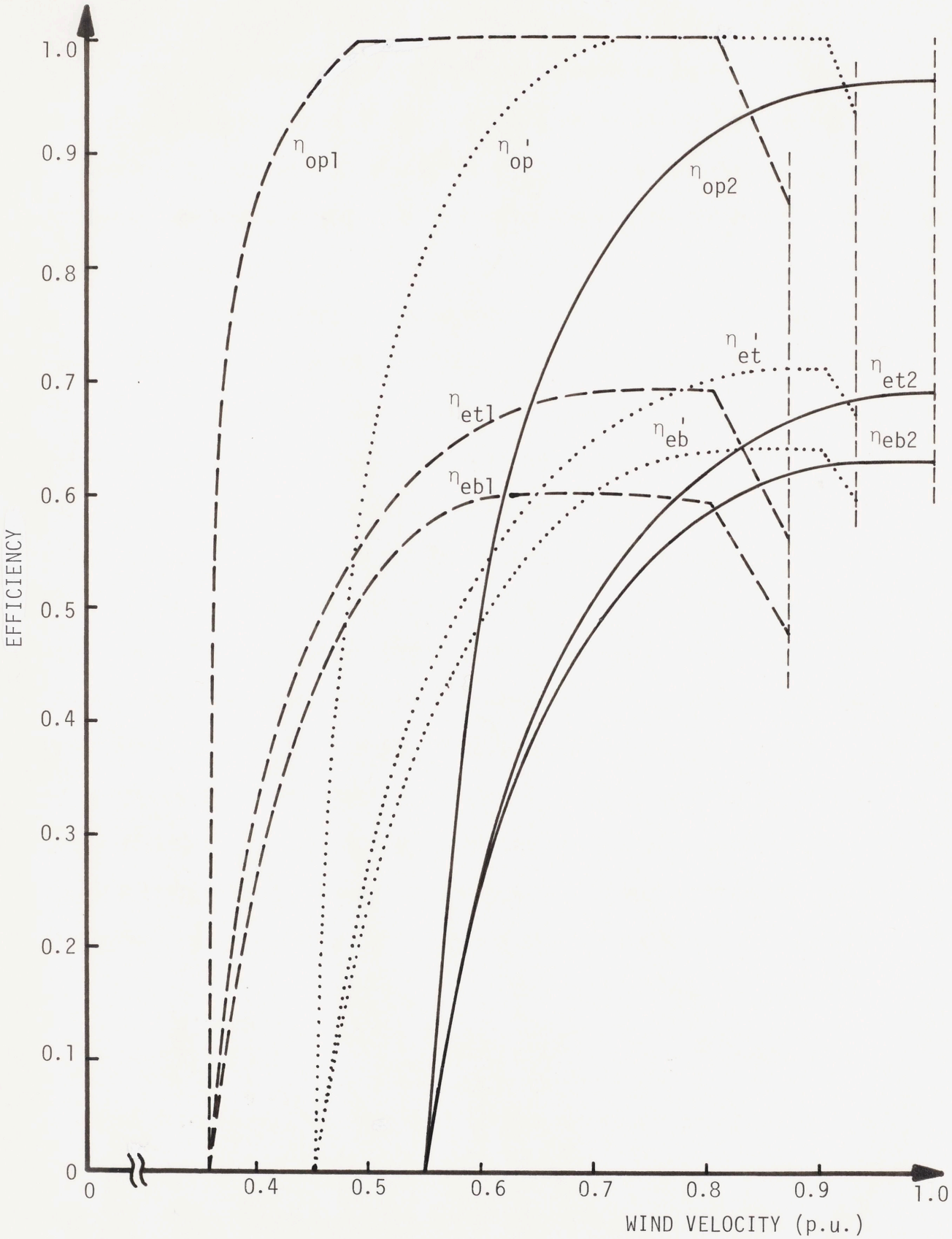

Figure 17 System Operating and Extraction Efficiency as a Function of Operating Wind Velocity

the generator input characteristic, P_{g1}. Above $v_w = 0.81$, η_{op1} again falls below unity due to generator armature current limiting. Here generator operation occurs along the P_{X1} line in Figure 15 instead of the desired P_{G1} curve. Also note that η_{op2} is always below unity due to system operation never occurring along the P_{G2} curve when two battery sections are charging.

One of the questions to be answered in this section is: What improvement in system efficiency is achieved if the battery bank is divided into a greater number of battery sections? To help answer this question, operating and extraction efficiency curves are plotted in Figure 17 for a battery load voltage of three-quarters full nominal value, i.e., η_{op}', η_{et}' and η_{eb}'. These curves represent the efficiencies of three charging battery sections in a four section bank. (In this case, the efficiency curves subscripted 1 and 2 represent two and four charging sections, respectively.) Note that improved overall system efficiency, where η_{eb}' is greater than both η_{eb1} and η_{eb2}, is only achieved for the wind velocities $0.69 < v_w < 0.91$ with the greatest improvement at $v_w = 0.8$, i.e., an absolute improvement of 5%. This largest efficiency improvement corresponds to a modest increase in stored battery power of approximately 0.037 per unit, i.e.,

$$\left[\frac{\eta_{eb}'(v_w = 0.8)}{\eta_{eb2}(v_w = 0.8)} - 1 \right] \cdot P_{B2}(v_w = 0.8).$$ Also, with one charging battery section in a four section bank, operating efficiency can be maintained at unity for a range of wind velocities below $v_w = 0.5$, i.e., where η_{op1}, the operating efficiency for two charging sections, drops below unity. However, the stored power, P_{B1}, is only

0.085 at $v_w = 0.5$. Thus, even a large improvement in system efficiency below this wind velocity is not expected to considerably improve system power conversion capability. However, a cost-benefit analysis is necessary to determine if improved system efficiency, due to more battery sections, offsets the additional cost in providing these finer increments in battery voltage.

For a windmill with an increased curvature in its C_p characteristic, however, a power system with a larger number of battery sections is more worthwhile. A larger curvature in windmill C_p curve results in greater system inefficiency when system operation is away from the peak of the battery input characteristic. As an example, imagine the P_{g1} curve in Figure 15 as windspeed drops below $v_w = 0.5$. For these wind velocities the locus of desired generator operation, along P_{G1}, and actual generator operation, along $P_{t1}(\phi = \phi_m)$ diverge as wind velocity decreases. Thus increased curvature in P_{g1} would result in decreased power conversion and, thus, lower operating efficiency for every value of wind velocity below $v_w = 0.5$. Yet, if finer increments in battery load voltage were employed in the system, then operating efficiency can be maintained at unity for a larger range of wind velocities, as is shown in Figure 17 with η_{op1} and η_{op}'. Therefore, with more battery sections, the system becomes less sensitive to the inefficiencies incurred due to generator flux saturation, since battery voltage can be more finely switched to return system operation close to unity operating efficiency.

Figures 18 and 19 and Figures 20 and 21 show both P_T and P_B curves as well as system efficiencies simulated for power systems

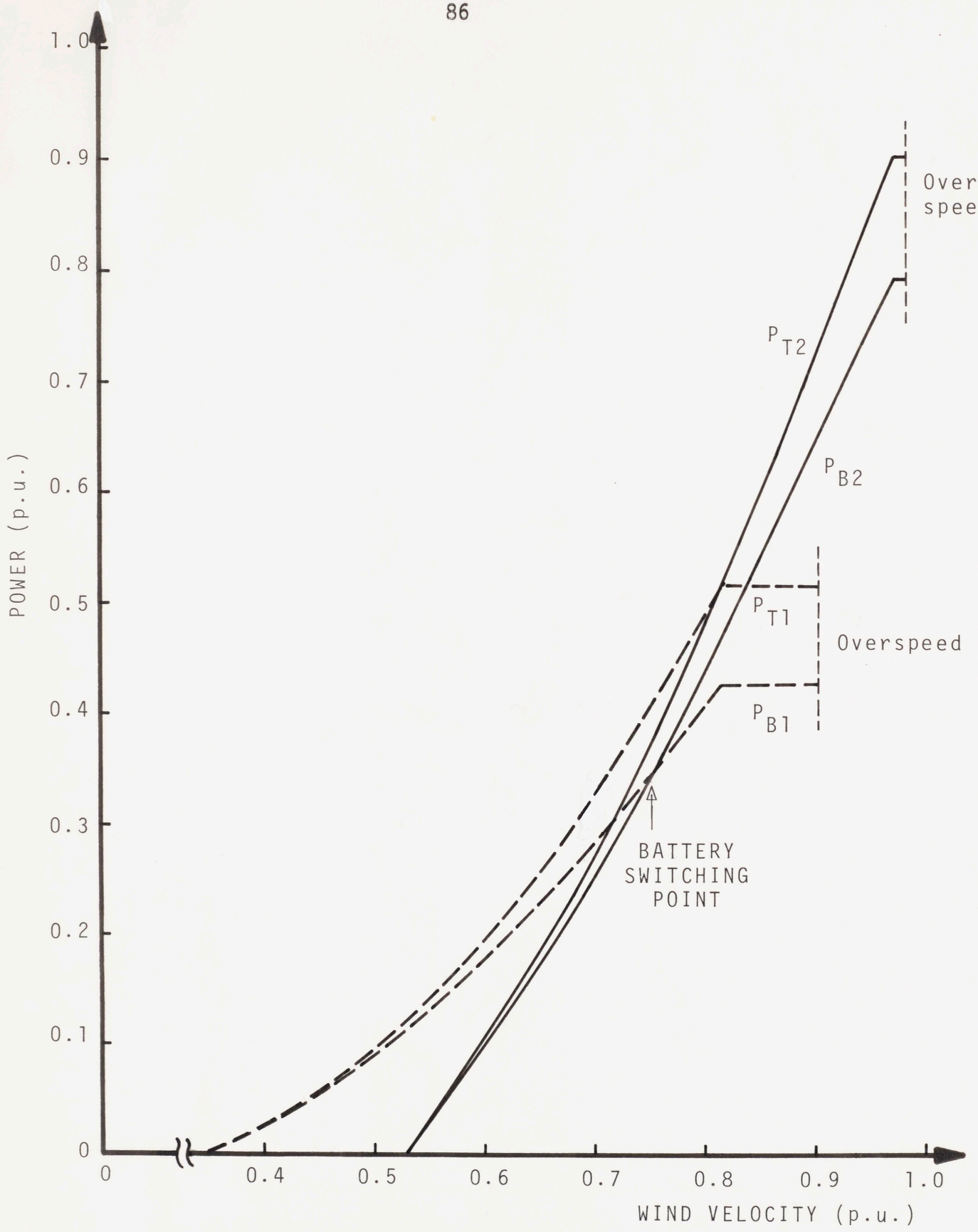

Figure 18 Generator Power and Stored Battery Power as a Function of Wind Speed for a Low State-of Charge Battery Bank.

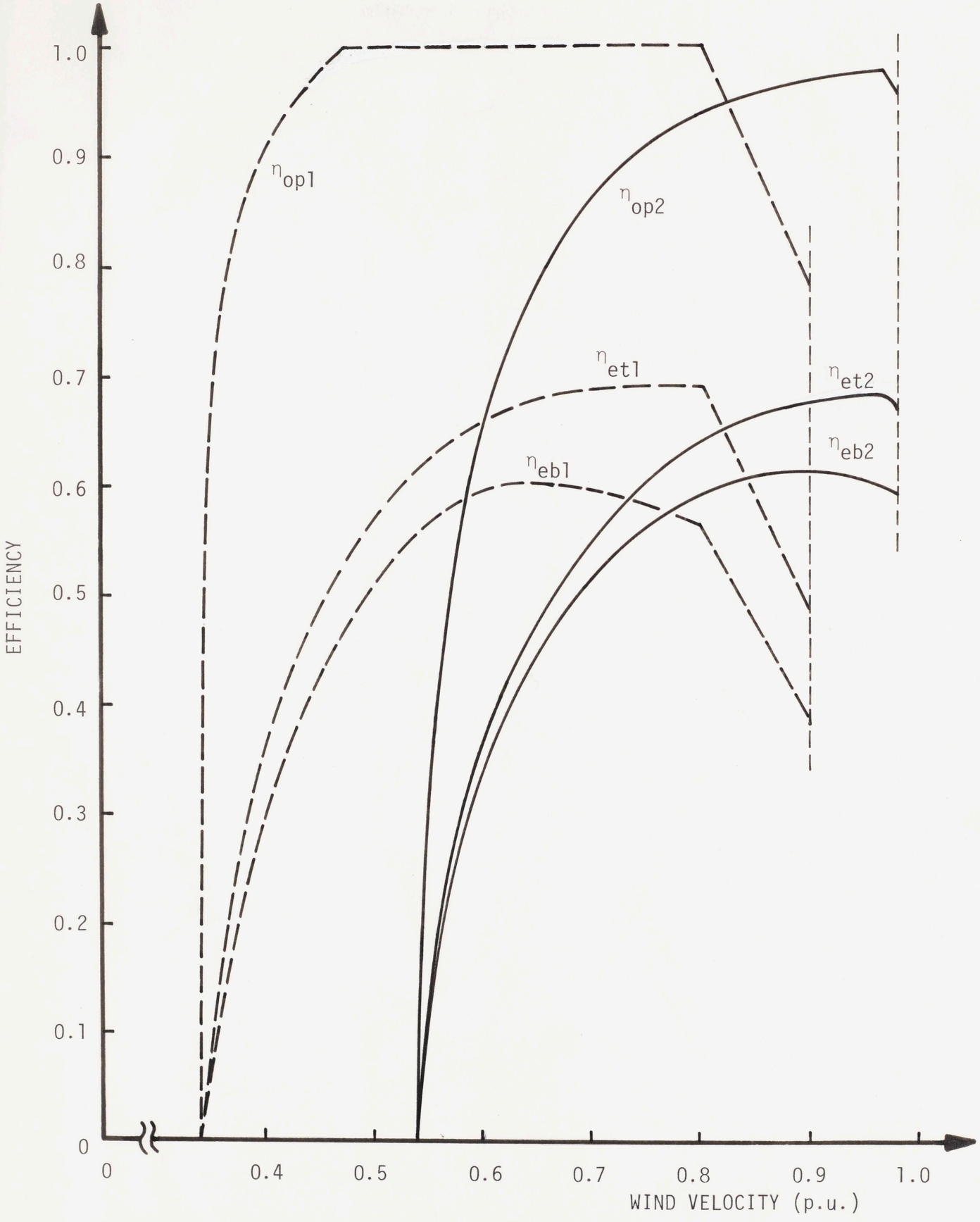

Figure 19 System Operating and Extraction Efficiencies as a Function of Wind Velocity for a Low State-of-Charge Battery Bank

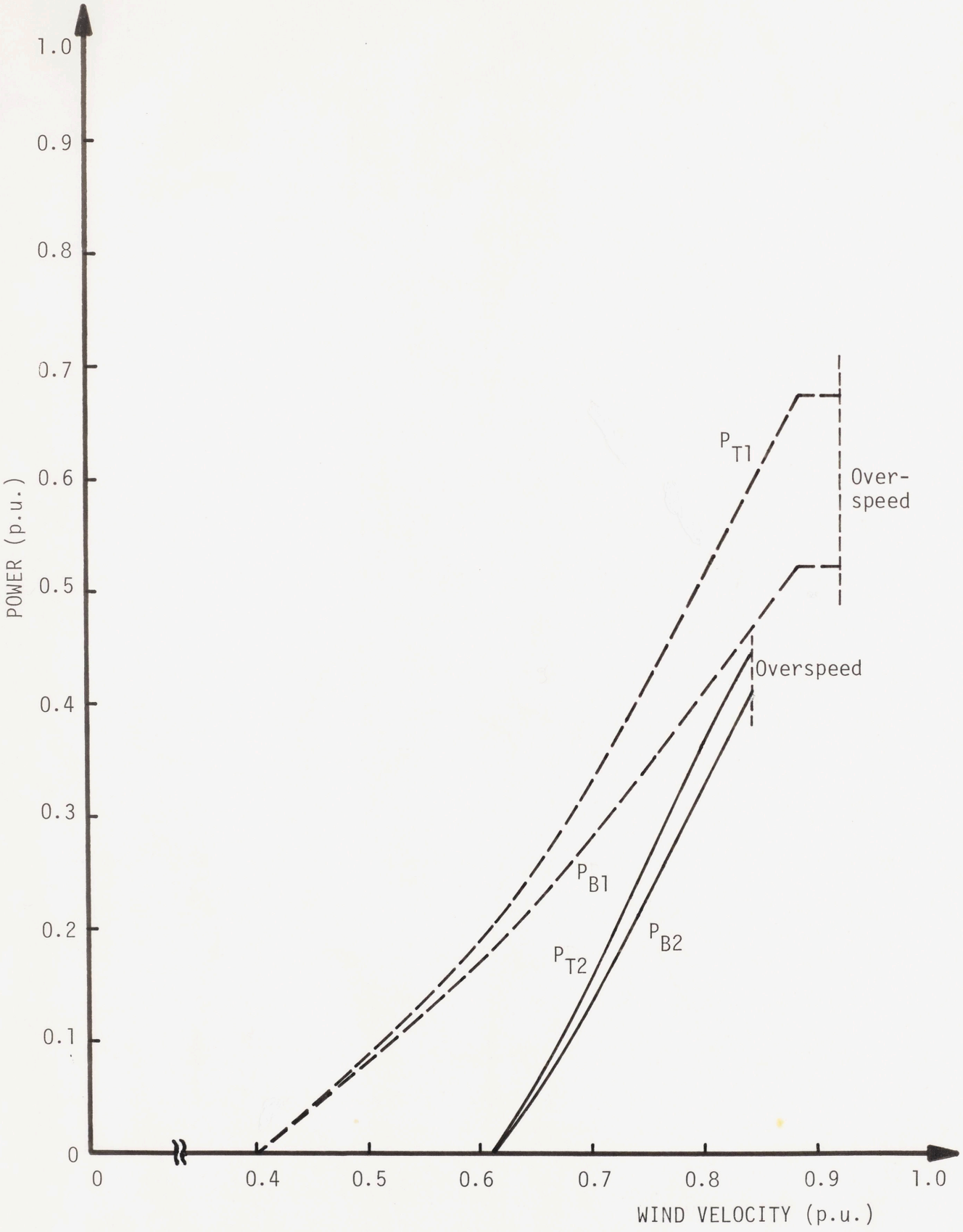

Figure 20 Generator Power Output and Stored Battery Power as a Function of Wind Velocity for a High State-of-Charge Battery Bank

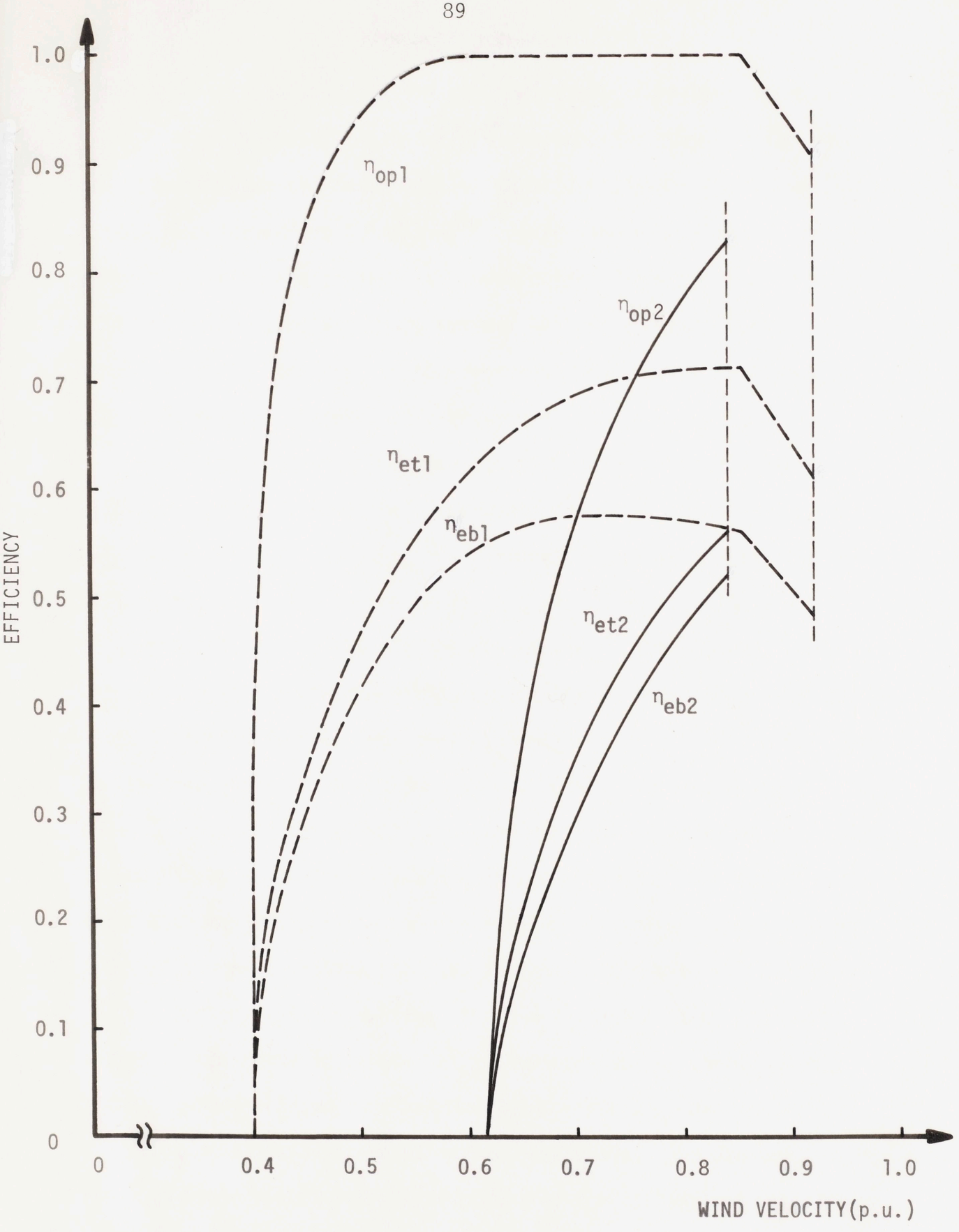

Figure 21 Generator Power Output and Stored Battery Power as a Function of Windspeed for a High State-of-Charge Battery Bank

with their battery banks in low and high state-of-charge, respectively. The values of the battery parameters for these simulations are obtained from the battery banks to be used in the scale model system (see Appendices B and C). These figures are again drawn only up to rated shaftspeed. If these pairs of figures are compared with the system simulation for nominal battery voltage, i.e., Figures 16 and 17, then certain observations about system performance, away from nominal battery state-of-charge, can be made.

First, note that in both low and high state-of-charge cases, system operation without shaft overspeed cannot be maintained up to rated wind velocity, i.e., $v_w = 1$. Second, note that overall system efficiency, i.e., the curves marked η_{eb} in Figures 17, 19, and 21, is, in general, lower for the off-nominal state-of-charge cases. Thus, as expected, system power conversion capability is reduced when battery characteristics deviate from their nominal values. Third, note that in the high state-of-charge case shown, system power conversion is never improved by charging two battery sections insteady of one. This is due to the insufficient loading of the generator when the batteries are fully charged. Lastly, an observation inferrable from the three pairs of system operating characteristics, is the movement of the desired battery switching point as a function of battery state-of-charge. This point is located at that wind velocity where the P_{B1} and P_{B2} curves intersect. Maximum system efficiency away from this operating point is improved by battery switching. For the complete range of battery state-of-charge the battery switching point varies approximately between $0.75 < v_w < .85$, if shaft overspeed is ignored,

increasing with state-of-charge. However, whether the necessity exists to implement a control to alter the point of battery switching, as a function of battery state-of-charge, is unclear. A cost-benefit analysis is again required to weigh the gain in system efficiency achieved by knowing exactly when to switch battery load, against the cost of both measuring battery state-of-charge and implementing the control.

In implementing a control that adjusts system operation as a function of battery state-of-charge, the locus of desired system operation as a function of wind velocity, i.e., ω_{so} (Eq. 41), is also important. This desired operating locus changes with respect to battery state-of-charge. For the computer simulation of the scale-model power system, Figure 22 shows approximate plots of ω_{so} as a function of wind velocity for different battery states-of-charge. The curves are plotted only for those wind velocities where generator constraints do not limit system operating efficiency. Note the minimal variation in $\omega_{so}(v_w)$ for the extremes in battery state-of-charge. Thus implementing a control scheme that varies $\omega_{so}(v_w)$ as battery state-of-charge changes may not be necessary to achieve adequate system efficiency. Yet, a cost-benefit analysis is, again, necessary to evaluate such a control scheme.

Steady-state windmill power system analysis is now complete. A computer simulation has been used to calculate both the regions of system operation and the locus of desired system operation. Efficiencies have been calculated for the different modes of generator operation,

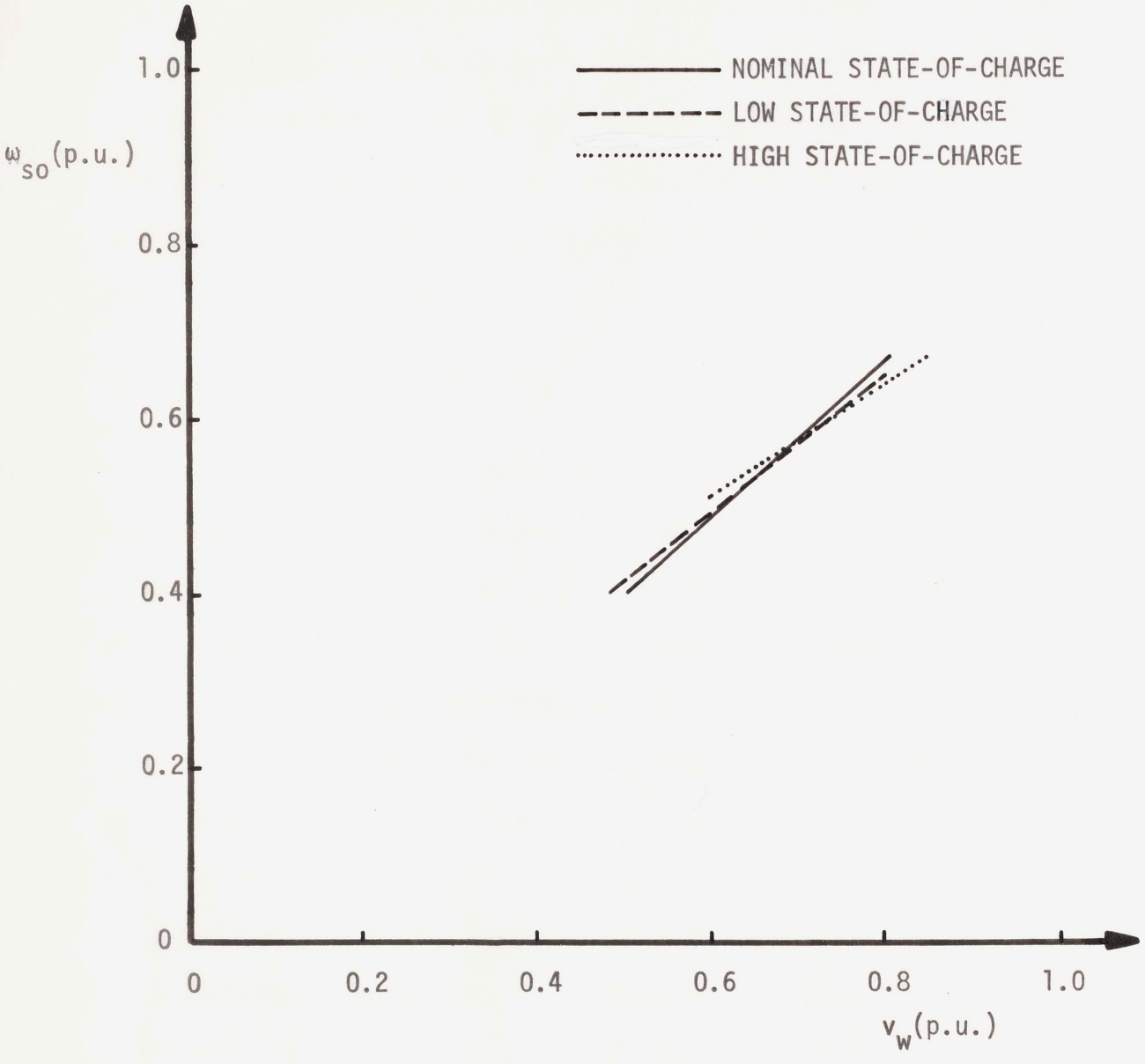

Figure 22 Desired Operating Shaftspeed as a Function of Wind Velocity for Different Battery States-of-Charge

i.e., maximum field current, maximum armature current or unconstrained operation. Also the location of the battery switching point was found.

Concluded from this analysis is that two battery sections seem optimum in obtaining good system power conversion for most wind velocities. Also shown was that varying the system operating locus as a function of battery state-of-charge is not necessary to maintain adequate system efficiency.

III.2 Dynamic System Simulation

This section is devoted to the results of a digital computer simulation of the dynamic behavior of the windmill power system. The dynamic model for the system was introduced in Section II.3, Figure 14. The parameters of the simulation are those of the physical scale model system described in Appendices B through E.

As was discussed in Section II.3, two types of dynamics are associated with the windmill control system. The first is system behavior related to changes in wind velocity alone. The second is dynamics associated with the discrete switching of battery bank voltage. Since both types of dynamics are unique, each will be discussed separately in this section.

III.2.a System Dynamics Associated with Changes in Wind Velocity

The object of the control system discussed here is to allow system operating point to track changes in desired operating point (ω_{so} as a function of wind velocity in Figure 14) with "good" dynamic performance. The method of control available is the choice of field

current time constant, τ_f, which acts as a gain element in the control loop, as shown in Figure 14.

Figure 23 shows the results of the computer simulation for a 0.1 step change in wind velocity from an initial velocity of $v_w = 0.6$ with one battery section charging. The plots shown are system shaftspeed versus time, starting from the initiation of the disturbance, for different value of field current time constant. From the plots the most well behaved dynamics, i.e., the critically damped system, result from $\tau_f = 0.5$ seconds. Shorter time constants produce considerable overshoot and ringing while the longer time constant results in an overdamped response.

The windmill control system is, however, nonlinear in nature. This can be seen from Figure 14 where the gain around the control loop is dependent upon the state of the system. Thus a field current time constant chosen to produce a critically damped response around one system operating point may not result in the same desirable response near a different operating point. Also the dynamics presented in Figure 23 were for the region of system operation where no generator field or armature current constraints are met.

In those regions of system operation where generator flux saturation occurs, the control system is forced to run open-loop. This is because the feedback control, that adjusts field current as a function of the error between actual and desired shaftspeed, can no longer initiate any change in the generator field current. The response of the system to changes in wind velocity is now expected to be first order in nature because only a single differential

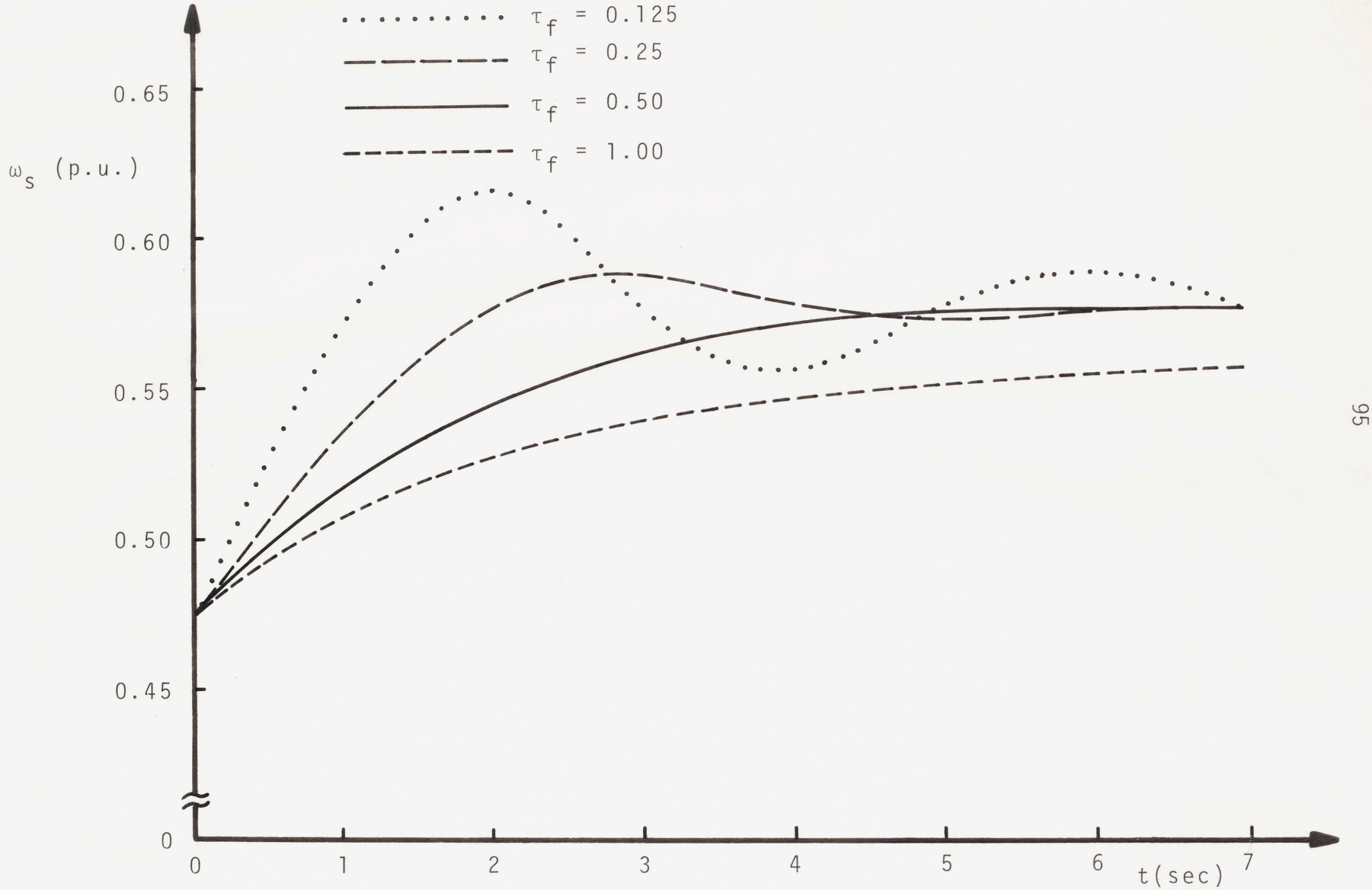

Figure 23 Shaftspeed Dynamics Associated with a 0.1 p.u. Step in Wind Velocity Initiated from a Speed of 0.6 p.u. for Four Values of τ_f

equation governs the dynamics of the rotating shaft, i.e., Eq. 38 with $\phi = \phi_m$, the maximum flux level.

In the case of generator armature current limiting, the feedback control loop is changed, as can be seen from Figure 14. In this case, the relative stability of the system is dependent upon the choice of the time constant, τ_{ac}. No dynamics are assumed to be associated with the switching of control loops, i.e., the switch in Figure 14 can change positions instantaneously.

Figure 24 shows shaftspeed dynamics in the vicinity of several different system operating points for 0.1 per unit step changes in wind velocity. Each response in the figure is marked with the initial equilibrium wind velocity before the disturbance was introduced. Also, all these responses are for a $\tau_f = 0.5$ seconds, i.e., the field current time constant that produced the best response in Figure 23. Notice the difference in damping between the two responses $v_{wo} = 0.6$ and $v_{wo} = 0.7$. These two responses occur in the unconstrained region of system operation, i.e., no generator field or armature current limiting. The difference in responses, however, does not seem severe enough to warrent alteration of field current time constant as a function of system operating point. The well damped nature of the response for $v_{wo} = 0.85$ is typical in that region of system operation where generator flux saturation occurs. This particular plot is for two charging battery section and, as was shown in Section III.1, maximum generator flux always exists in this region of operation. As predicted, this response is first order in nature. The response for $v_{wo} = 0.75$ occurred in that operating region where

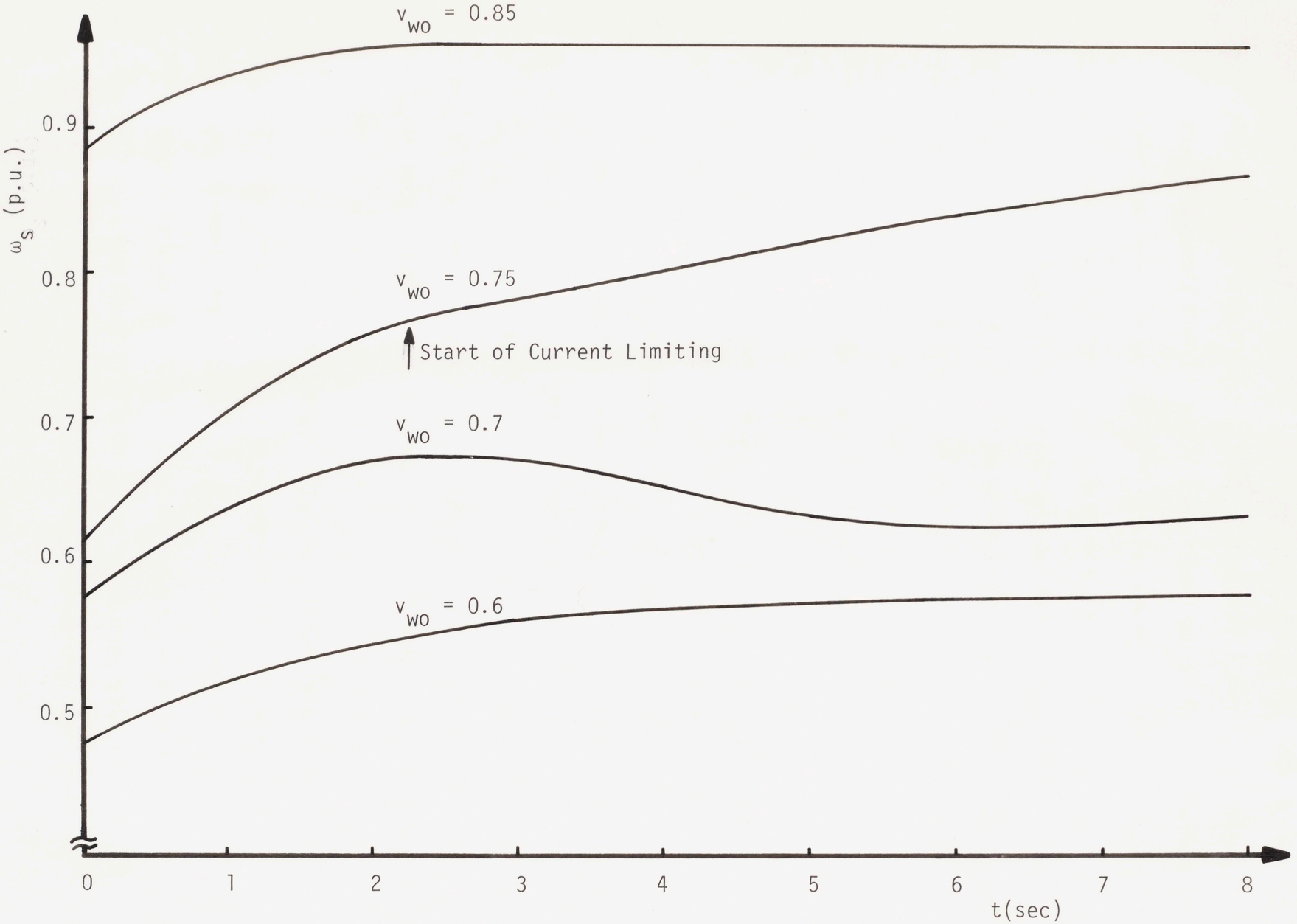

Figure 24 Shaftspeed Dynamics for a 0.1 p.u. Step in Wind Velocity with τ_f=0.5. Initial Wind Speed is Indicated on the Curves

generator armature current limiting results. For this situation, only one battery section is charging. Also, the choice of time constant, τ_{ac}, was 0.1 seconds for the simulation. Under equilibrium conditions, generator armature current limiting for one charging section occurs for wind velocities above 0.81 per unit (see Figure 15 and related text). For the dynamic condition discussed here, i.e., a step in wind velocity, a delay in armature current limiting results after the wind-speed goes above 0.81 per unit, at t = 0. Also, in the plot marked $v_{wo} = 0.75$ in Figure 25, note the slow rise in shaftspeed as the current limiting takes place until a final equilibrium is reached (not shown in the plot).

The final topic of interest, concerned with system behavior related to changes in wind velocity, is the variation in system response as a function of the curvature of the windmill C_p characteristic. The curvature of C_p is here defined as the rate with which the value of C_p decreases with respect to the per-unit velocity ratio, i.e., ω_s/v_w, as this velocity ratio is altered away from its peak power-ratio value, i.e., $\omega_s/v_w = 1$. As an example, if the curvature of C_p is doubled, then the distance $(1 - C_p(\frac{v_w}{\omega_s}))$ in Figure 1 is also doubled for all values of v_w/ω_s.

Figure 25 shows the simulated results of system shaftspeed for a 0.1 per unit step in wind velocity initiated from $v_w = 0.7$. The field current time constant, τ_f, is 1 second in all cases. The three responses shown have been simulated using the original parabolic C_p curve shown in Figure 1 and C_p curves with twice and three times the original curvature. Equilibrium shaftspeeds differ

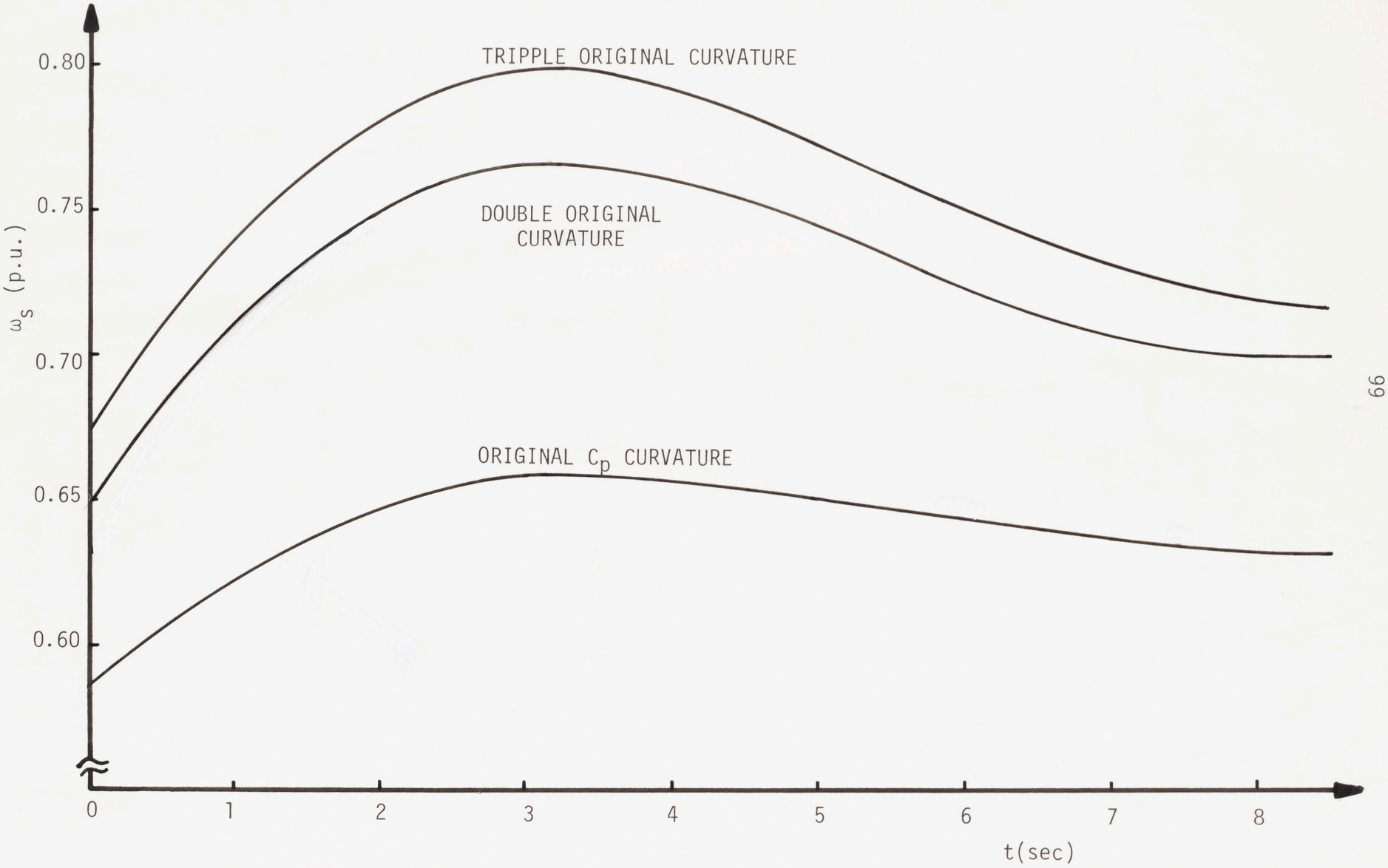

Figure 25 Shaftspeed Dynamics for a 0.1 Step in Wind Speed for Three Different Curvatures of the C_p Characteristic. Initial Windspeed is 0.7 p.u. For these simulations, τ_f= 1 sec.

in all cases because of the different locations of the peaks of the battery "input" characteristics for each C_p curve.

Note the increase in peak overshoot and ringing of the responses in Figure 25 as C_p curvature is increased. Therefore proper choice of τ_f for a particular windmill system requires knowledge of the type of windmill employed in the system.

III.2.b System Dynamics Associated with Battery Load Switching

For this discussion, the assumption is made that the batteries are always at their nominal state-of-charge.

The decision on when to switch battery bank voltage was discussed in both Sections II.2 and III.1. How this decision is made in both the computer and scale model systems will be further discussed in this section. However, as seen from the generator output characteristics, Figure 6, a change in battery load voltage produces an instantaneous change in generator load characteristics. To return generator operation as close as possible to the desired operating point, a change in generator field excitation is necessary. Different system behavior results depending on how rapidly field current is changed, as determined by the field current time constant. Before battery switching dynamics are presented, the battery switching criteria will be further discussed.

(i) Battery Switching Decision

In the proposed windmill power system, the decision to add or remove battery sections in the charging circuit is an important one. The switching criteria must be chosen such that hysteresis is

exhibited with respect to wind velocity. This hysteresis is necessary to prevent an oscillating switching condition near a critical wind speed.

From Figure 16, for a wind speed increasing from zero, the desired point of battery switching is at $v_w = 0.82$. However, under dynamic conditions, it is desirable to filter out high frequency variations in measured wind velocity such that switching occurs only when wind velocity exceeds 0.82 per unit, when averaged over some time period. In this way, premature switching due to rapid variations in wind velocity is prevented.

An alternative method to wind velocity filtering is also available. This method relies, in part, on the occurrence of generator armature current limiting prior to reaching the desired point of battery voltage incrementation. As seen from the control model in Figure 14, when rated armature current is reached, reduction in generator loading is achieved by decreasing field current. As wind velocity increases, the field current eventually reaches a value i_{fs}, where i_{fs} is the steady-state field current when the system is operating at the desired battery switching point with one charging battery section. For the computer model simulation i_{fs} is 1.0 per unit. Once field current becomes less than i_{fs} then average wind velocity is known to be above 0.82 per unit.

*"High frequency" refers to those variations that occur faster than the response time of the system.

For both the computer and scale model simulations, the actual algorithm employed for battery voltage incrementation relies on the above discussed states of both the armature and field currents. Battery voltage incrementation is initiated when both generator armature current reaches its rating and field current falls below i_{fs}. The reason for measuring armature current as well as field current is to prevent any ambiguity in the location of system operation, i.e., field current may drop below i_{fs} during other transients associated with wind velocity changes.

To demonstrate this algorithm's filtering effect on rapid changes in wind velocity, the power system has been simulated with the digital model for a sinusoidal wind velocity with frequency 0.15 sec^{-1} and with amplitude 0.05 per unit centered around $v_w = 0.81$. Figure 26 shows the resulting behavior of both actual and desired shaft-speeds,* and both field and armature currents. For $t < 0$ the system is in equilibrium.

Two modes of control system operation are present in Figure 26. These modes are reflected in the behavior of the field current, i_f in Figure 26(b), for different state of the battery charging current, I_B in Figure 26(a).

When the charging current is below rating, the field current is driven by the difference between actual and desired shaftspeed.

*For this case of fixed battery bank parameters, desired shaftspeed is directly proportional to wind velocity.

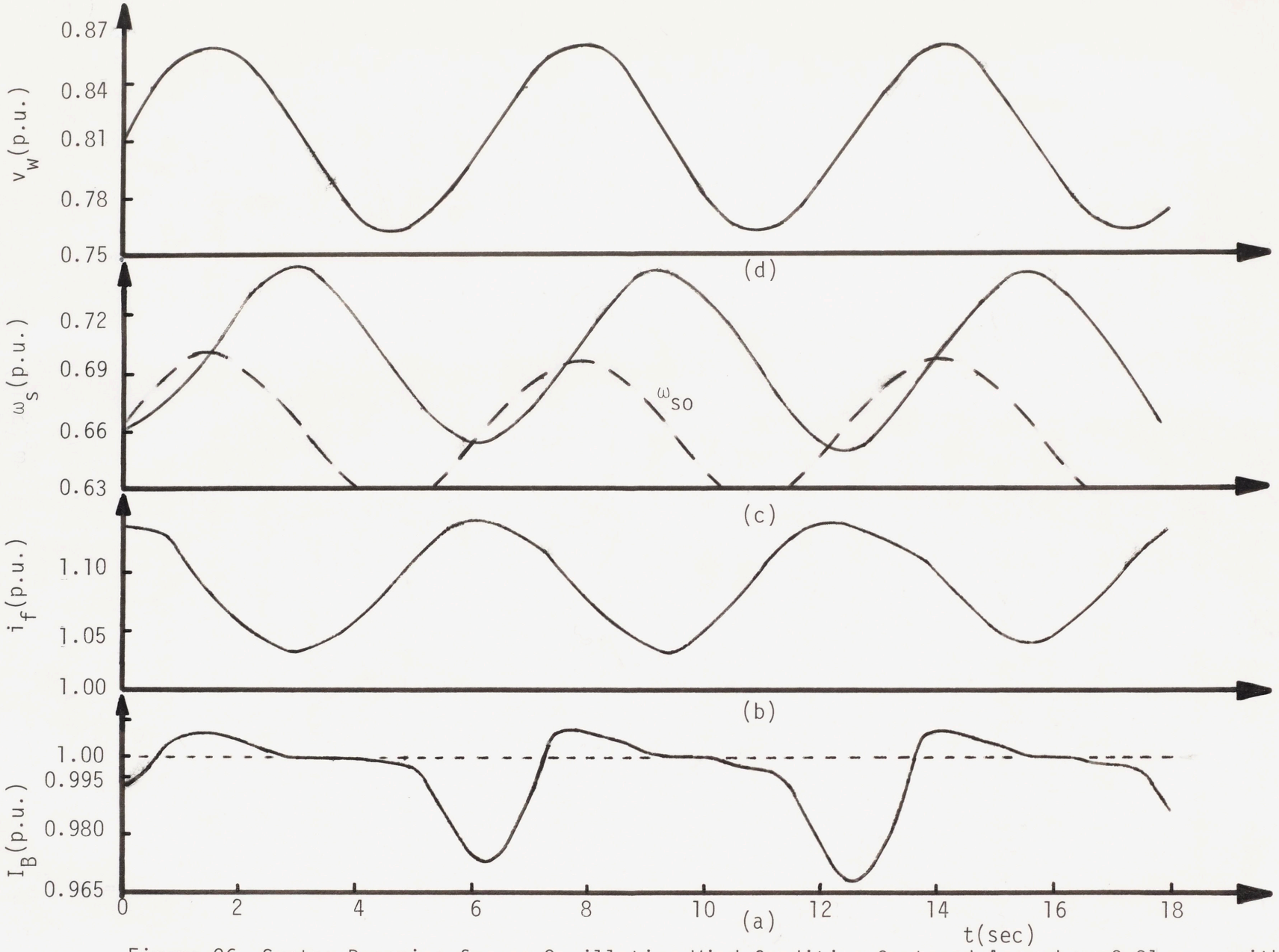

Figure 26 System Dynamics for an Oscillating Wind Condition Centered Around v_W=0.81 p.u. with Amplitude 0.05 p.u. and Frequency 0.15/sec. For this simulation, τ_f = 1 sec.

The implemented control law is given by Eq. 40 with $\tau_f = 1$ for this simulation. The objective of this control is allowed actual system shaftspeed to track changes in desired shaftspeed such that maximum power is transferred to the batteries.

However, for charging current above rating, the field current is decreased in proportion to the difference between actual and rated charging current. The control law for this case is given by Eq. 42 with $\tau_{ac} = 0.1$ for this simulation. The objective now is to decrease generator loading such that the charging current does not exceed rated generator current. When armature current limiting takes place, where $I_B > 1$ in Figure 26(a), tracking of desired shaftspeed is no longer possible. The result is an increasing deviation between actual and desired shaftspeeds for as long as rated armature current is exceeded, as seen in Figure 26(c).

However, the main purpose of Figure 26 is to show that for the oscillating wind velocity simulated, the system maintains operation with one charging battery section; battery switching does not occur when the wind velocity exceeds 0.82 per unit. This is because the field current does not go below the value i_{fs}, i.e., 1.0 per unit for this system, which is the resulting steady-state value of the field current when $v_w = 0.82$. Yet, if the computer model is simulated for a 0.02 per unit step change in wind velocity initiated from $v_w = 0.81$, then approximately 10 seconds after the initiation of the step the generator field current drops below 1.0 per unit in the presence of armature current limiting. With the implementation of the battery switching alborithm, the result is the incrementation of

the battery voltage. (This response is not shown yet a similar response will be shown in Section II.2.b(ii).)

From the above discussion, therefore, battery voltage incrementaiton via an algorithm that looks at generator currents instead of wind velocity helps to prevent premature battery switching that may be caused by rapid variations in wind velocity.

For battery voltage decrementation, a similar algorithm can be developed such that high-frequency rejection is again attained for wind velocities decreasing from rated value. However, battery voltage decrementation should only be initiated when the average wind velocity falls somewhat below the battery switching point, i.e., $v_w = 0.82$ in Figure 16. In this way, hysteresis is added to the switching cycle such that oscillation between battery increment and decrement states is prevented in the case of an average wind velocity that remains at 0.82 per unit.

For the computer and physical scale model simulations, the actual algorithm used for battery voltage decrementation involves measuring both generator field current and shaftspeed. Battery decrementation is initiated when both field current is at its maximum value, i_{fm}, and shaftspeed falls below the value ω_{ss}, where ω_{ss} is the steady-state shaftspeed when the system is operating at $v_w = 0.80$ (i.e., slightly less than the switching point wind velocity) with two charging battery sections. For the present system, ω_{ss} is approximately 0.82 per unit. Using this algorithm, which looks at both generator field current and shaftspeed, again prevents any ambiguity in the location of system operation.

In summary, the battery voltage increment and decrement algorithms are:

- Battery voltage increment: $I_B = 1$ and $i_f < i_{fs}$

- Battery voltage decrement: $i_f = i_{fm}$ and $\omega_s < \omega_{ss}$

where i_{fs} is the steady-state field current when $v_w = 0.82$ with one charging battery section in the system and ω_{ss} is the steady-state shaftspeed when $v_w = 0.80$ with two sections charging.

Now that battery voltage increment and decrement algorithms have been developed, the actual dynamics associated with battery switching are presented.

(ii) Battery Switching Dynamics

As mentioned in the introduction to this subsection, (III.2.b), different system behavior results depending on how rapidly field current changes after the initiation of battery switching. Figure 27 shows the dynamics associated with battery incrementation. The conditions for switching came about as the result of a 0.1 step change in wind velocity from an initial wind speed of 0.8 per unit. The only difference between Figures 27(a) and 27(b) is the value of field current time constant used in the simulation after the occurrence of switching. Prior to switching, the field current time constant in both cases had the value of 1 second, which was shown in Section III.2.a to be near optimum for variations in wind velocity around $v_w = 0.7$. Notice the large overshoot in shaftspeed in Figure 27(a) when the time constant remains at $\tau_f = 1$ after switching.

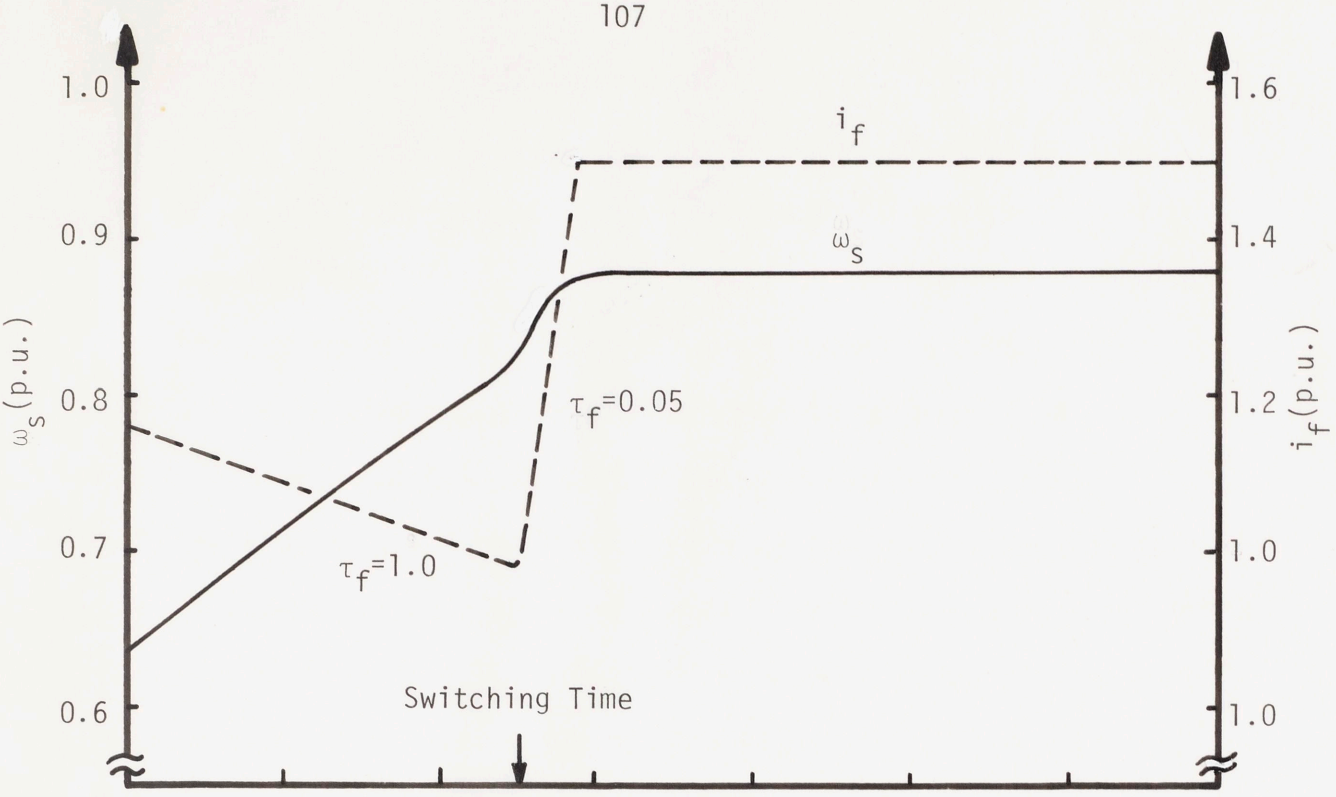

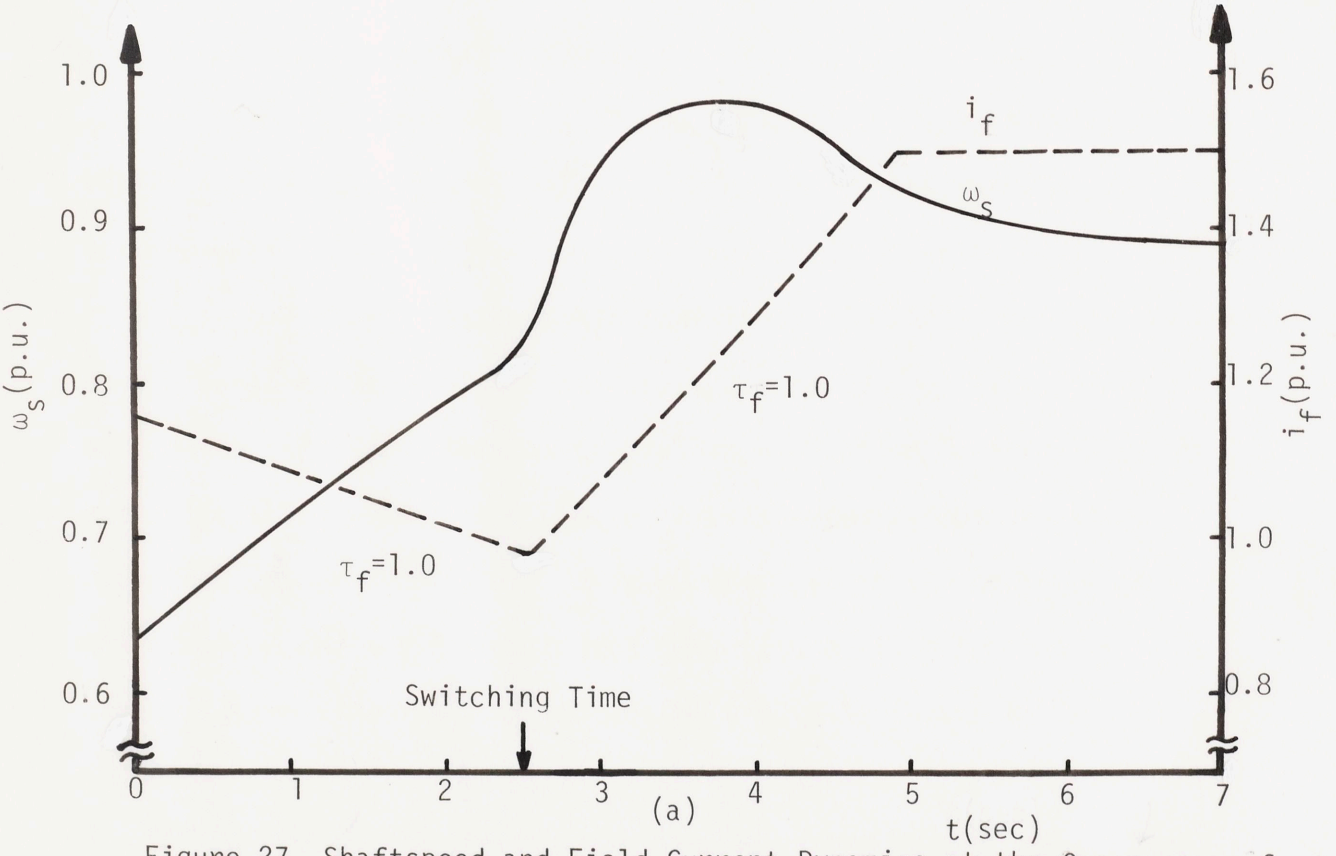

Figure 27 Shaftspeed and Field Current Dynamics at the Occurrence of Battery Voltage Incrementation. Dynamics for Two Values of τ_f are Shown where Switching is Initiated by a Step in Wind.

However, for the smaller time constant initiated after switching, τ_f = 0.05 second in Figure 27(b), no overshoot in generator shaft-speed results.

Figure 28 shows similar dynamics occurring after battery switching for a wind speed increasing linearly to 1 per unit from an equilibrium value of 0.8 per unit. The wind speed ramp starts at t = 0 and ends at t = 4 seconds. Notice again the overshoot in shaft-speed, exceeding rated shaftspeed by 10%, for the case of τ_f = 1 second. Also note the much improved behavior in the case of the shorter time constant initiated after switching. In Figure 28(a), the small difference in the rate of change of field current after t = 2 seconds is due to the occurrence of armature current limiting. Also the change of slope of the same field current at t = 5.3 seconds is again due to armature current limiting.

Lastly, presented in Figure 29 is the system response to a linearly decreasing wind velocity resulting in the decrementation of battery voltage. In this simulation, the field current remains at τ_f = 1 second during the complete transient. Immediately after switching, a large spike in armature current occurs due to the now larger difference in voltage between generators and battery terminals. The rate with which this current spike returns below rated current is dependent on how rapidly the field current can be reduced through the armature current feedback loop (see Figure 14). For this simulation τ_{ac}, the time constant associated with this feedback, is 0.1 seconds. After the armature current is reduced to 1 per unit, at t = 5.7 seconds in Figure 29, the control system returns to its

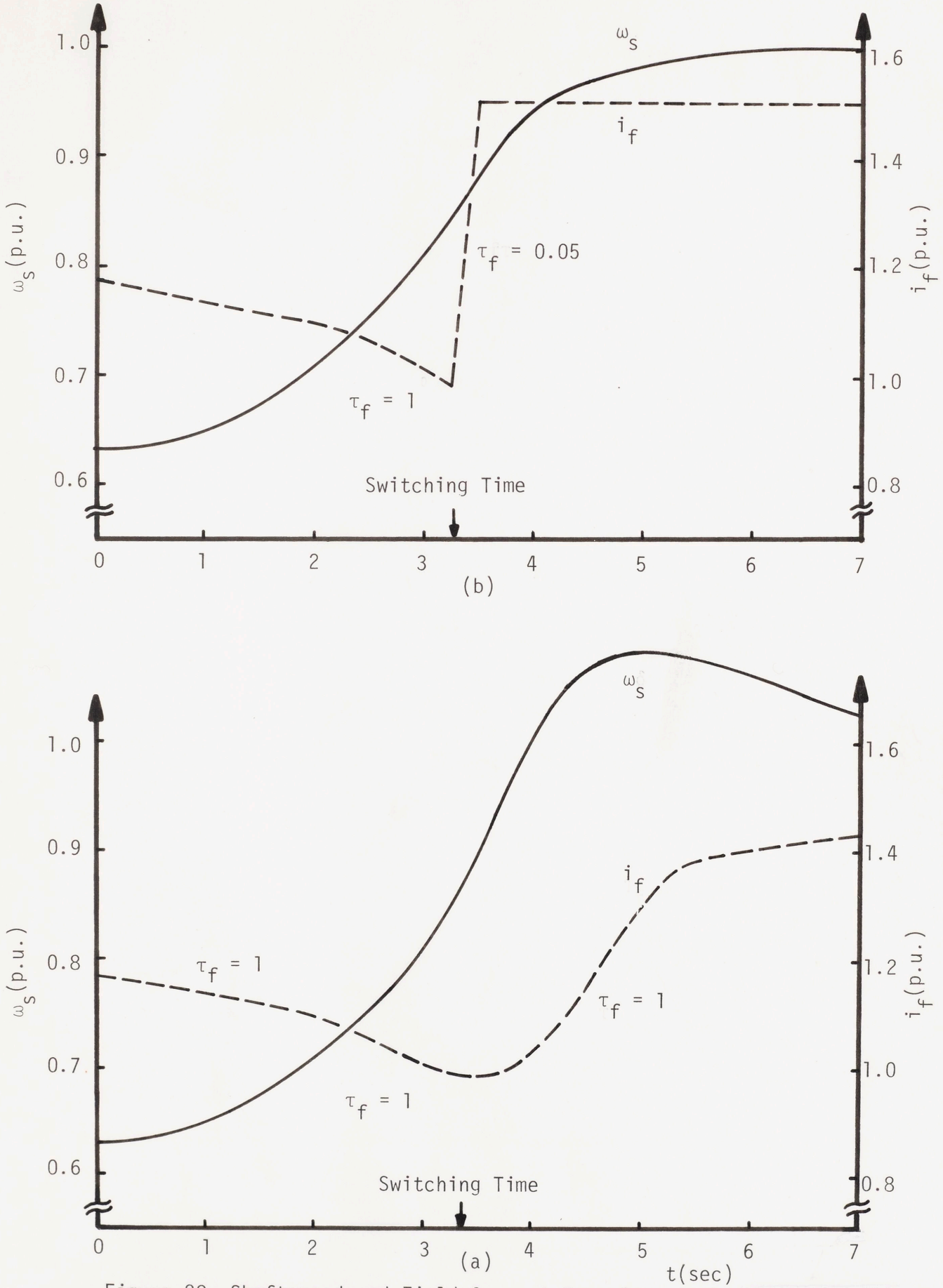

Figure 28 Shaftspeed and Field Current Dynamics at the Occurrence of Battery Voltage Incrementation. Dynamics are for Two Values of τ_f where Switching is Initiated by a Ramp in Wind

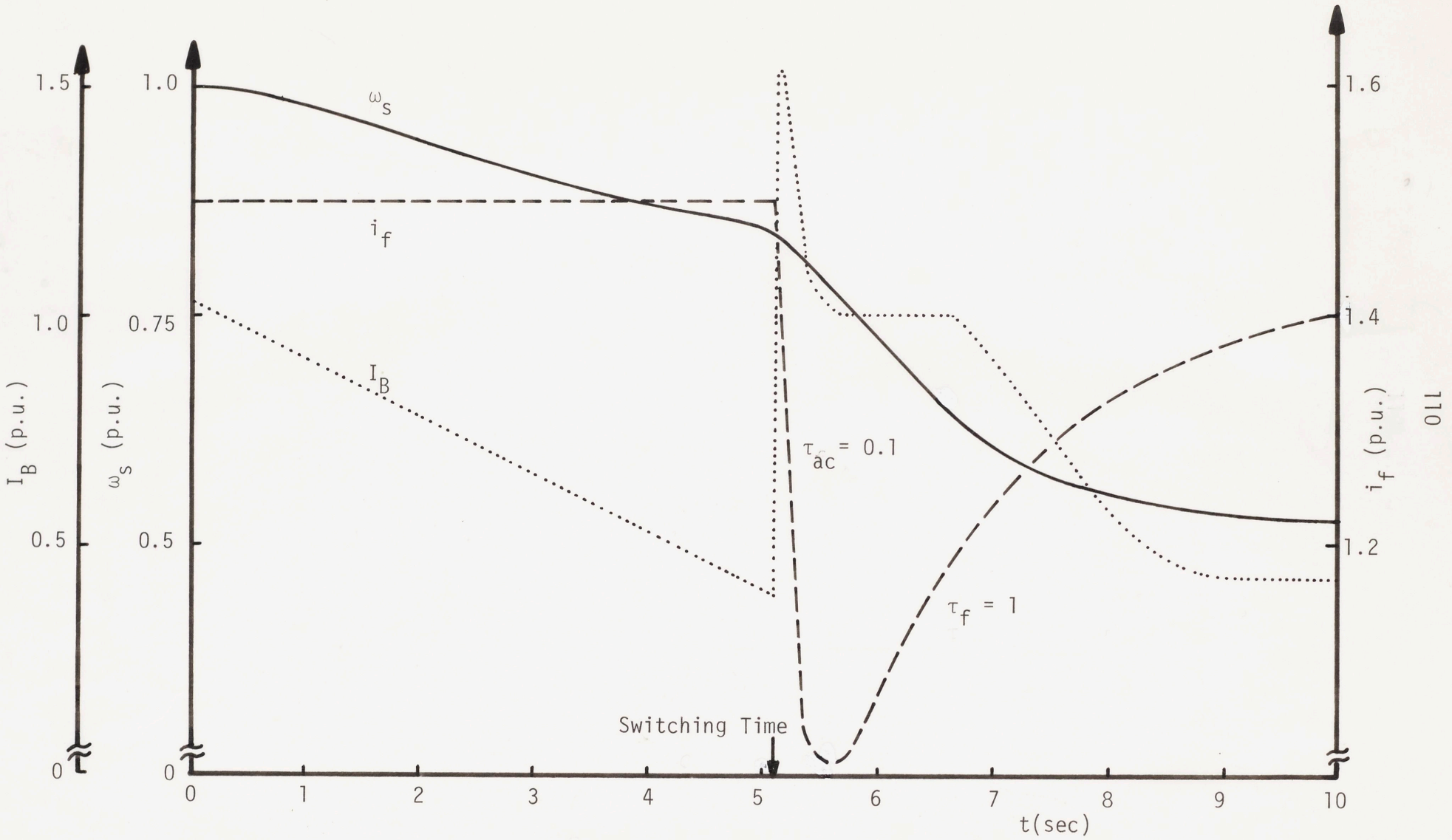

Figure 29 System Dynamics at the Occurrence of Battery Voltage Decrementation. Battery Switching is Initiated by a Decreasing Wind Velocity

original behavior of controlling field current as a function of the difference between actual and desired shaftspeed.

III.2.c Summary and Conclusion of Dynamic Investigation

The results of the dynamic investigation described in this section are that the field current time constant can be chosen to optimize mechanical transients due to changes in both wind velocity and battery voltage switching. A choice of τ_f = 1 sec. seems optimum for dynamics associated with wind speed changes in the unconstrained region of system operation. Also the curvature of the C_p curve seems to play only a minor role in affecting system dynamics in this same unconstrained generator operating region.

In the case of field current limiting, system behavior is first order in nature and in the case of armature current limiting, a well behaved response resulted from a choice of τ_{ac}, that time constant associated with armature current limiting, equal to 0.1 seconds.

Developed in this section was a formal algorithm for battery switching. The algorithm provides a filtering effect on wind velocity such that high frequency variations in this wind speed does not lead to premature battery switching. This algorithm also provided hysteresis in the switching cycle to prevent oscillation near a critical wind speed.

The results of system dynamics associated with battery switching showed that a much smaller field time constant was necessary after battery incrementation to prevent shaftspeed overshoot. Also, for transients associated with battery voltage

decrementation, system behavior depends on the choice of τ_{ac}. In this case, smaller values of τ_{ac} result in reduced armature current spikes immediately after battery decrementation.

A final observation on battery voltage switching is also worth mentioning. Note that during the dynamic behavior immediately following battery incrementation or decrementation, shown in Figures 27(b) and 29, conditions exist that are again very close to initiating battery switching according to the developed algorithms. The result may be oscillation between battery load states. To prevent the possible occurrence of this oscillation, the implementation of the battery switching algorithm may have to be inhibited for a short period of time, i.e., a few seconds, after switching has occurred.

The computer program used to perform the dynamic simulations presented in this section is shown and discussed in Appendix F.

CHAPTER IV

WINDMILL POWER SYSTEM CONTROL IMPLEMENTATION

The purpose of this chapter is to present the control system implemented for the physical scale model simulation of the windmill power system. A 2KW single-phase synchronous alternator is used as the electromechanical converter in the simulation. A single-phase generator is employed instead of the more desirable polyphase generator due to the unavailability of a polyphase machine at this low power level. The characteristics of this single-phase generator are described in Appendix B.

Due to the difficulty of bringing a windmill into a laboratory environment, a dc motor has been employed to reproduce the power-speed characteristics of a windmill. The analysis and implementation of this windmill simulator is well documented in Appendix C of Reference 1. For convenience, however, this analysis is briefly redescribed in Appendix D. Since the characteristics of the dc machine as a windmill simulator are also important, these characteristics have also been presented in Appendix D.

This chapter is divided into two sections. The first section involves the circuit implementation of the system control algorithms developed in the previous chapter. The second section presents a few test results of the performance of the control circuitry. The overall behavior, both steady-state and dynamic, of the scale model power system is left for Chapter V.

IV.1 Control System Circuit Implementation

Two types of controls have been developed for the proper operation of the proposed windmill power system. The first type of control involves the analog implementation of the field current control laws developed in Section II.3. The second type of control involves the implementation of battery section rotation and the battery voltage switching algorithms developed in Section III.2.b.

The analog control consists of three modes of generator field current control. The first mode involves maintaining system shaft-speed operation on a desired locus. The second mode maintains battery charging current below a rated value. Equations 40 and 42 show these two controls in their analytical forms. The third mode of field current control involves a simple field current limiting. This control, along with the other two, is shown in Figure 14, i.e., the schematic diagram of the overall analog control system.

As was shown in Figure 3 of Chapter I, SCR's are used as switches to implement both the rotation and voltage switching of the battery section. Commutation of these battery SCR's is achieved by removing the battery charging current through the "turning off" of the SCR's in the bridge rectifier. However, a small amount of time is necessary to allow the charging current to decay to zero through the smoothing choke in the charging circuit.

The choice of smoothing choke is important to circuit operation. A choke with too small an inductance yields a charging current with a large ripple factor. However, a choke with a larger inductance causes

the charging current to decay more slowly through an added free wheeling diode (not shown in Figure 3) when the bridge SCR's are "turned off". Since the power output of the generator is reduced to zero when the bridge is "turned off", a prolonged time in this state of operation produces increased shaftspeed dynamics that may be detrimental.

The calculation of the smoothing choke inductance used in the physical model simulation is shown in Appendix G. The remainder of this section deals with the circuit implementation of the control system.

IV.1.a Analog-Control Implementation

Figure 30 shows the circuit implementation of the three modes of field current control. The "shaftspeed controller" integrates the difference between actual and desired (set point) shaftspeed. This controller produces a signal which drives a current source amplifier that supplies current to the generator field winding. Shaftspeed is measured through the rectification and filtering of the output of a tachometer coupled to the generator shaft. For this implementation, the calculation of set point shaftspeed, shown as $w_{so}(\omega_w,M,soc)$ in Figure 14 and Eq. 41, has been extremely simplified. Figure 22 shows this desired operating shaftspeed related to wind velocity and battery state-of-charge, as calculated by the steady-state computer model. This figure shows that ω_{so} does not vary much with battery state-of-charge. Therefore, the set point shaftspeed has been approximated by the line $\omega_{so} = 0.82v_w$ which closely fits the curves in Figure 22. A simple linear amplifier is used to create

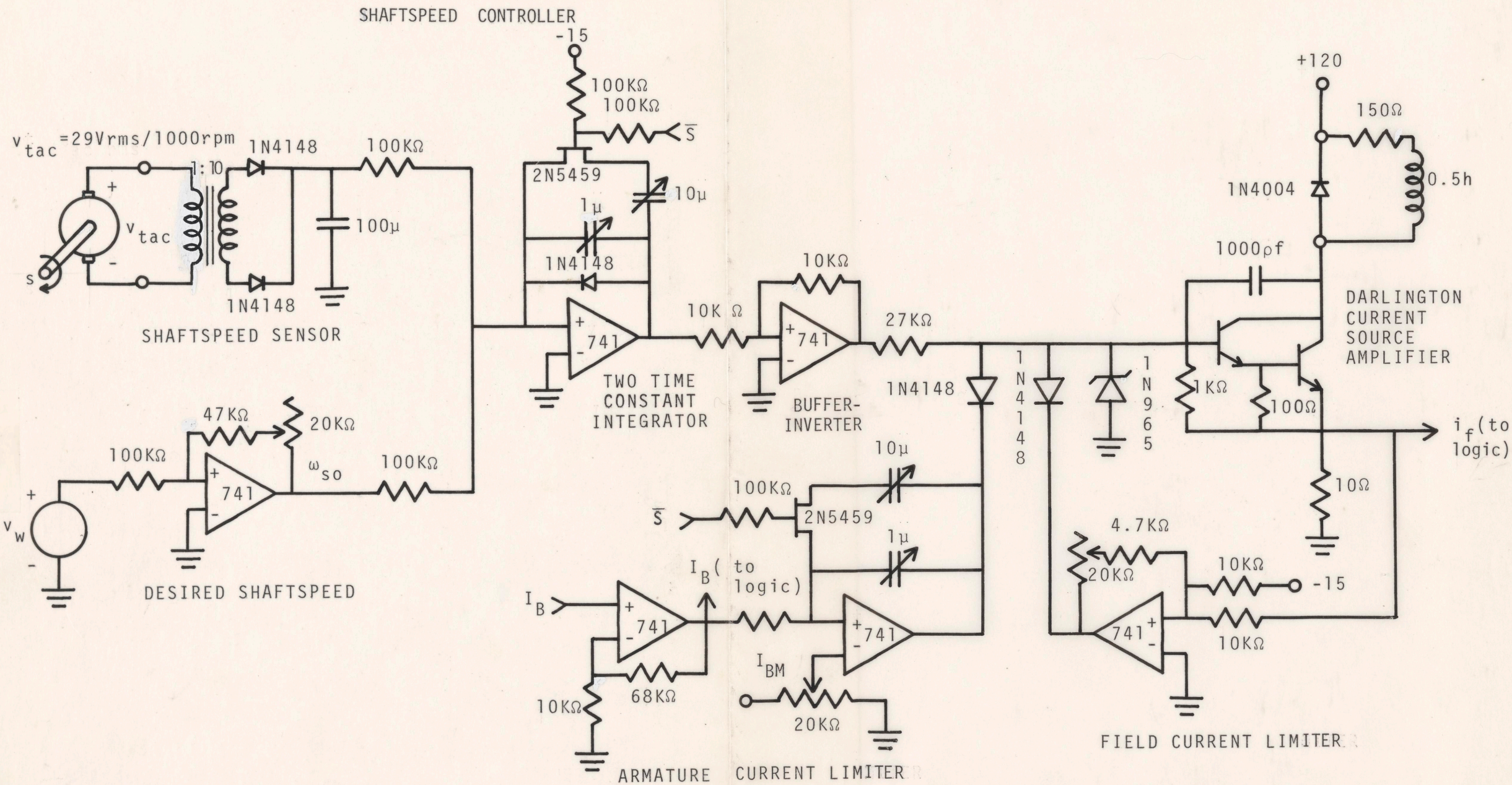

Figure 30 Implemented Analog Control Circuitry

the signal ω_{so} in the implemented control circuit of Figure 30. The input signal to this amplifier is produced by a voltage source that varies from 0 to 15 volts as the wind velocity signal in the windmill simulator varies from zero to rated wind speed.

Two different, yet adjustable, time constants are implemented in the integrator in the shaftspeed controller. A Field Effect Transistor (FET) is used to switch between the two time constants depending on the state of the logic level $\bar{S}$. The diode in the integrator simply prevents the integrator output from going positive.

Normally, the logic level $\bar{S}$ is high such that the FET is conducting and a large integrator time constant, up to 1.1 sec, is implemented. However, when $\bar{S}$ is low, the FET becomes "pinched off" resulting in the implementation of a much smaller integrator time constant. Physically, these two time constants correspond to the two field current time constants that were shown to be necessary from the dynamic system analysis of Section III.2.

A buffer amplifier is used at the output of the shaftspeed controller to prevent loading of the integrator and to produce a signal inversion.

Under unconstrained generator operation, i.e., no generator field or armature current limiting, the diodes at the output of the shaftspeed controller are reverse biased and thus do not provide a signal path. In this mode of operation, the output of the shaftspeed controller provides the drive for the Darlington current source amplifier which, in turn, drives the generator field current. The Darlington amplifier is connected as an emitter follower which

directly relates the amplifier's output current to input voltage. The nonlinearity due to the transistor base-emitter voltage drops is not detrimental to the functioning of the circuit due to the nature of the system feedback. The integrator in the shaftspeed feedback loop drives the generator field current to whatever value is necessary to equate actual and set point shaftspeed.

In terms of amplifier implementation, the base-emitter resistors in the Darlington connection are used to support transistor leakage currents. The base-collector capacitor is used to reduce high frequency incremental gain in the amplifier, thus maintaining amplifier stability. The zener diode at the input of the amplifier as well as the diode connected in parallel with the generator field winding are used for protection purposes. The purpose of the 27KΩ resistor at the output of the shaftspeed controller will be discussed later.

The operation of the field current limiter is simple. The output voltage of the Darlington emitter-follower is fed directly to the input of the field current limiter. When this voltage reaches a certain value, i.e., that value signifying maximum current in the generator field winding, then the voltage at the output of the field current limiter is at that value to just forward bias the diode connected between the limiter's output and the base of the Darlington amplifier. Any further increase in current through the Darlington amplifier results in the removal of base drive to the amplifier through this diode. This removal of base drive causes a lowering of generator field current until the diode "turns off", i.e., when maximum field current is no longer exceeded.

The armature current limiter in Figure 30 involves the implementation of Eq. 41 (Section II.3) whenever maximum armature current is exceeded. The operation of this circuit is similar to the operation of the field current limiter in that a diode is "turned on" to remove base drive from the Darlington amplifier when maximum armature current is exceeded. However, a rate of response is also associated with the armature current limiter. This rate of response is set by the integrator time constant in the armature current limiter circuit. This time constant simulates τ_{ac} in Eq. 41. The input to the limiter is the battery charging current, I_B, which is measured through a small current sensing resistor in the battery charging circuit. This signal is amplified by a factor of 8 through an operational amplifier, shown in Figure 30. The resulting signal is compared to a reference, I_{BM} in Figure 30, corresponding to the value of the signal when the armature current is at rated value. The difference between the input signal and I_{BM} is then integrated. If I_B is less than rating then the integrator output voltage ramps up to positive supply voltage thus maintaining reverse bias on the diode at the integrator's output. However, when I_B exceeds rating, the input to the integrator becomes larger than I_{BM} causing the output voltage of the integrator to ramp downward at a rate set by the integrator time constant, i.e., τ_{ac}. Eventually, this output voltage becomes low enough to "turn on" the diode connected to the integrator's output. The result is a loss in field current dirve, reducing generator load and thus yielding lower generator armature current.

There is, however, a disadvantage to this implemented armature current limiter. An inherent delay exists from the time rated generator current is exceeded to the time when the output voltage of the integrator falls below the value that forward biases the diode connected to the integrator's output. This delay may be detrimental to generator operation, especially when rated armature current is exceeded in the case of battery voltage decrementation. As seen in Figure 29, a large spike in generator armature current results from battery voltage decrementation. The height of the spike, as well as its duration, is dependent on how quickly generator field current can be reduced after rated current is exceeded. A large delay in field current reduction can lead to excessive armature currents that may damage the machine. To reduce this delay time, a second time constant has been implemented in the integrator of the armature current limiter. This second time constant is implemented in a manner similar to the two time constant implementation in the shaftspeed controller. When the logic level $\bar{S}$ becomes low, occurring for a short time after battery-voltage switching, the FET in the armature current limiter becomes "pinched off". The result is an incremental decrease in integrator time constant. Otherwise, $\bar{S}$ remains high resulting in the FET conducting and a larger integrator time constant.

From an understanding of the operation of both field and armature current limiters, the purpose of the 27KΩ resistor at the output of the shaftspeed controller can now also be understood. This resistor is used to limit the output current of the buffer-inverter to prevent competition between the shaftspeed controller and the limiter control loops.

The final observation to be made on the analog control circuit of Figure 30 is in the two circuit outputs marked i_f and I_B, representing the field and armature current levels, respectively. These signals go to the logic circuit that makes the decision on when to switch battery voltage. This logic circuit, which also initiates battery section rotation as well as battery voltage switching, is the topic of the following section.

IV.1.b Implementation of Battery Section Rotation and Battery Voltage Switching

As described in Chapter III, two battery sections have been employed for the present implementation of the windmill power system. Figure 31 shows these battery sections in a diagram of the implemented battery charging circuit. The resistances associated with the smoothing choke, generator armature winding and internal battery power losses are not shown in this figure. However, the purpose of the figure is to emphasize that six SCR's must be controlled to perform the functions of battery section switching and battery section rotation.*

As shown in Figure 31, SCR "turn on" is initiated by closing the switch between the individual SCR's anode and gate. Connected in series with these SCR gate switches are resistors. When the forward voltage across the SCR becomes large enough to supply the required gate current through the gate resistor, the SCR "turns on".

*As mentioned earlier, the battery sections are electrically rotated to maintain uniform state-of-charge among the sections.

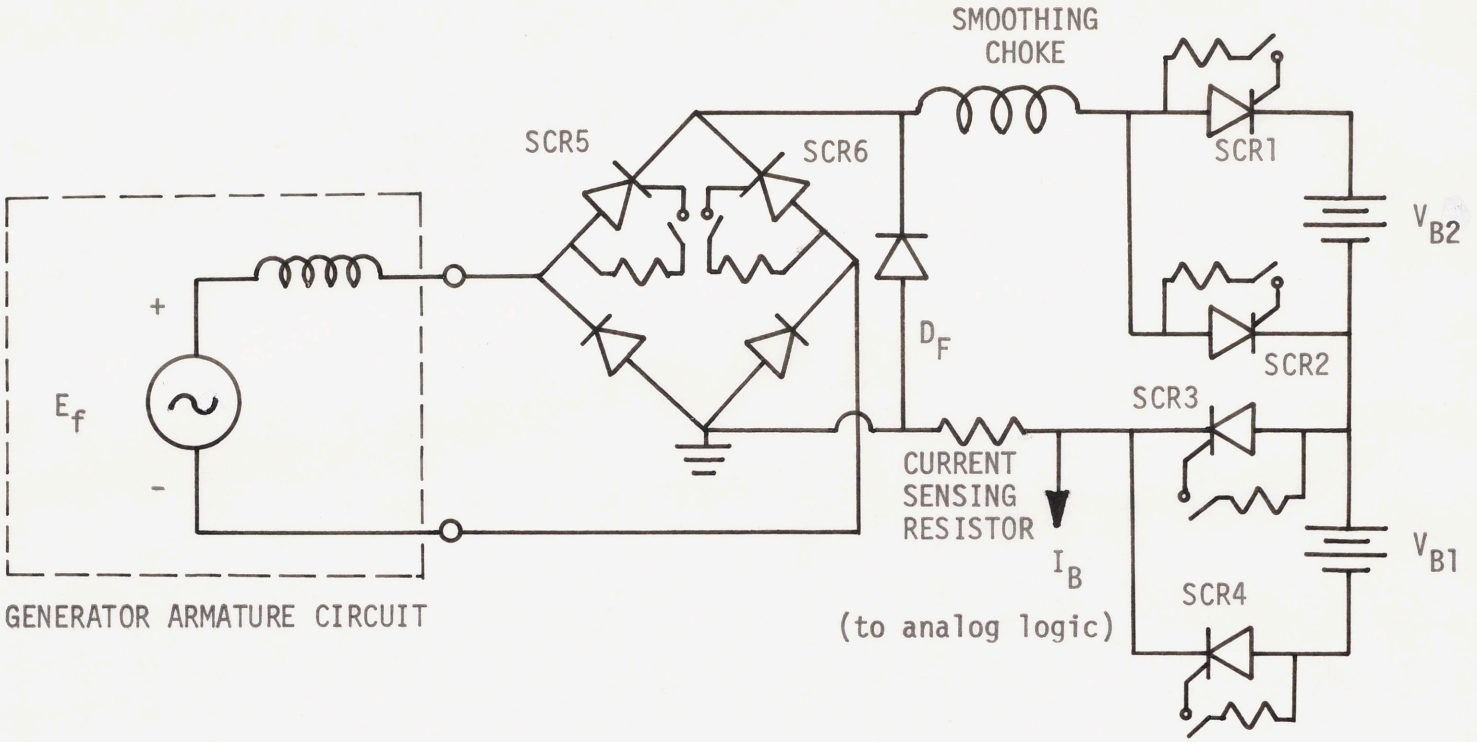

Figure 31 Battery Charging Circuit Showing Six SCR's to be Controlled

The processes of battery rotation and battery voltage switching require the removal of the battery charging current such that the appropriate battery SCR's (SCR1 through SCR4) can commutate. Charging current is removed by "turning off" the bridge SCR's in the charging circuit, i.e., opening switches S5 and S6 in Figure 31, and allowing the current to decay through the free wheeling diode, D_F. The current decays due to the back emf of the batteries.

With respect to the battery SCR's, the process of battery rotation involves alternatively opening and closing the switch pairs S_1-S_3 and S_2-S_4. This results in each battery section becoming alternately a part of the charging-current path. However, when the decision is made to rotate sections, the charging current must be removed prior to the closing of alternate gate-switch pairs. If switch S_2 is closed before SCR3 has been given time to commutate (in the case of battery rotation from sections V_{B2} to V_{B1}), then the conditions exist to "turn on" SCR2 resulting in the isolation of both battery sections from the charging circuit. This, in turn, results in insufficient back emf to reduce the charging current to zero in order to commutate the SCR's. Thus, when initiating battery rotation, the control circuitry must wait until the charging current has decayed to zero before closing alternate gate-switch pairs.

However, in the process of battery voltage switching, the positions of the gate switches may be alternated prior to reaching zero charging current. For battery incrementation switches S_1 and S_4 are closed and switches S_2 and S_3 are opened. For battery decrementation, switch position return to those positions set for

battery rotation. For these cases, there exists no possibility that both battery sections may be isolated from the charging circuit through the simultaneous "turning on" of both SCR2 and SCR3. Thus gate-switch positions may be altered instantaneously after the decision is made to alter battery voltage.

Now that the procedures for rotating and switching the battery sections have been established, the circuit implementation of these functions is possible. Three states can be identified for the battery bank load. The battery bank in Figure 31 may be in the states of charging either V_{B1} or V_{B2}, in the case of one charging section, or both battery sections may be charging. For the present circuit implementation a JK flip-flop and the output of a ripple counter are used to hold these states of the battery bank. The state of the flip-flop determines whether one or two battery sections are charging and the state of the Most Significant Bit (MSB) on the counter determines which battery section is connected to the circuit when only one section is charging. Digital logic is employed to alter the state of the flip-flop in accordance with the battery switching algorithms developed in Section III.2.b.

Figures 32 and 33 show the implemented logic circuit. From Figure 32 the state of the JK flip-flop, i.e., X, is dependent on the states of the armature current, I_B, field current, i_f, and wind velocity, v_w, inputs. X is triggered high, signifying battery voltage incrementation, when $I_B > I_{BM}$, maximum armature current, and $i_f < i_{fs}$, the field current at which switching is desired. X is triggered low when $i_f > i_{fm}$, maximum generator field current, and $v_w < v_{ws}$, the

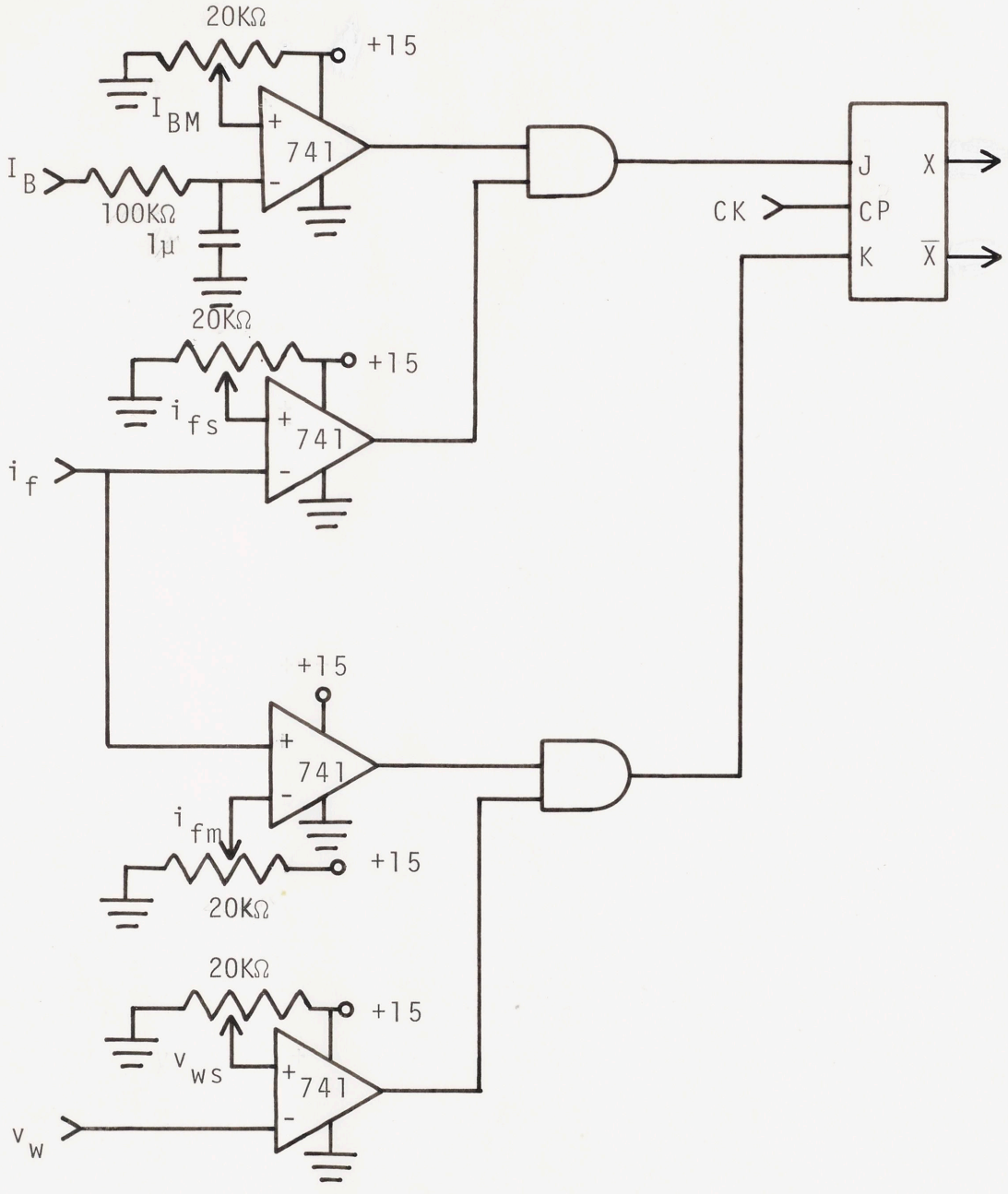

Figure 32 Implemented Logic Circuit

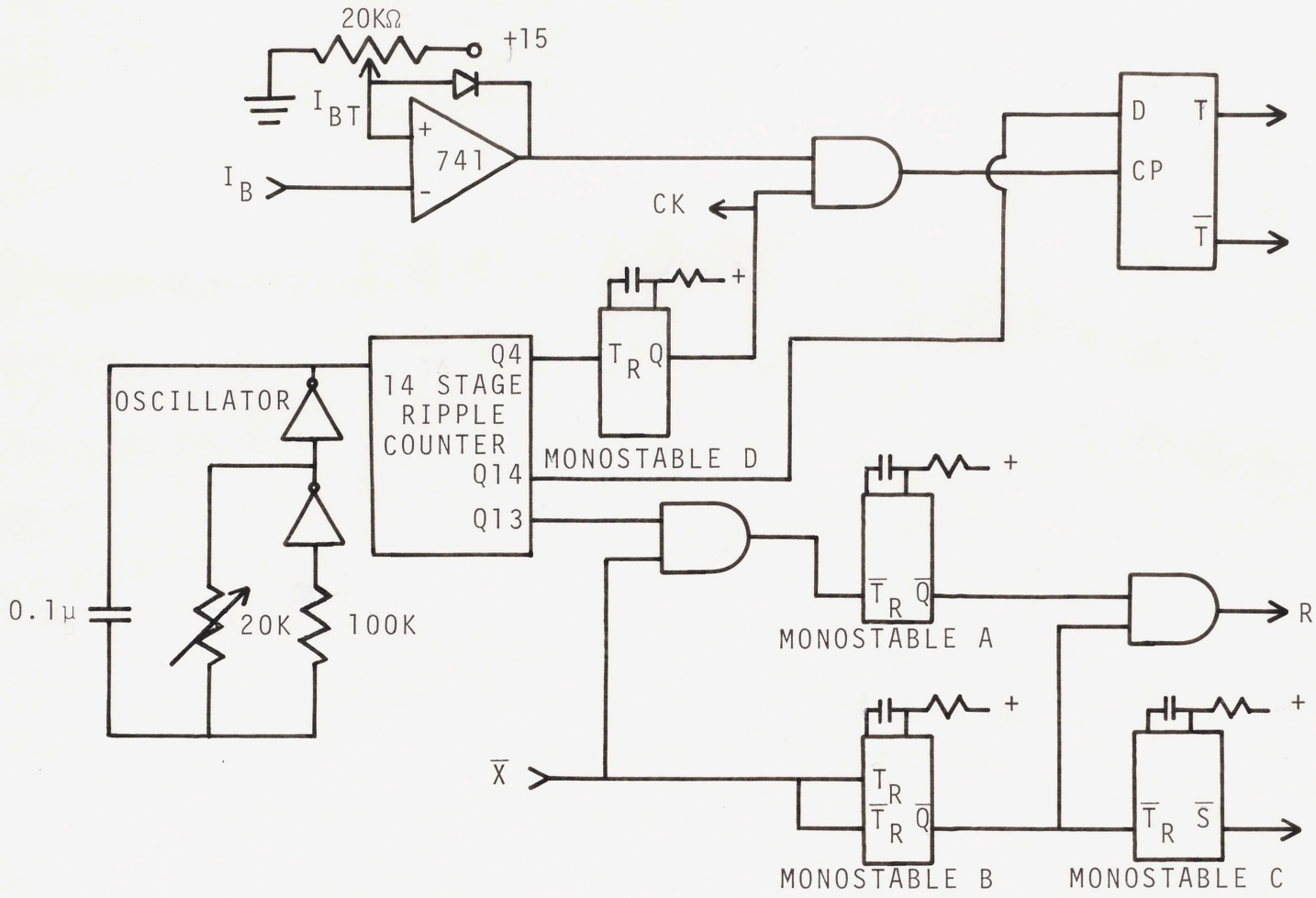

Figure 33 Implemented Logic Circuit.

desired switching point wind velocity. Operational amplifiers, shown in Figure 32, are used to make the comparison between these system variables and the set points. An RC filter is used at the input of the charging current comparators to filter out high frequency variations in the measured charging current.

Note that the above described algorithm for battery voltage decrementation is different than the algorithm developed in Section III.2.b. This is because this implemented algorithm yields no possible oscillation between load states as long as v_{ws} is chosen somewhat less than the switching point wind velocity.*

The state of the MSB (Q14) of the 14-stage ripple counter in Figure 33 determines which battery section charges. The frequency of the oscillator at the counter's input is set such that Q14 changes state every 8 seconds. However, to prevent the switching of the battery SCR's prior to the removal of battery charging current, Q14 has been wired to the input of a D flip-flop. The clock pulse to this flip-flop is inhibited until I_B, the battery charging current, falls below some very small value, I_{BT} in Figure 33. This comparison is again done using an operational amplifier. The output, T, of the D flip-flop is then decoded to appropriately alter the positions of the gate switches to the battery SCR's.

*See Figure 16 and related text for discussion of switching point wind velocity. Also see Section III.3 for discussion of oscillating load status.

The outputs of two monostables, A and B in Figure 33, are used to create the level R which sets the position of the gate switches to the bridge SCR's. These gate switches are opened, resulting in bridge "turn off", when either the level X changes state, signifying battery voltage switching, or when X is low and Q14 changes state, signifying battery rotation with only one charging battery section. Normally, the outputs of monostables A and B of Figure 33 are high resulting in R high. This situation corresponds to the bridge SCR's conducting current, i.e., the closed position of the gate switches to the bridge SCR's. However, when $\bar{X}$ changes state, monostable B is triggered resulting in R low for a short period of time. Also when $\bar{X}$ is high and Q14 changes state or, equivalently, $\bar{X}$ high and Q13, i.e., the second MSB in the counter, going through a high to low transition, then monostable A is triggered, again resulting in R low for a short period of time. Monostable C is triggered whenever there is a high to low transition at the output of monostable B, i.e., at the occurrence of battery voltage switching. The result is in $\bar{S}$ becoming low for a short period of time. This level, as discussed previously, is used to change the values of the time constants of the two integrators in the analog control circuit shown in Figure 30. Lastly, monostable D is used to create the short duration clock pulses for the JK and D flip-flops. The input to monostable D is from the fourth least significant bit of the counter, i.e., Q4. The frequency of these clock pulses is set at about 125 Hz.

The final circuit implementation involves decoding the states of X, T, and R in Figures 32 and 33 to determine the positions

of all the SCR gate switches as a function of the states of X, T and R. Table 1 summarizes the positions of all the SCR gate switches as a function of the states of X, T and R.

TABLE 1

POSITIONS OF SCR GATE SWITCHES AS A FUNCTION OF THE STATES OF X, T AND R

X	T	S_1	S_2	S_3	S_4
high	high or low	closed	open	open	closed
low	high	open	closed	open	closed
low	low	closed	open	closed	open

R	S_5	S_6
high	closed	closed
low	open	open

From these state tables the following excitation logic equations can be formed for the position of each SCR gate switch.

$$S_1 \text{ (closed)} = \overline{\bar{X}T}$$

$$S_2 \text{ (closed)} = \bar{X}T = \overline{S_1 \text{ (closed)}}$$

$$S_3 \text{ (closed)} = \bar{X}\bar{T}$$

$$S_4 \text{ (closed)} = \overline{\bar{X}\bar{T}} = \overline{S_3 \text{ (closed)}}$$

$$S_5 \text{ (closed)} = R$$

$$S_6 \text{ (closed)} = R = S_5 \text{ (closed)}$$

Figures 34 and 35 show the circuit implementation of these excitation equations. SCR optical isolators are used as the gate switches to the main SCR's. Transistors are used to drive the necessary input current to each isolator when the associated main SCR is required to "turn on". Light-emitting diodes (LED) are used at the outputs of each transistor to physically indicate which SCR is being gated.

The implementation of battery rotation and battery voltage switching is now complete. The following section shows some of the more interesting properties and functions of the designed control circuitry before final system testing and evaluation is conducted in Chapter V.

IV.2 Control Circuitry Test Results

Two preliminary tests were conducted to show a few of the properties of the implemented control circuitry. The results of the first test, depicted in Figure 36, shows the battery charging current at the occurrence of battery section rotation. Also shown in the figure is the output of the D flip-flop, T in Figure 33. A change in the level of T marks the point in time when the gate switches to the battery SCR's alternate position such that battery section rotation

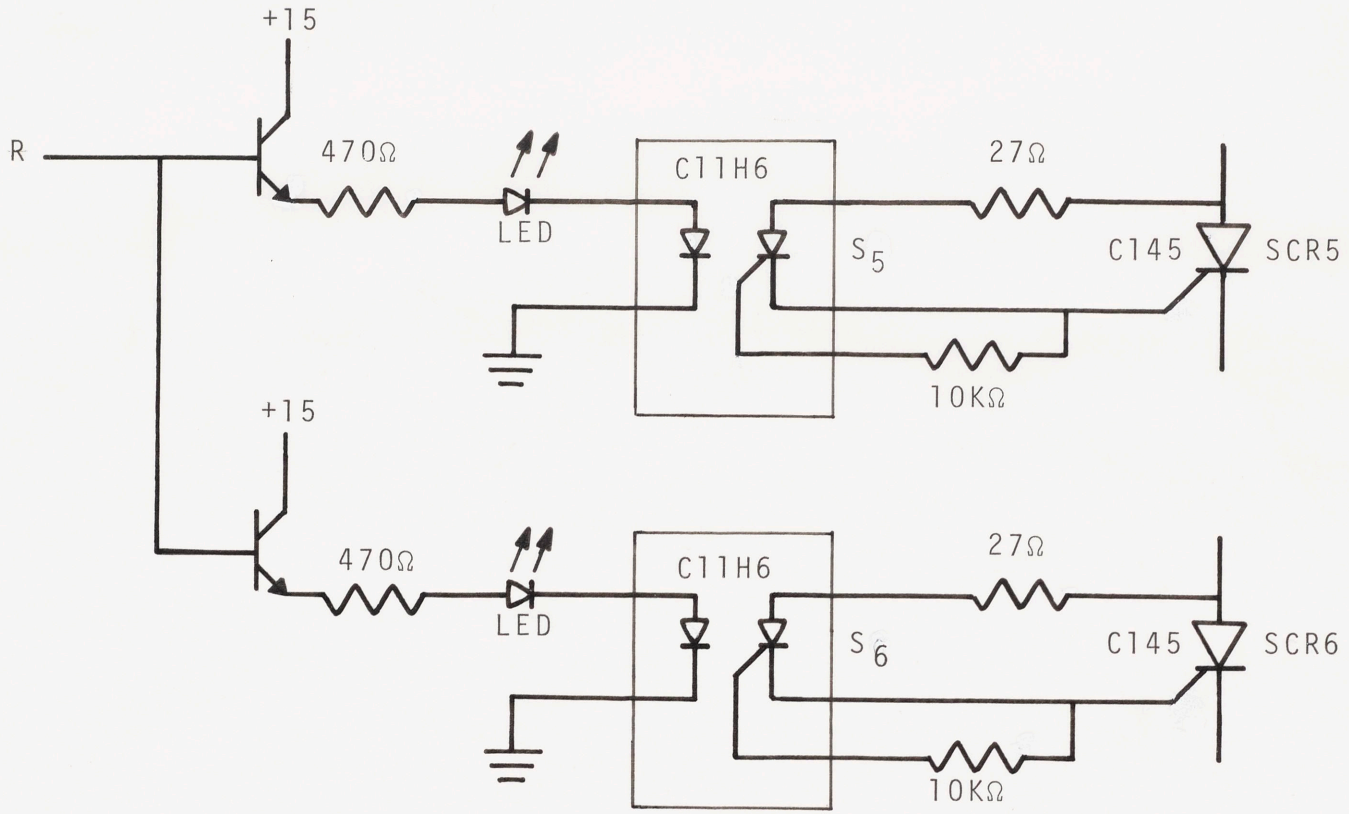

Figure 34 Decoding Logic and SCR Switch Implementation

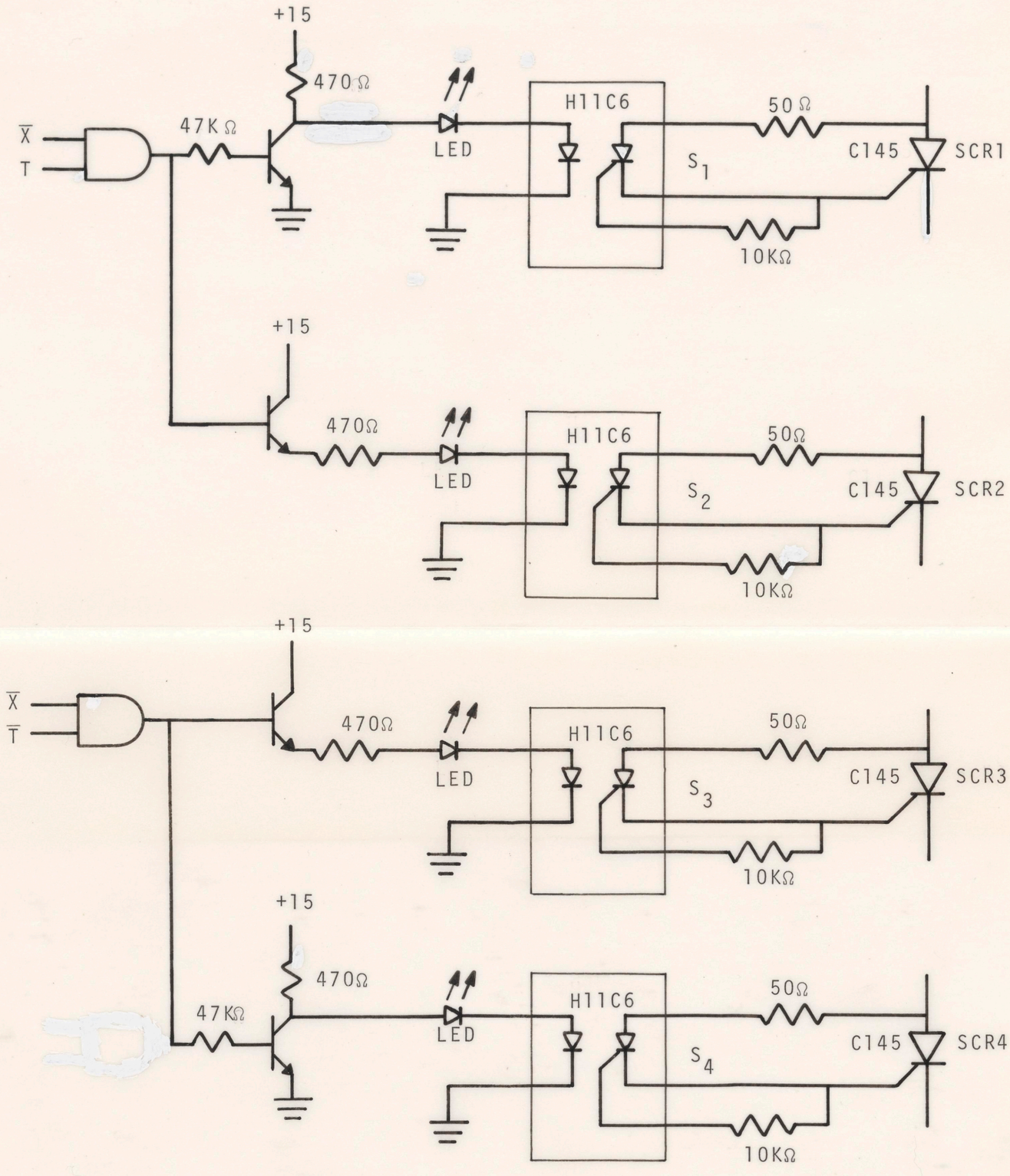

Figure 35 Decoding Logic and SCR Switch Implementation

is achieved. Figure 36 shows the rapid decay in charging current through the free wheeling diode after the bridge SCR's are "turned off". Only after the charging current becomes zero are the gate switches at the battery SCR's allowed to alternate position. This is shown by the change in level T which occurs at the first clock-pulse after the charging current reaches zero. A short time later, set by the RC time constant of monostable A in Figure 33, the gate switches to the bridge SCR are reclosed allowing current to flow into the alternate battery section. As seen from Figure 36, the total time that no power flows out of the generator is approximately 10 ms.

The high ripple in the armature current in Figure 36 is due to the small inductance of the smoothing choke used in the charging circuit. However, this small inductance allows the battery charging current to decay rapidly after the bridge SCR's are "turned off". This decay time is about 2-3 msec as seen in Figure 36. The choice of smoothing choke inductance used in the actual charging circuit is discussed in Appendix G.

Lastly, from Figure 36, notice the larger average charging current after battery rotation is complete. This larger current only occurs initially after the rotation due to the different terminal characteristics presented by the alternate battery section. These different characteristics are, in part, due to recovery having occurred in the alternate battery section during the 8 second period that it was not being charged. Also, nonuniform states-of-charge between the battery sections accounts for the rest of this current difference.

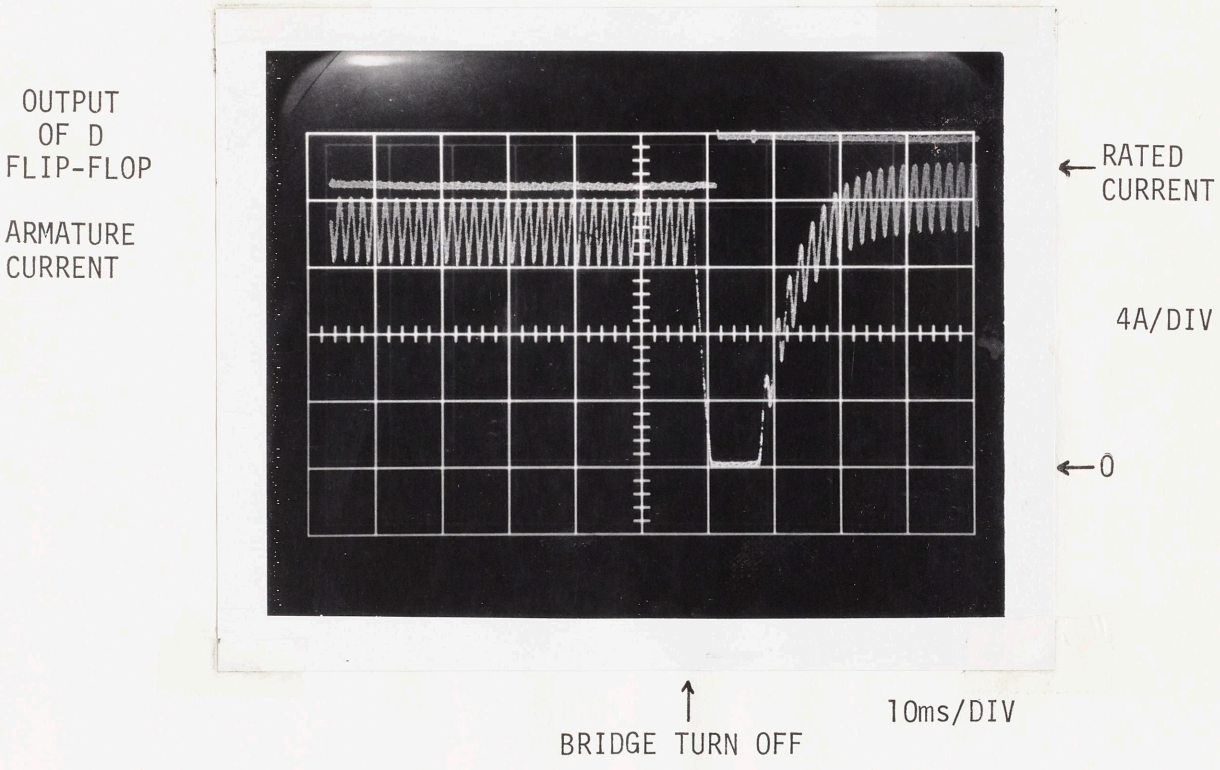

Figure 36 Generator Armature Current at the Occurrence of Battery Switching

The second test conducted on the control circuitry shows the dynamics associated with generator armature current limiting. Figure 37 shows two responses of generator armature current at the occurrence of battery voltage decrementation. The only parameter change that results in the two different responses is the choice of integrator time constant, τ_{ac}, in the armature current limiting circuit. The figures show that prior to battery decrementation the charging current is reduced to zero by "turning off" the bridge SCR's. However, when the bridge is again "turned on" the armature current almost instantly exceeds rating by more than 50%, being only limited by charging circuit resistance and generator armature inductance.

The results in Figure 37(a) were achieved with τ_{ac} = 0.03 seconds. Notice the delay, approximately, 0.1 seconds, prior to the reduction in armature current due to the reduction in generator field current drive. (The slower reduction in armature current during the delay is due to the slow recovery of internal generator inductance, transient inductance to synchronous inductance, after the large current transient.) The delay is due to the nature of the armature current limiter implementation, as previously described in Section IV.1.a. To reduce this delay, the integrator time constant, τ_{ac}, was decreased to 0.01 seconds. Figure 37(b) shows the new response to the armature current surge after battery voltage decrementation. The implementation of this faster time constant greatly reduces the delay in the occurrence of field current reduction when rated armature current is exceeded. However, as seen from Figure 37(b), oscillation results about the rated armature current level. This oscillation may be attributed to

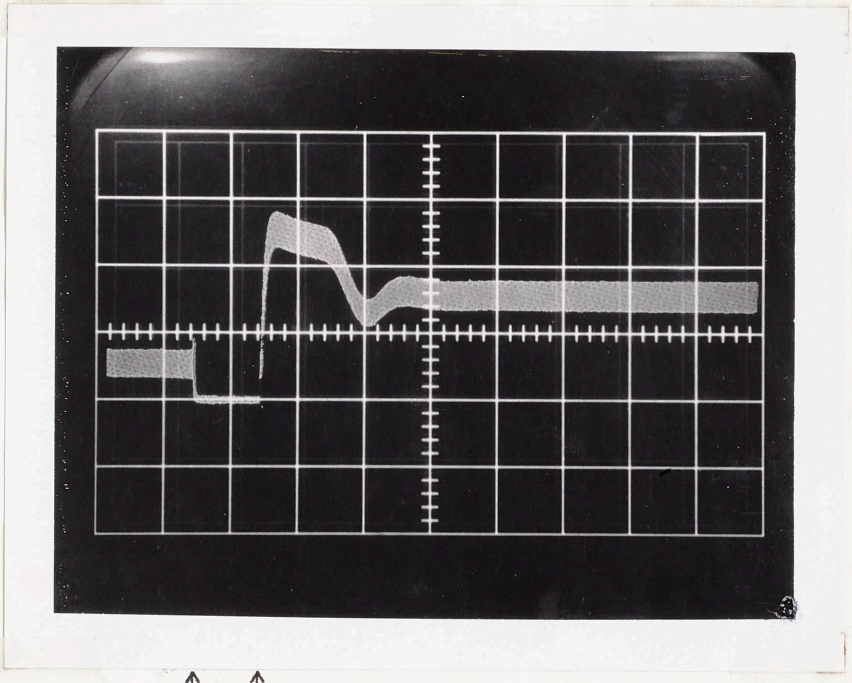

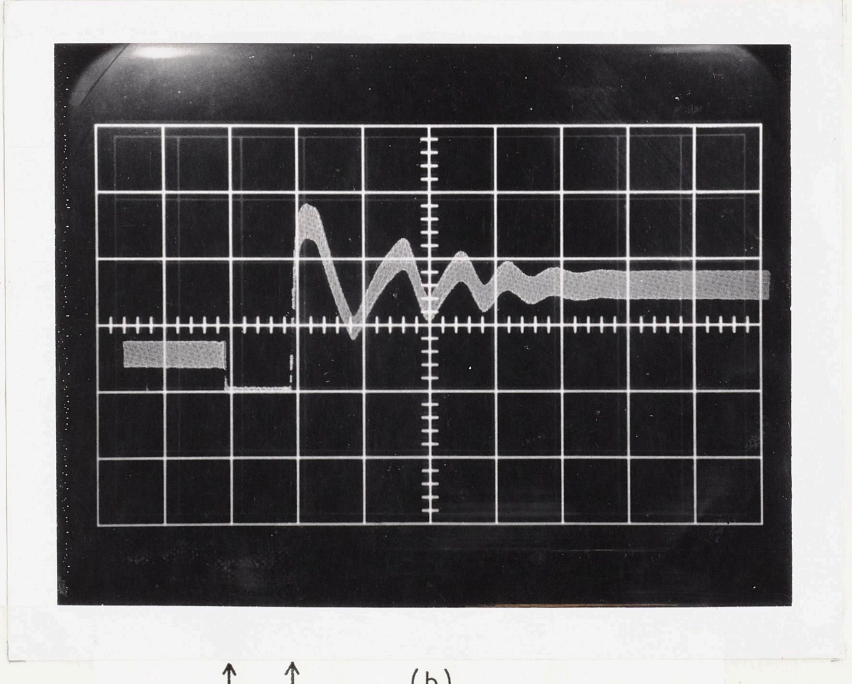

Figure 37 Armature Current Limiter Dynamics

two factors. Firstly, the loop again around the armature-current-limiter feedback is increased when τ_{ac} is decreased, as shown in the control system schematic of Figure 14. This increased loop gain results in decreased loop stability. Secondly, the switching between dominant feedback loops, i.e., the change in the switch position in Figure 14, is not perfect. Delays still exist in this switching, for example, from the time rated armature current is exceeded to the time that the armature current limiter circuit reduces field current drive. Also, possible competition between the feedback loops may also result in poorer system behavior.

From Figure 37, it seems evident that larger values of τ_{ac} produce more well behaved dynamics associated with armature current limiting, i.e., less oscillation occurs in the waveform with larger τ_{ac}. Also, as seen from the results of the computer simulation in Figure 29, a more well behaved response occurs in the case of both a larger time constant, i.e., τ_{ac} = 0.1 sec, and the implementation of virtually no integrator delay. Therefore, an improved circuit implementation of the armature current limiter would involve zero switching delay between the shaftspeed controller and armature current limiter control loops. However, this does not completely solve the problem. As shown in the computer simulation, a large current spike still occurs. Further study is therefore needed in reducing the current surge after batter decrementation.

IV.3 Summary

This chapter showed a possible implementation of the analog control laws and battery switching algorithms developed for both the

efficient and well behaved operation of the windmill power system. The analog control consisted of three modes of field current control with the implementation of two integrator time constants for both shaftspeed controller and armature current limiter. However, in the implementation of the armature current limiter an inherent delay exists from the time rated armature current is exceeded to the time of occurrence of the limiting. This delay was shown to be detrimental to the functioning of armature current limiting in the case of battery voltage decrementation. Thus an improved implementation is necessary.

In implementing battery section rotation and battery voltage switching, the control of six SCR switches was shown to be necessary. An important requirement in the case of battery rotation is the removal of battery charging current prior to the gating of alternate battery SCR's. However, this is not a stringent requirement in the case of battery voltage switching as long as charging current is removed to allow the commutation of the battery SCR's.

CHAPTER V

PHYSICAL SCALE MODEL SIMULATION OF STEADY-STATE AND DYNAMIC BEHAVIORS OF THE WINDMILL POWER SYSTEM

This chapter presents the measured steady-state and dynamic behaviors of the implemented physical model windmill power system. These measured results will be compared with the computer simulation results of Chapter III. The objective is to see how well the measured results correlate with the behavior predicted by the analytic model of the power system. The actual description of the physical model system is presented in Appendices B through E. The control implementation for the power system was presented in the previous chapter.

V.1 Steady-State Behavior of the Physical Model System

In Chapter III the results of a steady-state computer simulation of the model windmill power system were presented. Curves were plotted showing generator power output, stored battery power, and system efficiency as a function of wind velocity. Figures 16 and 17 show these results with the system battery bank at a nominal state-of-charge.

Similar power and efficiency curves were obtained from measurements on the physical scale model system. Figures 38 and 39 show the results of these system measurements with the battery bank at an intermediate state-of-charge. The variables shown in these figures are defined in Section III.1 and correspond to the variables shown in Figs. 16 and 17. As in the calculated curves, i.e., those shown in Figs. 16 and 17, the curves of Figs. 38 and 39 have been plotted

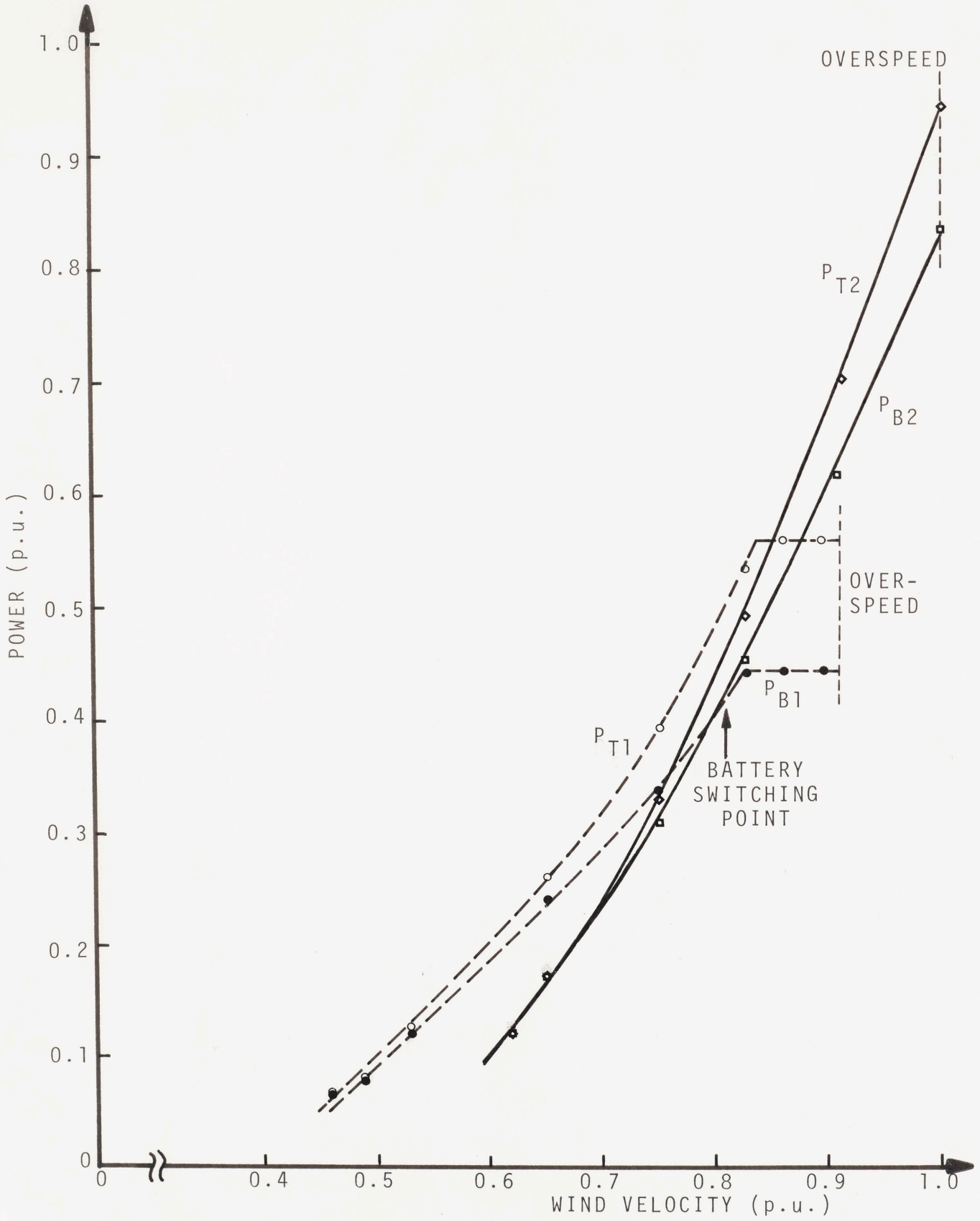

Figure 38 Measure Generator Power Output and Stored Battery Powers as a Function of Wind Velocity for a Nominally Charged Battery Bank

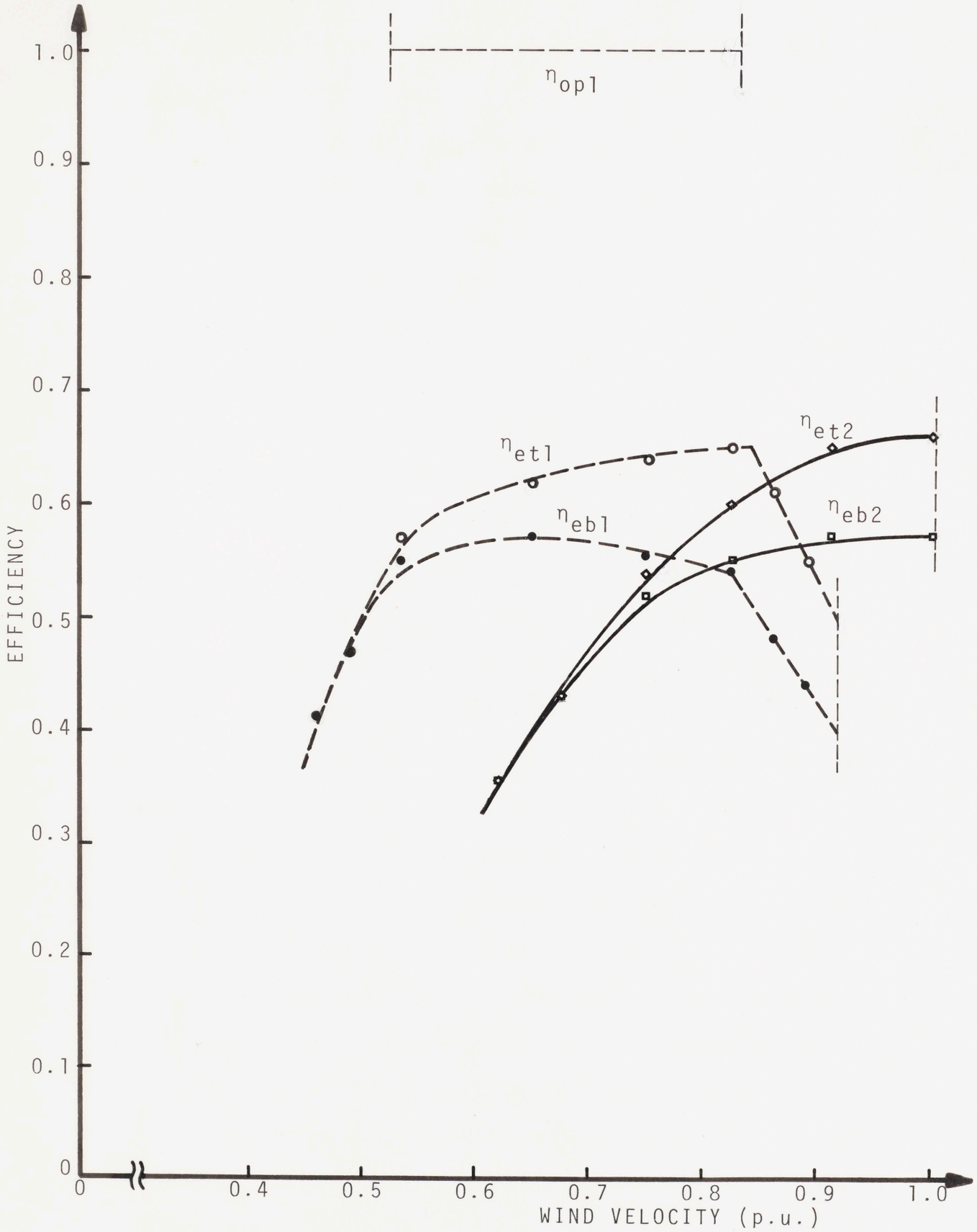

Figure 39 Measured System Operating and Extraction Efficiency as a Function of Wind Speed for a Nominal State-of-Charge Battery Bank.

only up to those wind velocities where rated shaftspeed is attained for the respective battery loads.

For one charging battery section of the two section battery bank the P_{T1} and P_{B1} characteristics were obtained, for a given wind speed, by adjusting generator field excitation until the battery charging current reached a maximum value. At this point of operation the power being stored in the batteries is also at a maximum for that wind velocity. This stored power, P_{B1}, is estimated as the product of the maximum charging current and the open-circuit battery voltage. Also, for this wind velocity, P_{T1} is simply measured by noting the generator power output at this point of maximum charging current operation.

As discussed in Chapter II, maximum system operating efficiency, i.e. operation at the peak of the battery "input" characteristic, is attainable only at those wind velocities where maximum charging current operation occurs in the unconstrained region of generator operation. For this region of operation both generator field and armature currents are below their limiting values.

For the physical scale model system, Fig. 39 shows the range of wind velocities where maximum system operating efficiency is achieved with one charging battery section, i.e. where $\eta_{op1} = 1$. Only in this range of wind velocities is maximum charging current attained without reaching the generator's field or armature limit. For wind velocities below this range η_{op1} fall below unity due to generator field current limitations. For wind velocities above the range where $\eta_{op1} = 1$, the generator armature current constraint limits system efficiency.

Note from Fig. 39 that the plot of η_{op1}, i.e., the measured system operating efficiency for one charging battery section, is incomplete. This is because in the constrained regions of system operation where field or armature current limiting occurs, operating efficiency is not measurable. To determine values for η_{op1} in these operating regions requires knowledge of the peak value of the battery "input" characteristic (see definition of η_{op} in Chapter II). However, due to the generator constraints, this peak value can never be physically attained, and thus cannot be measured.

In the case of two charging battery sections, i.e., charging the full battery bank voltage, the operation of the physical system never occurs at maximum operating efficiency. As predicted by the windmill power system model of Chapter II, the greatest generator output in this case is achieved by maintaining maximum excitation on the generator field. P_{T2} and P_{B2} in Fig. 38 show the measured generator output and stored battery powers as a function of wind velocity for the two battery section load. Note that the operating efficiency of this full-battery-bank load, i.e. η_{op2}, is not plotted in Fig. 39. This is because maximum field current operation, occurring when charging two battery sections, does not allow η_{op2} to be measured.

Figure 39 also shows the measured "generator terminal extraction efficiencies", η_{et1} and η_{et2}, and "battery extraction efficiencies", η_{eb1} and η_{eb2}, for the two respective battery loads. At a given wind velocity these quantities are obtained by taking the quotient of the measured P_T and P_B values and the power into the windmill simulator

at that simulated wind speed.*

In comparing the measured results of Figs. 38 and 39 to the calculated curves of Figs. 16 and 17, much similarity is seen between the respective curves. Note especially that range of wind velocities where overall system efficiency, shown by η_{eb1} and η_{eb2} for one and two battery sections, respectively, and power conversion capability, P_{B1} and P_{B2} for the respective battery loads, is improved by charging one battery section instead of the full battery bank. As shown in Figs. 38 and 39, this improvement occurs for all wind speeds below 0.82 per unit, i.e. where $P_{B1} > P_{B2}$. Thus, the ability to charge battery voltages that are less than the full battery bank voltage increases the effective utility of this windmill energy conversion system.

Several noticeable differences, however, can be seen between the calculated and measured steady-state results. Firstly, for most wind speeds the power output of the generator, curves marked P_T, is less in the actual model system than in the computer simulation results. This power discrepancy is also reflected in the generally lower values for the efficiencies of Fig. 39 as compared with their counterpart efficiencies in Fig. 17. These differences may be attributed to errors made in both the measuring and the modeling of system power losses. A significant component of this error may be attributed to generator stray losses. These losses, which were estimated by performing a short-circuit test on the generator

*See Appendix D for discussion of windmill simulator.

(see Appendix E.3), may be much larger under actual load conditions than in the test. Also, the crude manner in which these losses are estimated (again, see Appendix E.3) may also result in substantial errors in the modeling of these losses.

A second discrepancy between calculated and measured steady-state system behavior is seen in the absolute power difference between respective P_T and P_B curves. This power difference, signifying power losses in the battery charging circuit, including battery losses, is much larger for the measured curves (Fig. 38) than in the calculated curves (Fig. 16). This discrepancy is believed to be related to the increase of internal battery voltage as a function of charging current.* This effect, if taken into account when estimating the P_B curves in Fig. 38, results in a larger value for P_B than is shown in the figure. The greater value for P_B is because, under charging conditions, the internal battery voltage is actually larger than the open-circuit value of this voltage originally used in estimating P_B. Thus the actual difference between respective P_B and P_T curves is less than the difference shown in Fig. 38.

A third source of discrepancy between the measured and calculated power-windspeed characteristics may be different battery states-of-charge in the two cases. This factor may, for example, account for

*When obtaining the measured results, the battery terminal voltage as a function of charging current was observed. The terminal voltage increased much more rapidly with charging current than can be attributed to the measured battery characteristics modeled in Appendix C. This observation may be attributed to the internal battery voltage increasing with charging current.

the different location of the battery switching point, i.e., where $P_{B1} = P_{B2}$, in the measured curves as opposed to calculated characteristics. In the case of the measured curves, this switching point does not occur on the flat portion of the P_{B1} curve in Fig. 38 as is predicted in Fig. 16. However, as a result of the computer simulation in Section II.1, the location of the battery switching point was found to depend on battery state-of-charge. Thus, this state-of-charge factor may account for the observed difference in the location of battery switching point between the measured and calculated power-windspeed characteristics.

Measurements of the P_T and P_B characteristics and system efficiency were also obtained for the physical system with the batteries at both low and high states-of-charge. Figures 40 and 41 and Figures 42 and 43 show these measured results for low and high battery states-of-charge, respectively. These results can be compared with the calculated results shown in Figs. 18 and 19 and Figs. 20 and 21. The largest discrepancy between these measured and calculated curves is seen for wind velocities below the battery switching point. For these wind speeds, the power gained by charging one battery section instead of two sections is measured to be less than that predicted by the calculated curves. This difference is believed to be due to increasing internal battery voltage as a function of battery state-of-charge, an effect not modeled in obtaining the calculated curves. However, to validate this belief, the simulated curves may be recalculated taking into account

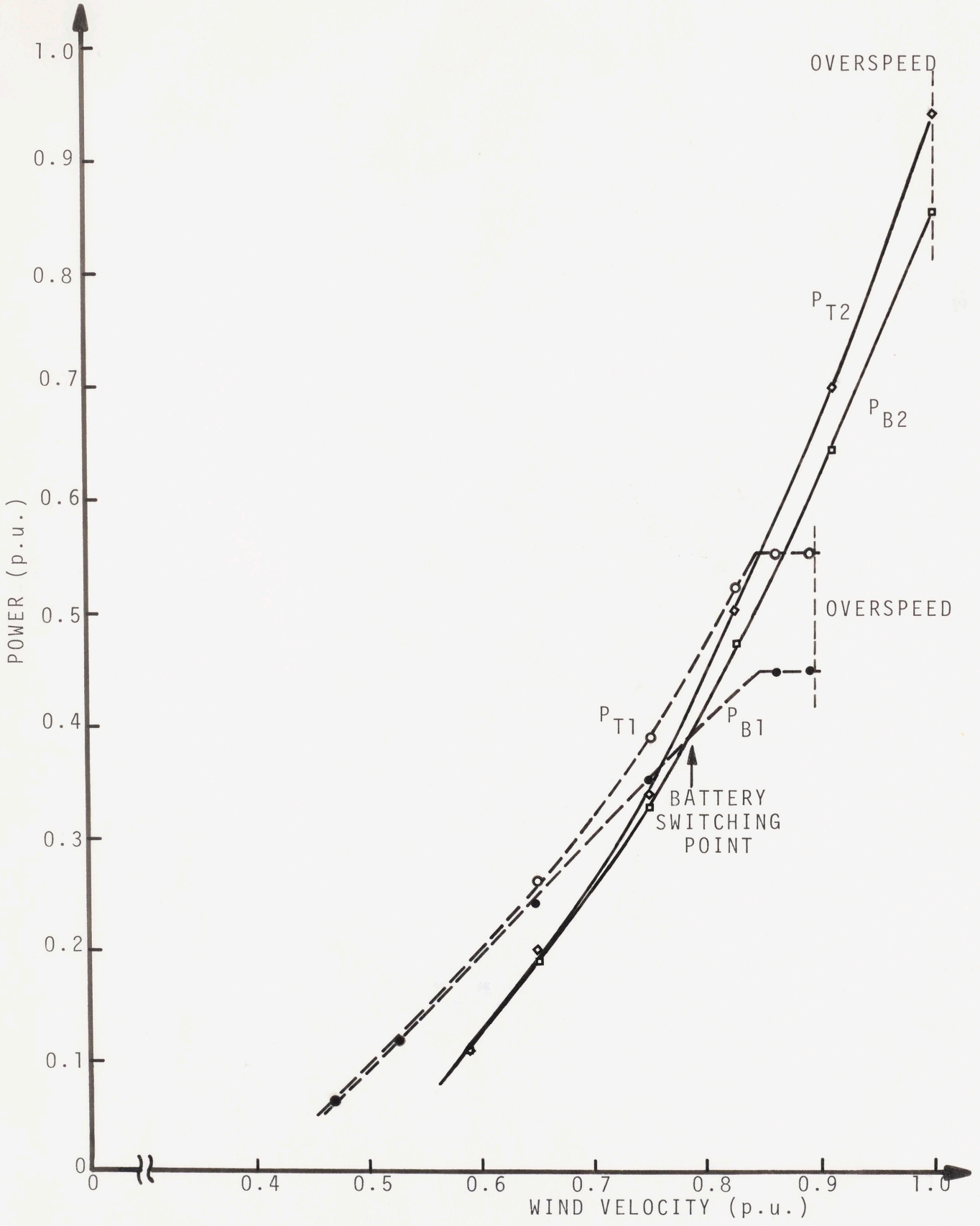

Figure 40 Measured Generator Output and Stored Battery Power as a Function of Wind Velocity for a Low State-of-Charge Battery Bank.

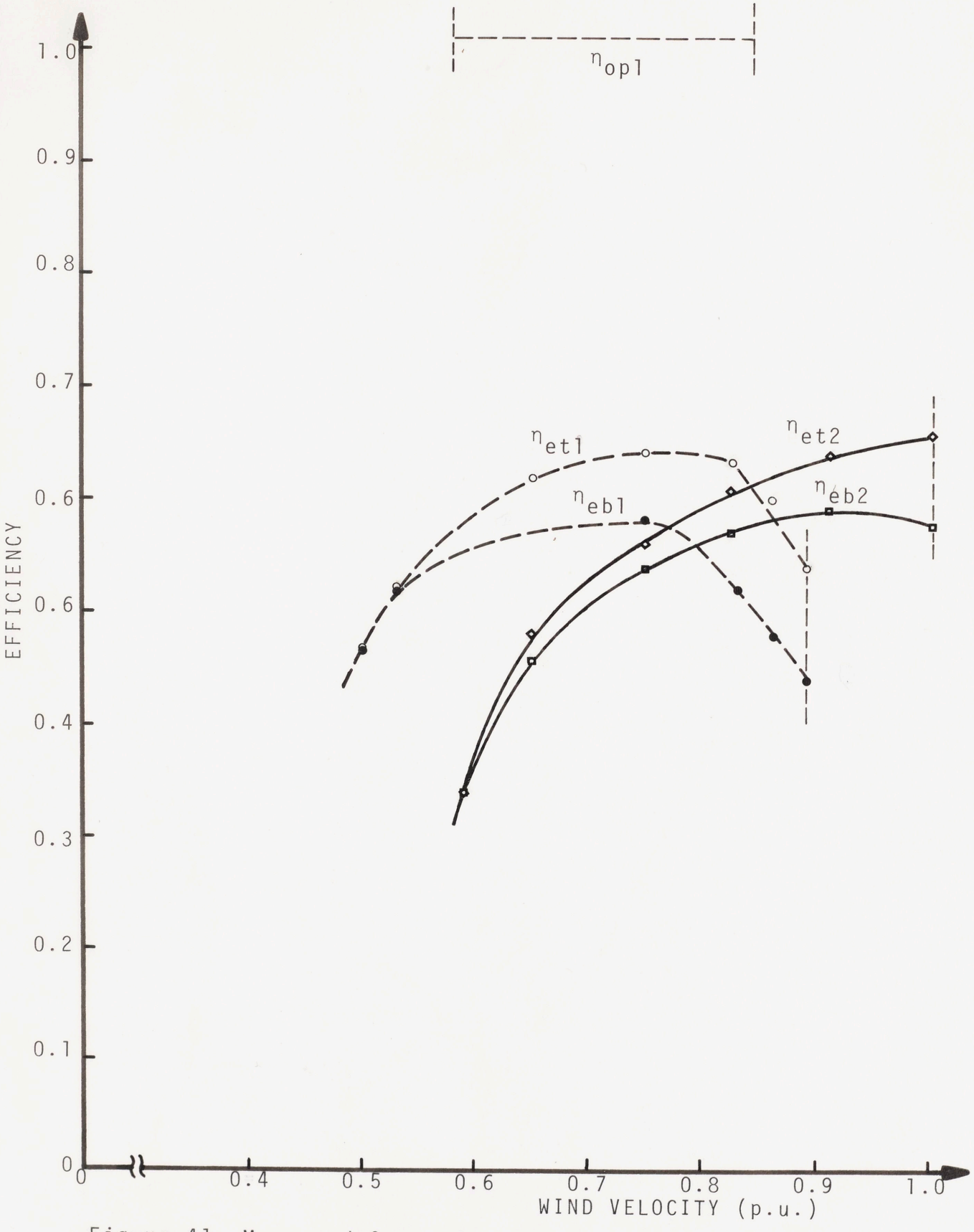

Figure 41 Measured Operating and Extraction Efficiencies as a Function of Wind Speed for a Low State-of-Charge Battery Bank.

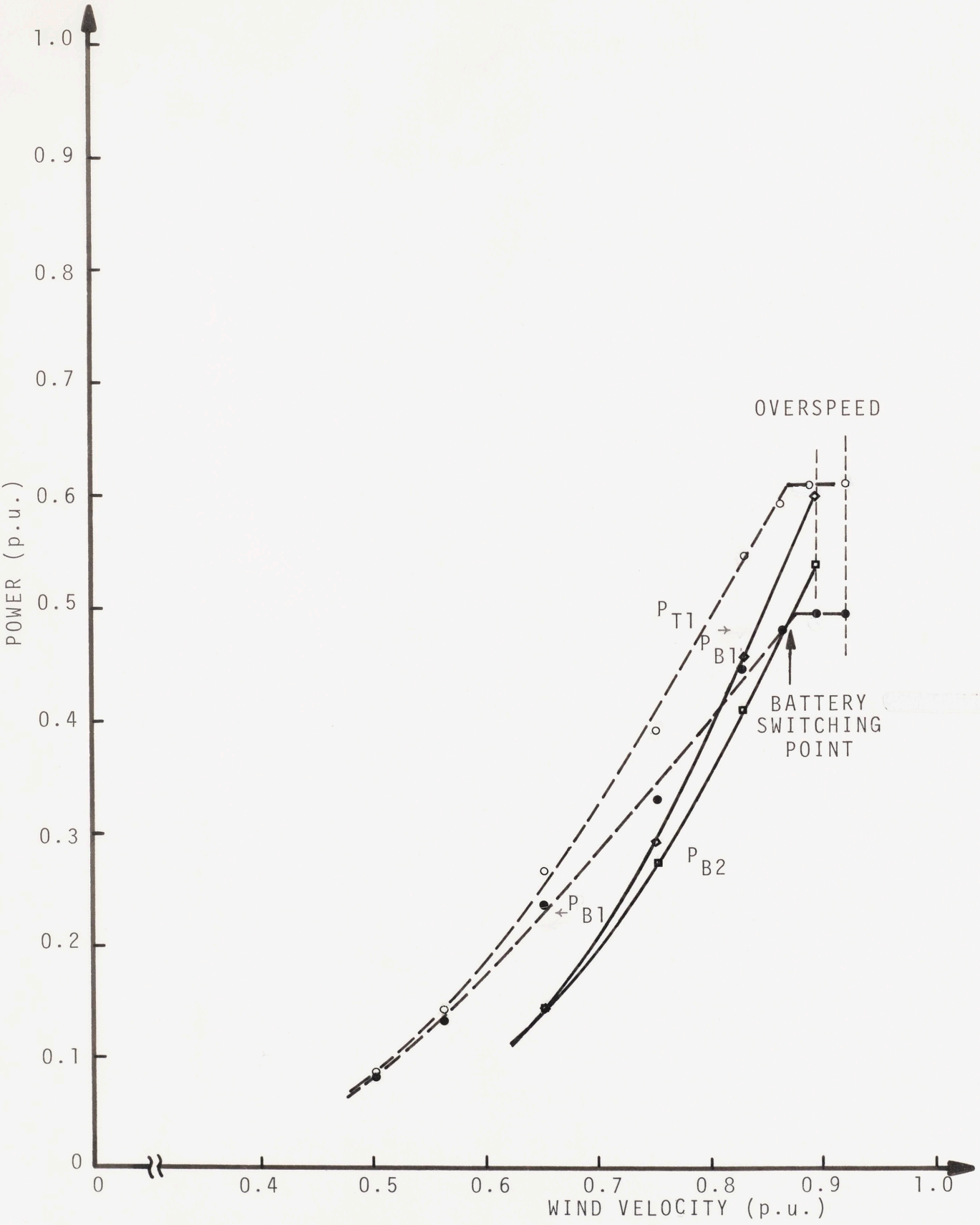

Fugure 42 Measured Generator Power Output and Stored Battery Power as a Function of Wind Speed for a High State-of-Charge Battery Bank.

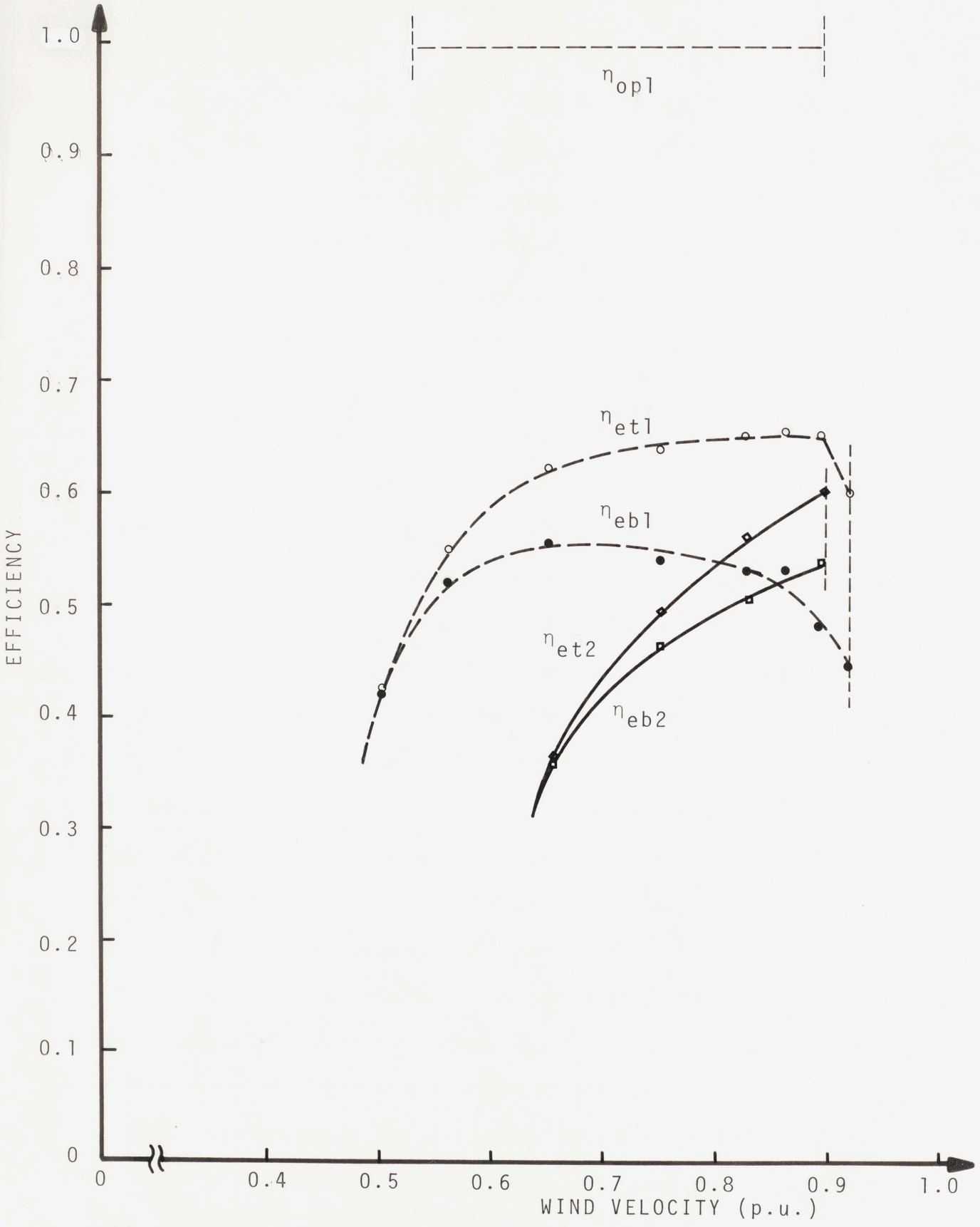

Figure 43 Measured System Operating and Extraction Efficiencies as a Function of Wind Velocity for a High State-of-Charge Battery Bank

this new battery condition.

In comparing the measurements of Figs. 42 and 43, i.e., high state-of-charge case, to the measurements of Figs. 38 and 39, i.e., intermediate state-of-charge case, system power conversion capability is observed to be greatly reduced in the former case as expected. At this high state-of-charge the batteries can no longer present the required load to the generator. As seen in Figs. 42 and 43, shaft overspeed in this high state-of-charge case occurs at a much lower wind velocity than in the intermediate state-of-charge case.

In the low state-of-charge case, Figs. 41 and 42, generator armature current limiting is not observed with two sections charging at high wind velocities, an effect seen in the calculated curves of Fig. 18. Armature current limiting does not occur under these conditions because the electrical power conversion of the system is not large enough to warrant this limiting. As previously mentioned, the power losses in the actual system were measured to be greater than the losses in the simulated system. If this power difference had been converted instead of lost then armature current limiting may have occurred at these high wind velocities due to the inability of the batteries to accept the increased generator output.

Another observation concerning the series of measured power-windspeed characteristics, i.e., Figs. 38, 40 and 42, is the variation in battery switching point as a function of battery state-of-charge. Note that, as predicted in the calculated results of Section III.1, the wind speed corresponding to the battery switching point increases

with battery state-of-charge.

The final system measurements presented in this section are the locations of the desired operating shaftspeed as a function of wind velocity, i.e., $\omega_{so}(v_w)$ as described in Section III.2. These measurements, as described previously, can only be obtained in the unconstrained region of generator operation. Only in this region can operation occur at the peak of the battery input characteristic. Figure 44 shows the measured values of $\omega_{so}(v_w)$ for the battery bank at an intermediate state-of-charge. Also drawn in this figure is the curve showing the variation in ω_{so} as calculated by the computer simulation for a battery bank at a nominal state-of-charge (see Fig. 22). The correlation between the measured and predicted results is fairly accurate. Discrepancies between these results may be due to unequal battery states-of-charge in the two cases.

In summary, this section presented the results of measurements made on the steady-state behavior of the physical model windmill power system. Accurate correlation was observed between the measured and calculated power and efficiency curves plotted as a function of wind velocity. This correlation was also shown to be accurate in the cases of off-nominal battery states-of-charge. The major result seen from these figures is that windmill power system efficiency can be greatly improved if the ability to switch between battery voltages is available to the system.

Two major sources of error between the measured and calculated curves were also discussed in this section. These were, firstly, errors made in measuring and modeling system power losses, especially

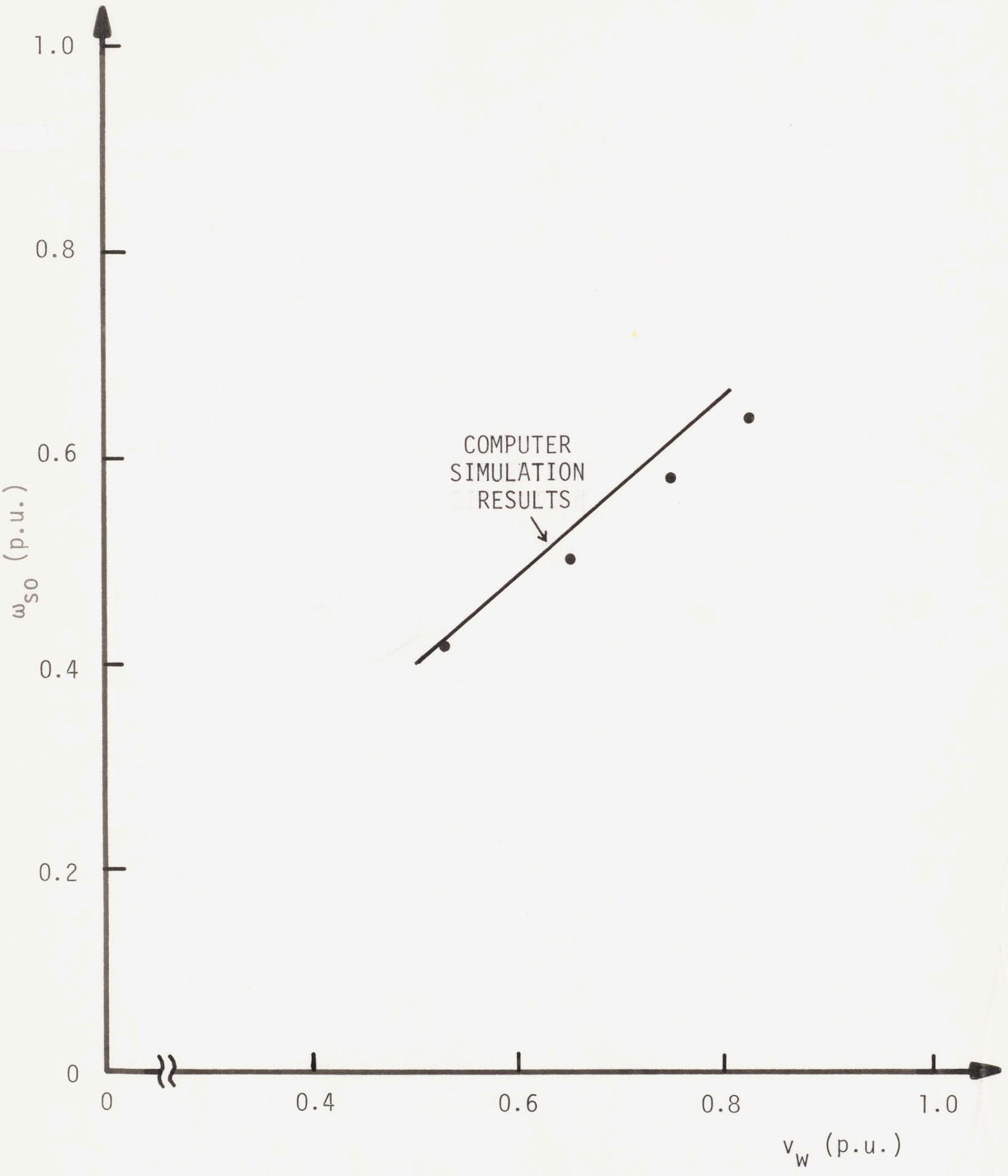

Figure 44 Measured and Calculated Desired Shaftspeed as a Function of Wind Velocity

generator stray losses, and secondly, variations in system behavior caused by the internal battery voltage varying as a function of battery charging current.

Lastly, desired system shaftspeed as a function of wind speed, i.e., $\omega_{so}(v_w)$, was also measured and plotted along with the predicted results. Accurate correlation was observed between these measured and calculated results.

V.2 Dynamic Behavior of Physical Model System

Chapter III presented the results of a computer simulation to determine the dynamic behavior of the windmill power system. Two types of dynamics were discussed. These were the dynamics associated with changes in wind velocity alone and dynamics associated with battery voltage switching. The purpose of this section is to present the observed dynamics of the physical model system. This behavior is also to be compared with the results of Chapter III. Again, as in Chapter III, the two types of dynamics inherent to the windmill power system are discussed separately in this section.

V.2.a Dynamics Associated with Wind Velocity Changes

The discussions presented in Section II.3 and Section II.2.a showed that the choice of generator field current time constant, τ_f, is critical to determine the shaftspeed behavior of the windmill power system. Also, from the results of the computer simulation in Section III.2.a, the choice of τ_f is only important in the unconstrained region of system operation, i.e., in that region of operation where field current control is used to maintain system operation along a desired

locus with respect to wind velocity.

Figure 45 presents the results of four tests performed on the windmill power system to determine the effect of the field current time constant on system behavior.* These dynamics are the result of an 0.1 per unit step increase in wind velocity from an initial speed of 0.7 p.u. Results are presented for four different field time constants.

From the photographs of Fig. 45, as the field current time constant is increased, greater damping is observed in the physical system. This effect is predicted in the computer simulations of Section III.2.a; see Fig. 23. Also, note the field current limiting that occurs during the transients in Figs. 45(c) and 45(d), e.g., between t = 2 to 4 seconds in Fig. 45(d). As discussed in Chapters II and III, the system becomes first order in nature during maximum field current operation. This behavior is present in both Figs. 45(c) and 45(d).

Figures 45(a) and 45(b) can be directly compared with the result of the digital computer simulation of Chapter II. The simulated curve marked "original C_p curvature" in Fig. 28 and the curve marked "v_{wo} = 0.7" in Fig. 24 correspond to the same conditions that resulted in the behavior seen in Figs. 45(a) and 45(b), respectively. Note

*The large high-frequency ripple associated with the field current in the figure is due to coupling of the magnetic flux produced by the armature current to the generator field circuit. When magnified onto a larger scale, this field variation is identical to the ripple current present in the rectified armature current waveform. This field current ripple is an inherent property of a single-phase generator where the negative sequence flux wave present in the machine induces a substantial voltage in the field winding.

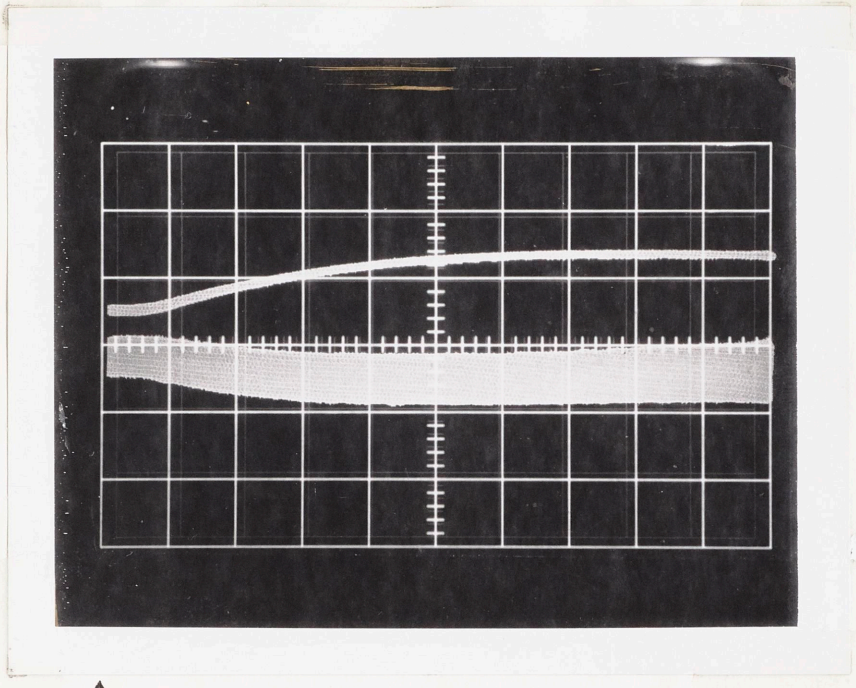

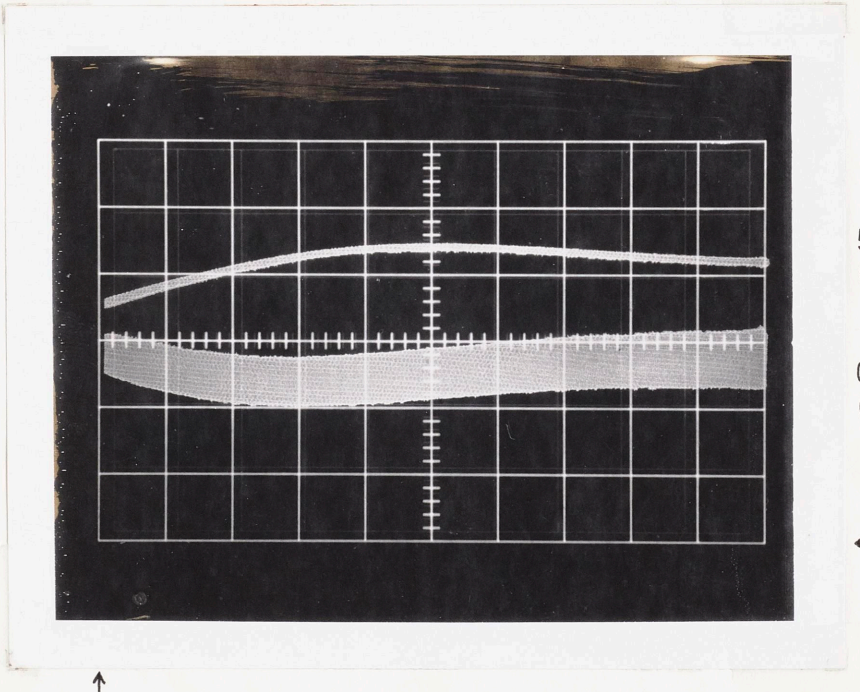

Figure 45 Shaftspeed and Field Current Dynamics for a 0.1 Step in Wind Speed from an Initial Speed of 0.7 p.u. The Value for τ_f is Marked for Each Case.

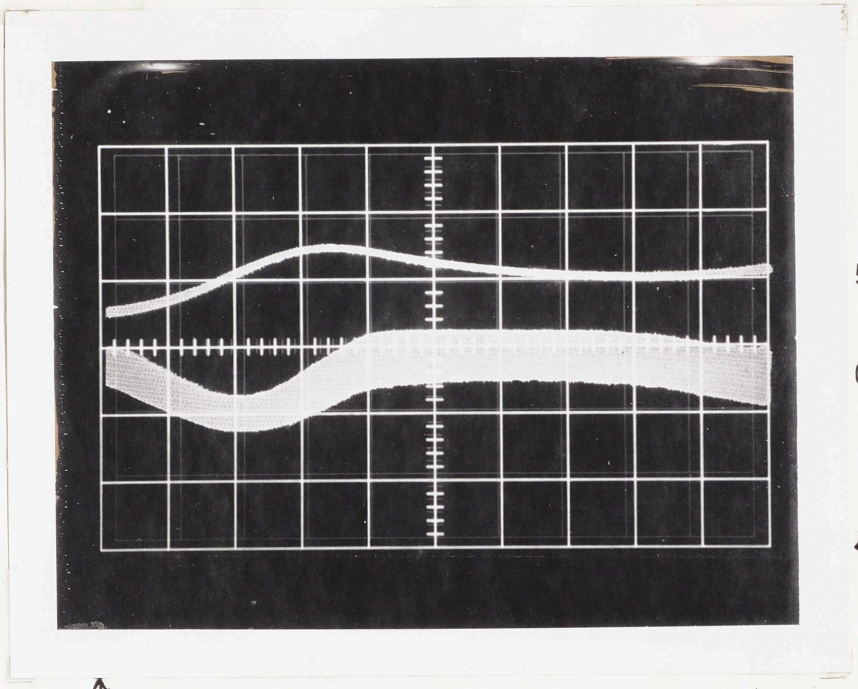

SHAFTSPEED

FIELD CURRENT

τ_f=0.25 sec

525rpm/div (0.15pu/div)

0.2A/div (0.5pu/div)

←0

↑ 0

(c)

0.5sec/div

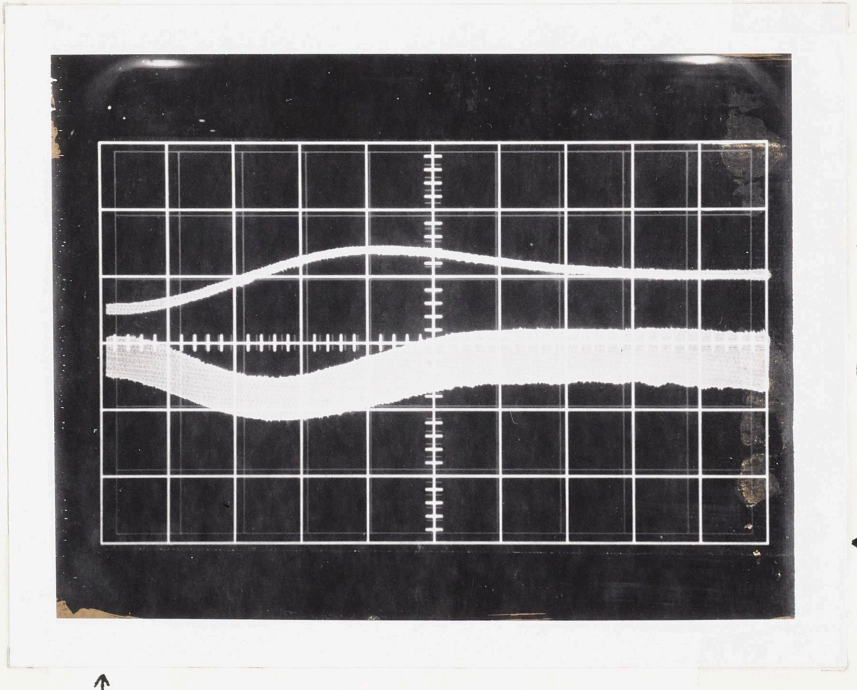

SHAFTSPEED

FIELD CURRENT

τ_f=0.13 sec

525rpm/div (0.15pu/div)

0.2A/div (0.5pu/div)

←0

↑ 0

(d)

0.5sec/div

Figure 45 (continued)

the very similar dynamics present in these two pairs of responses. However, the dynamics present in the physical system seem slightly better damped than the simulated dynamics. This discrepancy may be due to errors in calculating the H constant ($\frac{1}{2} J \frac{\omega_{s(base)}^2}{P_{t(base)}}$) of the system. Like the field current time constant, the H constant acts as a gain in the dynamic feedback loop of the system (see Fig. 14 and related discussion in section II.3). As this gain changes the dynamics of the system also changes. Moreover, any deviation in the gain of the control circuitry, e.g., variation in the gain of the buffer-inverter in Fig. 30 due to resistance tolerances, also results in different system behavior due to a different gain around the control loop. A third source of discrepancy between the measured and simulated dynamics may be due to the lower system efficiency that was measured in the physical system compared with the simulated model system, as discussed in Section V.1. The larger power losses associated with this lower efficiency add increased damping to the system and thus may account for the better behavior of the dynamics seen in Figs. 45(a) and 45(b) as opposed to the computer results in Fig. 25 (curve marked "original C_p") and Fig. 24 (curve marked "$v_{wo} = 0.7$"), respectively.

The response in Fig. 46 is shown to demonstrate the behavior of the power system when charging two battery sections. This figure shows the first order behavior of the shaftspeed predicted by the computer simulation results of Section III.2.a, i.e., results shown

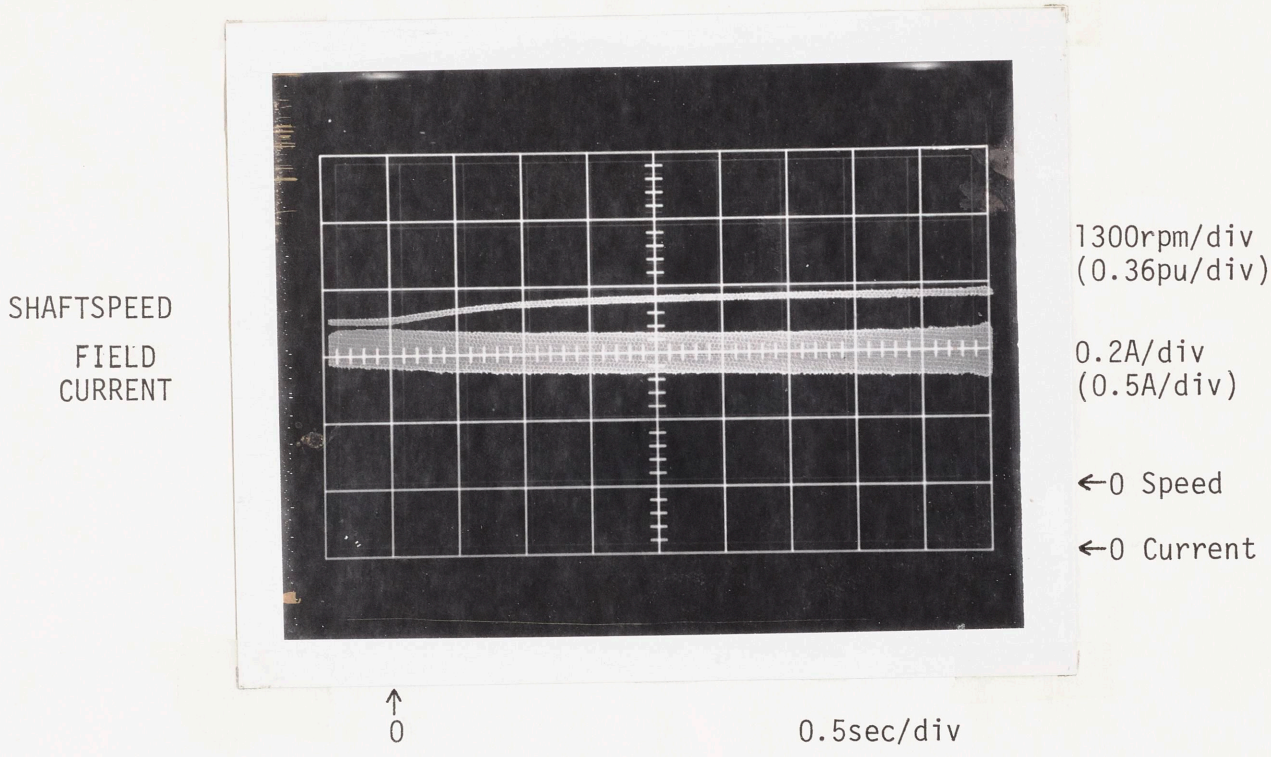

Figure 46 Shaftspeed and Field Current Dynamics for a 0.1 Step in Wind Velocity from an Initial Speed of 0.9 p.u. for Two Charging Sections.

in Fig. 24 for v_w = 0.85. The behavior exhibited in Fig. 46 is for a 0.1 p.u. step in wind velocity from an initial wind speed of 0.9 p.u. The value of τ_f in this response is inconsequential due to maximum field current operation exhibited for the duration of the response. Note from this figure that the new steady-state shaftspeed is achieved within two seconds of the initiation of the transient. This response is consistent with the behavior indicated in the computer results of Fig. 24.

In summary, this section presented the measured system dynamics associated with variations in wind velocity. The dynamics predicted by the computer simulation of Section III.2.a correspond very well with the observed responses of the physical model system. The choice of field current time constant is seen to be critical to system performance. From Fig. 45(a) a choice of τ_f = 1.0 sec results in a well behaved system; this time constant results in a critically damped response. Discrepancies between the measured and calculated results are associated with errors in the calculation of the gains of the control loop components, e.g., errors in calculating system H constant or errors associated with tolerances in the circuit components. Also, the larger power losses measured in the physical model system may account for the increased damping present in the measured responses compared with that observed in the computer simulation.

V.2.b Dynamics Associated with Battery Voltage Switching

As discussed in Section III.2.b, battery voltage switching produces an instantaneous change in generator load characteristics.

As shown in that section, system behavior is dependent on the rate with which generator field current excitation can be increased after the switching.

Figure 47 shows the measured dynamics associated with the incrementation of battery voltage for the physical windmill power system. The conditions for switching resulted from a 0.1 step in wind speed from an initial speed of 0.83 p.u. The two different behaviors present in Fig. 47 result from the implementation of different values of field current time constant, τ_f, after the switching. Prior to switching, the field current time constant is 1 second for both cases shown in Fig. 47. This is the value which results in a well behaved system in the case of wind velocity dynamics (see Fig. 45(a)). Notice the overshoot in shaftspeed in Fig. 47(a) when τ_f remains unchanged after the switching. However, for the smaller time constant implemented after switching, i.e., τ_f = 0.05 sec. in Fig. 47(b), no overshoot in generator shaftspeed is observed.*

The results of Fig. 47 can be compared with the computer simulated results shown in Fig. 27. Note that, in the actual system, the dynamics appear more well behaved, i.e., more damped, than in the simulated system. The discrepancies between the results may be again due to the same sources of error discussed in Section V.2.a. These errors are associated with both the calculation of the gains of the system control

*The slightly higher steady-state shaftspeed seen in Fig. 47(b) as compared with Fig. 47(a) is due to a slightly higher final wind velocity in the former case.

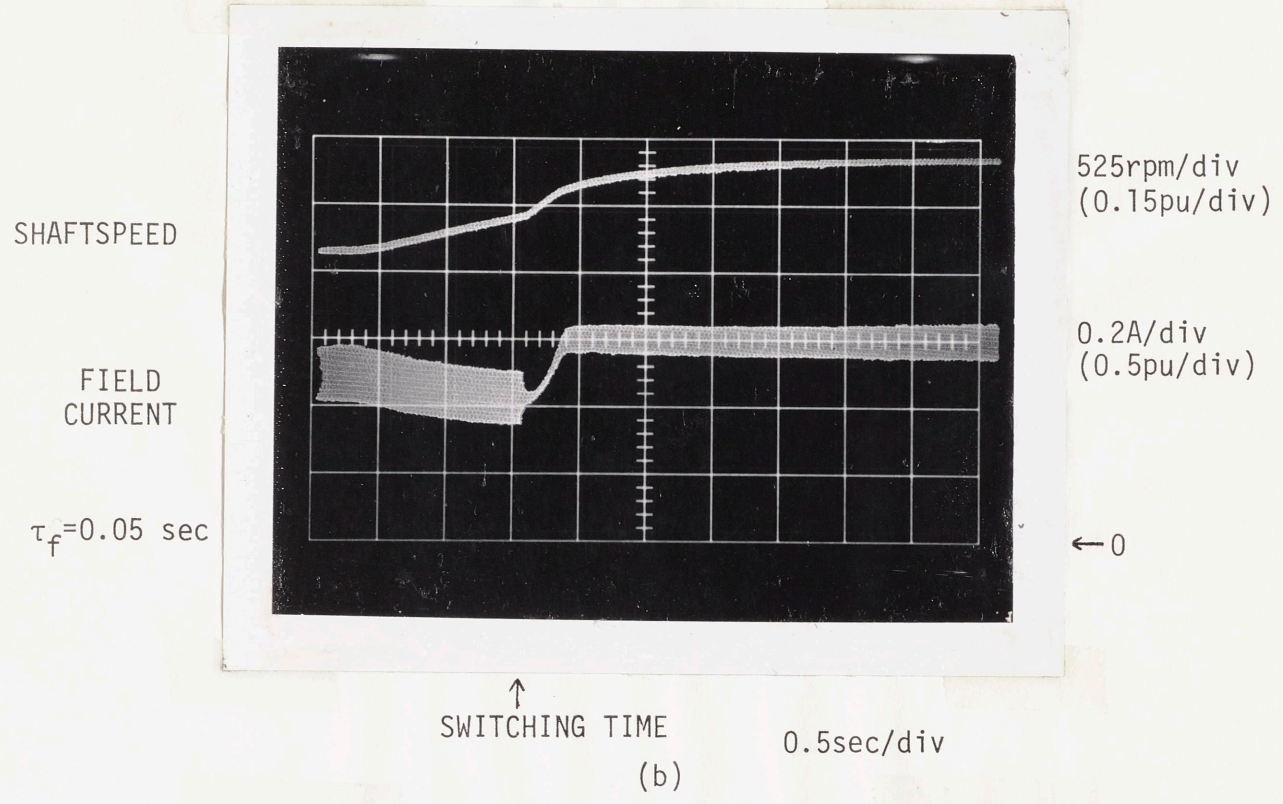

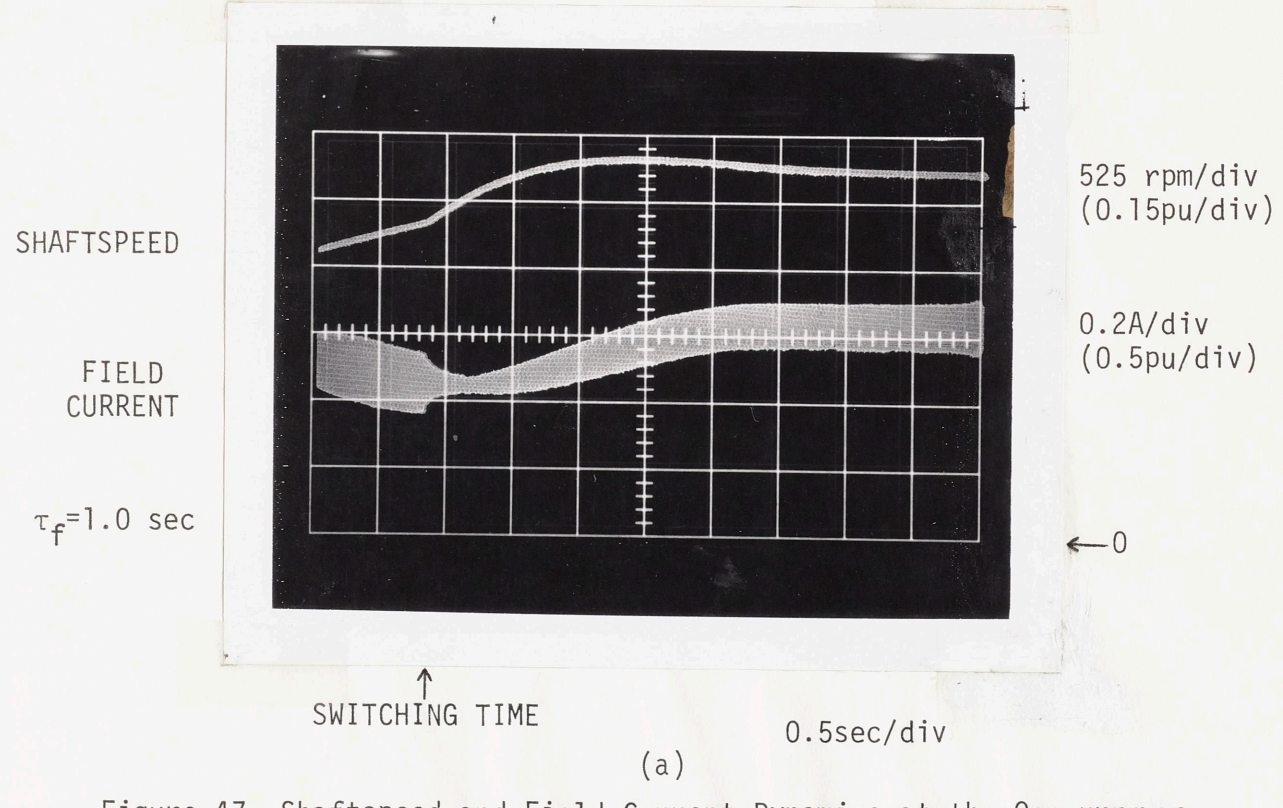

Figure 47 Shaftspeed and Field Current Dynamics at the Occurrence of Battery Voltage Incrementation. Dynamics Shown are for Two Values of τ_f where Switching is Initiated by a Step in Wind.

loop components and the increased power losses measured in the system.

Lastly, Fig. 48 shows system dynamics at the occurrence of battery voltage decrementation. The conditions for switching result from a 0.07 p.u. decrement in wind speed from an initial speed of 0.83 p.u. For this case, the field current time constant remains at τ_f = 1 seconds, i.e., the value that results in well behaved dynamics for wind velocity variations, for the duration of the response. Also the time constant associated with the armature current limiter feedback loop, i.e., τ_{ac}, is 0.1 seconds in this case (see Section II.3 for discussion of τ_{ac}). As previously discussed in Section III.2.b(ii) and Section IV.2, a large current spike occurs in the battery charging current immediately after the battery voltage decrementation. As discussed in Section IV.2, at the occurrence of this armature current surge, the field current behaves in the manner to reduce the surge. Thus, as seen in Fig. 48, after a delay of 0.3 seconds the field current is rapidly reduced. (The undesirable delay is an inherent property of the implemented control circuitry, see Section IV.2). After armature current is reduced below rating, the slower field current time constant, τ_f, is again implemented. This can be seen, in Fig. 48, by the less rapid variation in field current after the sharp decrease of this current.

Also note the shaftspeed transient in Fig. 48. For the first 0.3 seconds after switching the shaftspeed declines more rapidly than in the time following this decline. This is due to the substantial loading of the generator caused by the armature current surge during

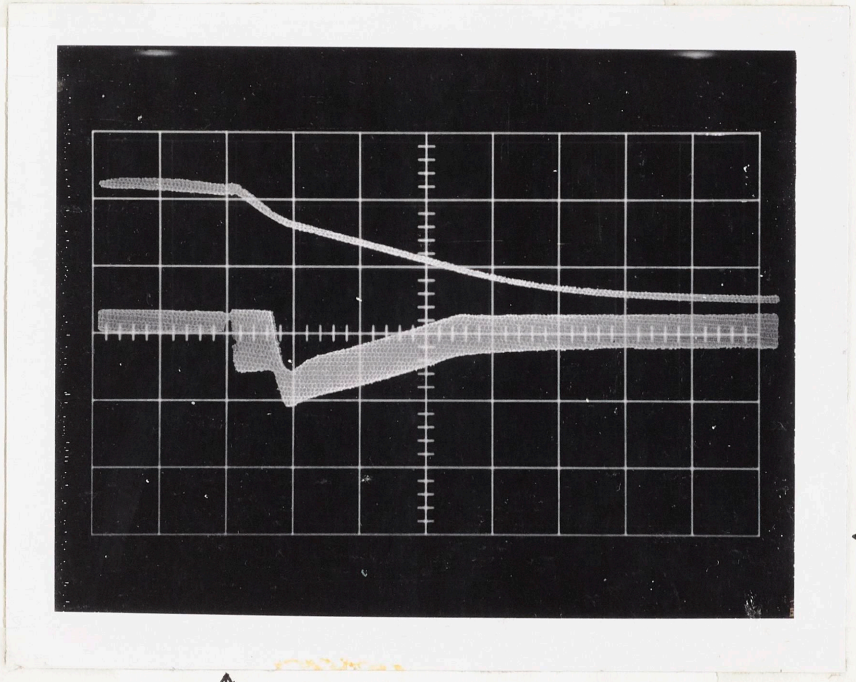

Figure 48 Shaftspeed and Field Current Dynamics at the Occurance of Battery Voltage Decrementation. Battery Switching is Initiated by a Step Decrease in Wind Speed.

this interval. Once the current surge dissipates, due to field current reduction, this decline in shaftspeed is more gradual. Further discussion of the armature current surge associated with battery voltage decrementation is found in Sections III.2.b(ii) and IV.2, as previously mentioned.

These measured results concerning battery voltage decrementation may be compared with the computer simulation results of Fig. 29, Section III.2.b(ii). Notice the very similar shaftspeed dynamics present in both cases. The greatest discrepancy between the results is in field current behavior after switching. This is due to no delay exhibited in the reduction of field drive in the computer simulation of Fig. 29 after the armature current surge.

In summary, this section presented the results of tests performed to determine the dynamic performance of the physical model system at the occurrence of battery voltage switching. In the case of battery voltage incrementation, the choice of field current time constant during the transient determines system behavior. For well behaved dynamics, a much smaller value for τ_f is necessary during this transient than in the case of transients caused by variations in wind velocity alone. Also, in the case of battery voltage decrementation, the armature current surge after the switching may be detrimental to system performance. During this surge, rated armature current is exceeded and a large load transient is exhibited.

APPENDIX A

WINDMILL POWER SYSTEM DESCRIPTION AND WINDMILL MODELING

The purpose of this appendix is to present information obtained from Reference 2 that is relevant to this thesis.

Windmill Power System Description

A simplified block diagram of the proposed windmill power system is shown in Fig. A.1. To achieve maximum power transfer from the wind to the battery load, the coordination of the design of the three component subsystems is necessary.

Windmill Modeling

The total power available in the wind is proportional to the kinetic energy of the wind and is given by

$$P_{available} = \frac{1}{2} \rho A v_w^3 \qquad (A.1)$$

where ρ is the density of the air, A is the area swept by the blades of the windmill and v_w is the velocity of the wind. All units are in mks. Tip speed is the product of windmill shaftspeed, ω_s, and windmill radius, R. The velocity ratio is the ratio of windmill tip speed to wind velocity, $\omega_s R/v_w$. The power ratio, c_p, is the ratio of wind power extraction, to the total power available in the wind. For a given fixed blade windmill, c_p is a function of the velocity ratio.

Using c_p, wind power extraction can be related to wind power.

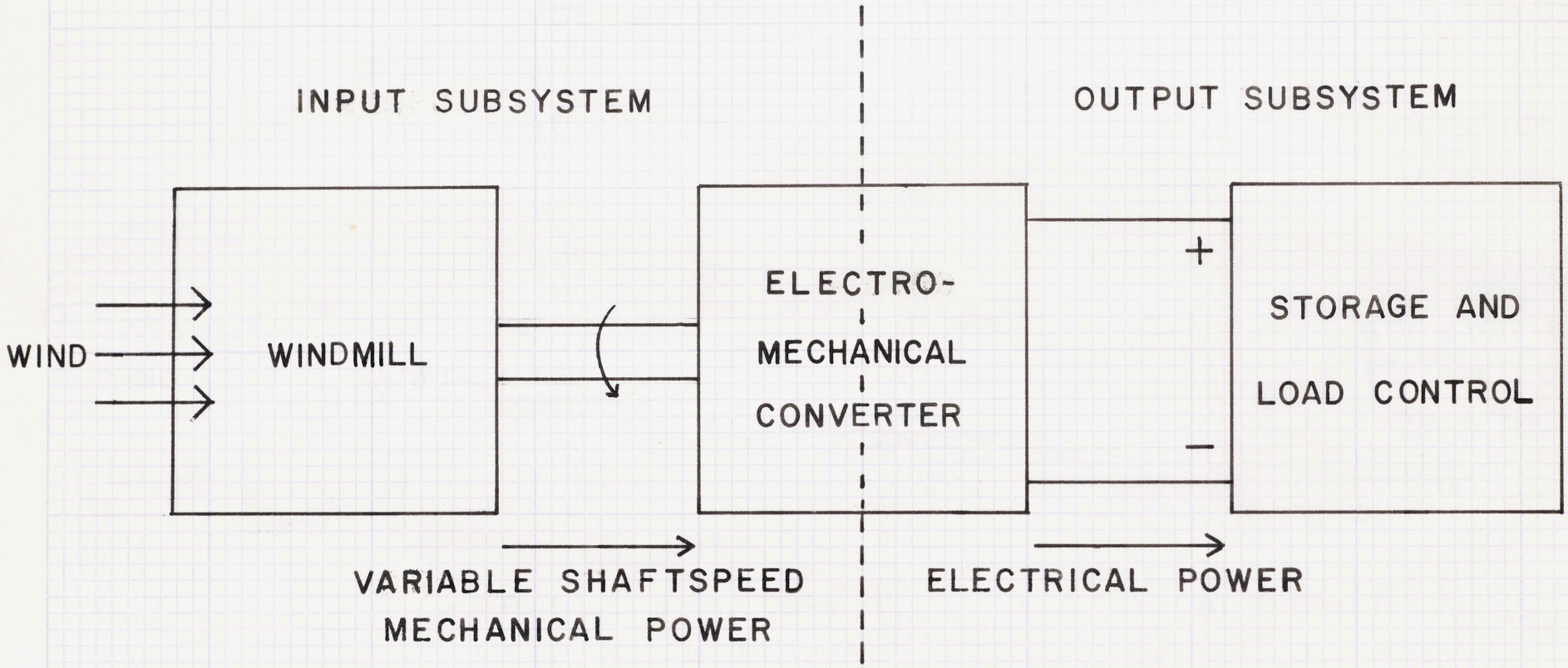

Figure A.1 Simplified Block Diagram of Wind Energy Conversion and Storage System

$$\text{Power Extracted} = \left[c_p \left(\frac{\omega_s R}{v_w}\right) \cdot \frac{1}{2} \rho A v_w^3\right] \qquad \text{(A.2)}$$

APPENDIX B

PHYSICAL SCALE MODEL SYSTEM DESIGN

The purpose of this appendix is to apply the windmill power system design procedure, introduced in Section II.1, to a physical scale model system. This procedure involves three steps. The first step deals with the choice of base quantities for the system. This choice is made in accordance with rated generator quantities. The second step involves the construction of a compatible battery bank which can accept the required power during rated system operation. The final step in windmill power system design is in the actual design of the windmill. During rated operation, this windmill must supply enough power to maintain both rated generator output and power losses associated with the coupled windmill-generator.

B.1 Generator Characteristics and the Choice of Base Quantities for the Windmill Power System

The generator employed in the physical scale model simulation of the windmill power system is a single-phase Long Island Alternator. The nameplate ratings and specifications of this machine are listed in Table B.1.

From the discussion of the battery charging circuit model in Section I.2.c, the generator armature current, i_t in Figure 4 (Section I.2.c), was shown to represent the fundamental component of the actual armature current waveform. As described, only this component contributes to the power output of the machine. However, since the generator armature winding is rated at 17.4A rms, from

TABLE B.1

GENERATOR RATINGS AND SPECIFICATIONS

Rated Shaftspeed	3450 rpm
Rated Armature Voltage	115V rms
Armature Voltage Frequency (at Rated Shaftspeed)	400Hz
Rated Armature Current	17.4A rms
Rated Power Output	2kw
Armature Winding Resistance (at 25°C)	0.25Ω
Field Winding Resistance (at 25°C)	150Ω
Field Current Required to Produce Rated Open-Circuit Armature Voltage at Rated Shaftspeed	0.35A dc

Table B.1, the rms value of the actual square-wave armature current, and not the rms value of i_t, must be maintained below this rating. Thus, the rating of i_t in Figure 4 is $r \cdot 17.4 = 15.6$A rms, where $r = 2\sqrt{2}/\pi$ (the rms value of the fundamental component of a unit amplitude square wave). This means that the electrical power rating of the generator is also reduced by the factor r to approximately 1.8kw.

The decision was made to return the power rating of the generator to 2kw. This was achieved by increasing both the shaftspeed and field current excitation of the machine until the new open-circuit voltage of 128v rms, i.e., 2kw/15.6A rms, was attained. This voltage, as well as the shaftspeed and field current required to produce this voltage, i.e., 3600rpm and 0.4A dc, were chosen as the generator base quantities. These base quantities that recharacterize rated generator operation are summarized in Table B.2. These quantities are the desired operating

levels of the generator at rated wind speed. Generator operation at these levels, as opposed to the ratings listed in Table B.1, do not physically compromise generator performance.

TABLE B.2

GENERATOR BASE QUANTITIES

Base Shaftspeed (ω_{sb})	3600rpm (377sec^{-1})
Base Armature Voltage (V_{tb})	128V rms
Base Armature Current (I_{tb})	15.6A rms
Base Power (P_b)	2kw
Base Field Current (I_{fb})	0.40A dc
Base Field Flux (ϕ_b)	0.34V-sec

The field flux level in the generator is calculated by taking the quotient of open-circuit armature voltage and shaftspeed (see Eq. 4 and related discussion). The base field flux in Table B.2 is calculated via this method by using base armature voltage and base shaftspeed.

Figure B.1 shows the magnetization curve and short-circuit characteristics for the generator. The axes of the figure are marked in per unit with base quantities previously defined in Table B.2. This curve was measured at 1 per-unit shaftspeed thus the vertical axis represents either the generator open-circuit armature voltage or the flux level within the generator. The measured variation in open-circuit voltage due to hysteresis effects in the generator iron was

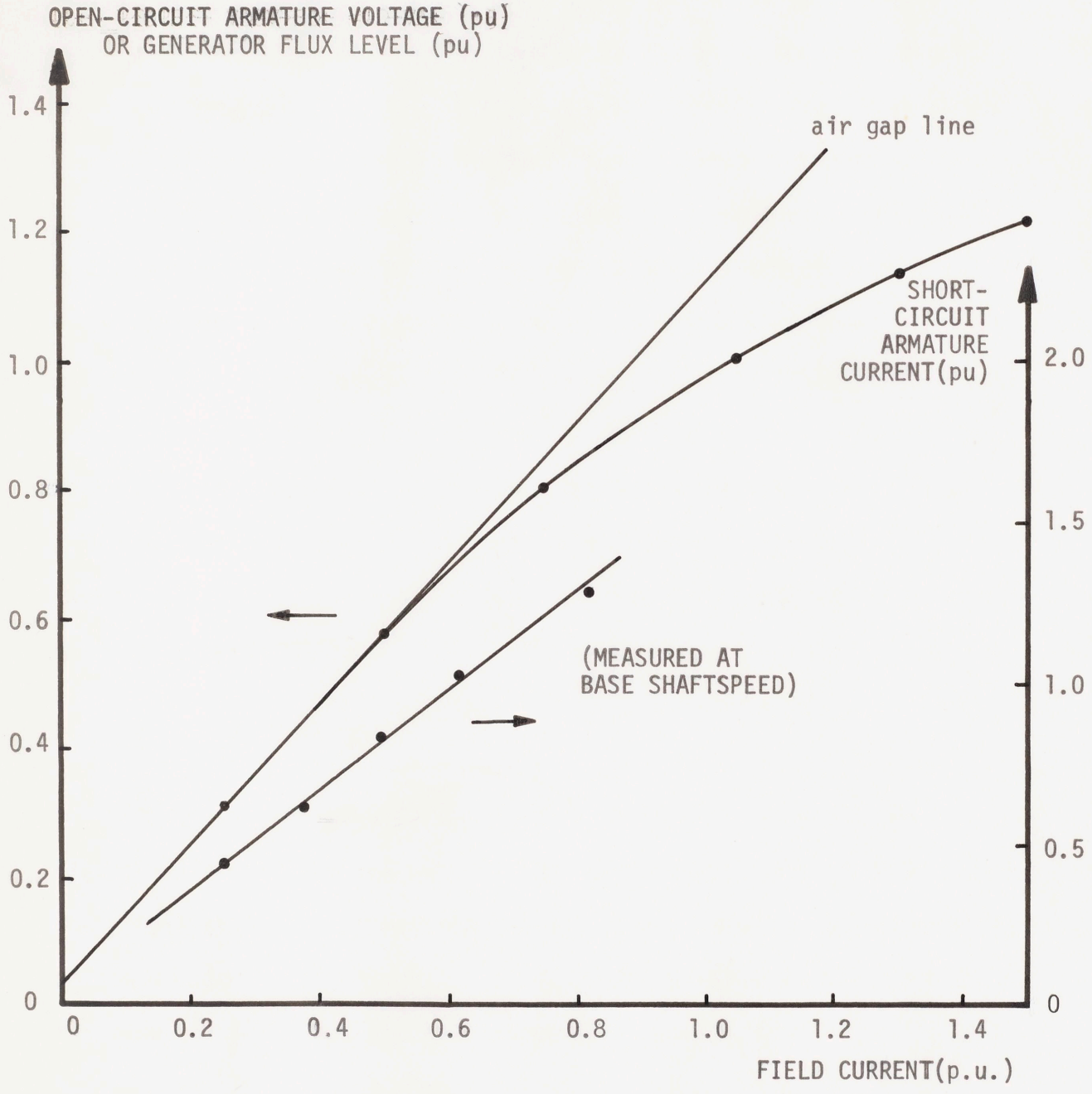

Figure B.1 Generator Open-Circuit Armature Voltage and Short-Circuit Armature Current as a Function of Field Excitation

no more than ± 0.04 per unit over the entire field current range. Also the finite flux at zero field current is due to residual magnetism in the machine iron. From Figure B.1, the internal inductance, L_x, of the machine armature winding can be calculated as the quotient of the field currents necessary to produce base armature current and base armature voltage. Due to magnetic saturation effects, this inductance varies as a function of generator field flux level. Figure B.2 plots the variation in L_x as a function of field flux. Also marked in Figure B.2 is the value of L_x under rated load conditions, obtained from measuring the field excitation under these conditions.

Now that desired generator operation at rated wind speed is known, i.e., at those levels listed in Table B.2, design of a compatible battery load and windmill can be effected.

B.2 Battery Bank Design

Due to the transformer turns ratio modeled in Section I.2.c, Figure 4, the voltage and current base quantities on the dc side of the charging circuit are transformed by a factor r from the base quantities on the ac side of the vircuit. Thus, on the dc side of the circuit, the base voltage, V_{bb}, and base current, I_{bb}, are

$$V_{bb} = r \cdot V_{tb} = 115V \text{ dc}$$

$$I_{bb} = \frac{I_{tb}}{r} = 17.4A \text{ dc} \qquad (B.1)$$

where $r = 2\sqrt{2}/\pi$ and V_{tb} and I_{tb} are from Table C.2.

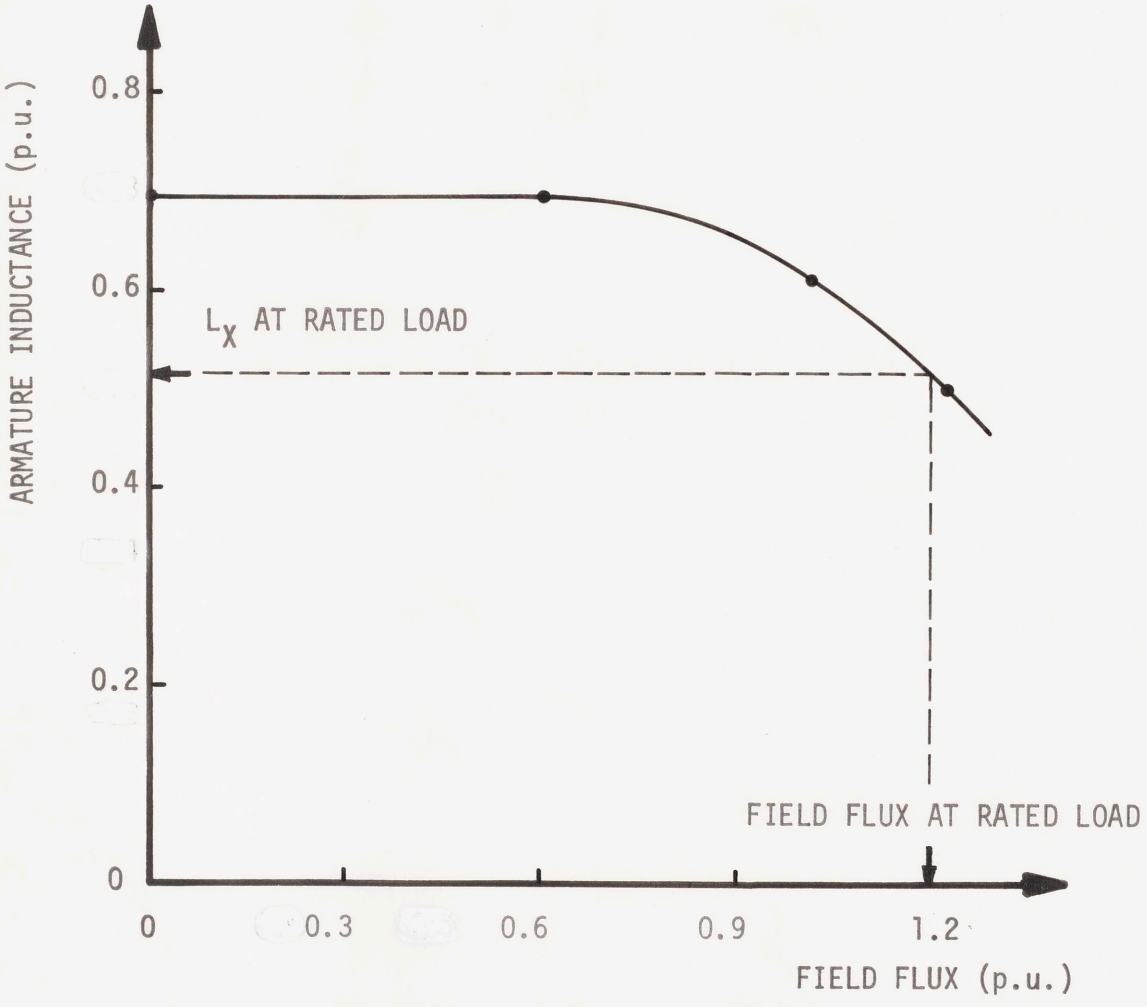

Figure B.2 Generator Armature Inductance as a Function of Field Excitation

From Section II.1, a relationship was constructed that links the choice of nominal battery bank parameters to rated generator quantities and charging circuit parameters. This relationship is given by Eq. 21. The quantity v_d in Eq. 21 is the voltage drop across a single rectifier in the charging circuit, about 1 volt for the rectifiers used in the physical scale model system. Thus, in per unit,

$$4v_d = \frac{4V}{V_{bb}} = \frac{4V}{115V} \simeq 0.03 \text{ p.u.} \tag{B.2}$$

The quantity R_s in Eq. 21 is the resistance associated with the smoothing choke inductor in the charging circuit. For the inductor used, this resistance is approximately 0.22Ω. Thus, in per unit,

$$R_s = \frac{0.22\Omega \cdot I_{bb}}{V_{bb}} = \frac{0.22\Omega \cdot 17.4A}{115V} \simeq 0.03 \text{ p.u.} \tag{B.3}$$

Replacing Eqs. B.2 and B.3 into Eq. 21 results in

$$V_{BN(NOM)} + R_{BN(NOM)} = 0.94 \text{ p.u.} \tag{B.4}$$

The choice of nominal battery bank parameters, such that they satisfy Eq. B.4, is accomplished in Appendix C.

B.3 Windmill Design

During rated system operation at rated wind speed, the windmill must supply enough power to maintain both rated generator output and power losses associated with the coupled windmill-generator. A

windmill design that is capable of supplying this power requirement was described in Section II.1. The characteristics of this windmill are given by Eq. 29 where P_{RW} is a function of both the windmill and generator loss coefficients and the internal generator impedances. P_{RW} is given by Eq. 26 (Section II.1).

The calculation of the loss coefficients C_{w1} and C_{w2} in Eq. 26 is dependent on the characteristics of the windmill that drives the generator. Since a dc motor is used to simulate the power-speed characteristics of a windmill, these two loss coefficients depend not only on mechanical losses associated with the motor shaft but also on magnetic-core losses in the machine iron. An outline of the procedure involved for windmill simulation as well as the measurement of the losses associated with this windmill simulator are described in Appendix D. In that appendix values for C_{w1} and C_{w2} are determined. Thus, from Eq. D.14

$$C_{w1} + C_{w2} = 0.215 \tag{B.5}$$

In determining the values for the remaining parameters in Eq. 26, measurements must be effected on the generator. These measurements, which determine all the power losses associated with the generator, are described in Appendix E. In that appendix, the mechanical loss coefficients, C_{g1} and C_{g2}, as well as the magnetic-core loss coefficients, C_e and C_h are determined for the generator. Also the equivalent stray-loss resistance, R_{ST}, is estimated. The results yield

$$C_{g1} + C_{g2} = 0.07$$

$$C_e + C_h = 0.055 \qquad \text{(B.6)}$$

$$R_{ST}(\omega_s = 1) = 0.03$$

where Eqs. E.2, E.4 and E.5 have been used.

The value of the effective resistance of the generator armature winding, R'_{eff}, is given by Eq. 14 (Section I.2.d) where R_a is the generator armature resistance and $r = 2\sqrt{2}/\pi$ in the case of a single-phase generator. The generator armature resistance is obtained from Table B.1 and can be expressed in per unit using the base quantities in Table B.2. This resistance is

$$R_a \simeq 0.03 \qquad \text{(B.7)}$$

Thus

$$R'_{eff} = \frac{R_a + R_{ST}}{r}$$

$$\simeq \frac{0.03 + 0.03}{\frac{2\sqrt{2}}{\pi}}$$

$$R'_{eff} \simeq 0.07 \qquad \text{(B.8)}$$

where Eqs. B.6 and B.7 have been used.

All information is now available in determining P_{RW} in Eq. 26. Substituting Eqs. B.5, B.6, B.7 and B.8 into Eq. 26 and using

Figure B.2 to determine the internal generator inductance, L_x, at rated load yields

$$P_{RW} = 1 + (0.055)[(1 + 0.07)^2 + (0.5)^2] + 0.07$$
$$+ 0.07 + 0.215$$
$$P_{RW} \simeq 1.43 \text{ p.u.} \qquad \text{(B.9)}$$

Thus the windmill necessary to supply rated generator output at both rated wind velocity and rated system shaftspeed is the windmill with the power-extraction characteristic

$$P_{ext} = 1.43 v_w (2 v_w \omega_s - \omega_s^2) \qquad \text{(B.10)}$$

where Eq. B.9 has been substituted into Eq. 29. Equation B.10 is plotted in Figure B.3 for three values of v_w.

A piece of information needed in performing the digital computer simulation of the windmill power system, as presented in Section II.3, is the H constant $(\frac{1}{2} J \frac{\omega_{s(rated)}^2}{P_{t(rated)}})$ of the coupled windmill-generator system. The H constant of the system is calculated by measuring the shaftspeed profile as the coupled windmill-generator slows down from rated shaftspeed under the influences of mechanical power losses alone. The speed profile can then be analytically approximated and weighted by the mechanical power loss equations for the system (sum of Eqs. 3 and 11 in Chapter I). The resulting function is then integrated

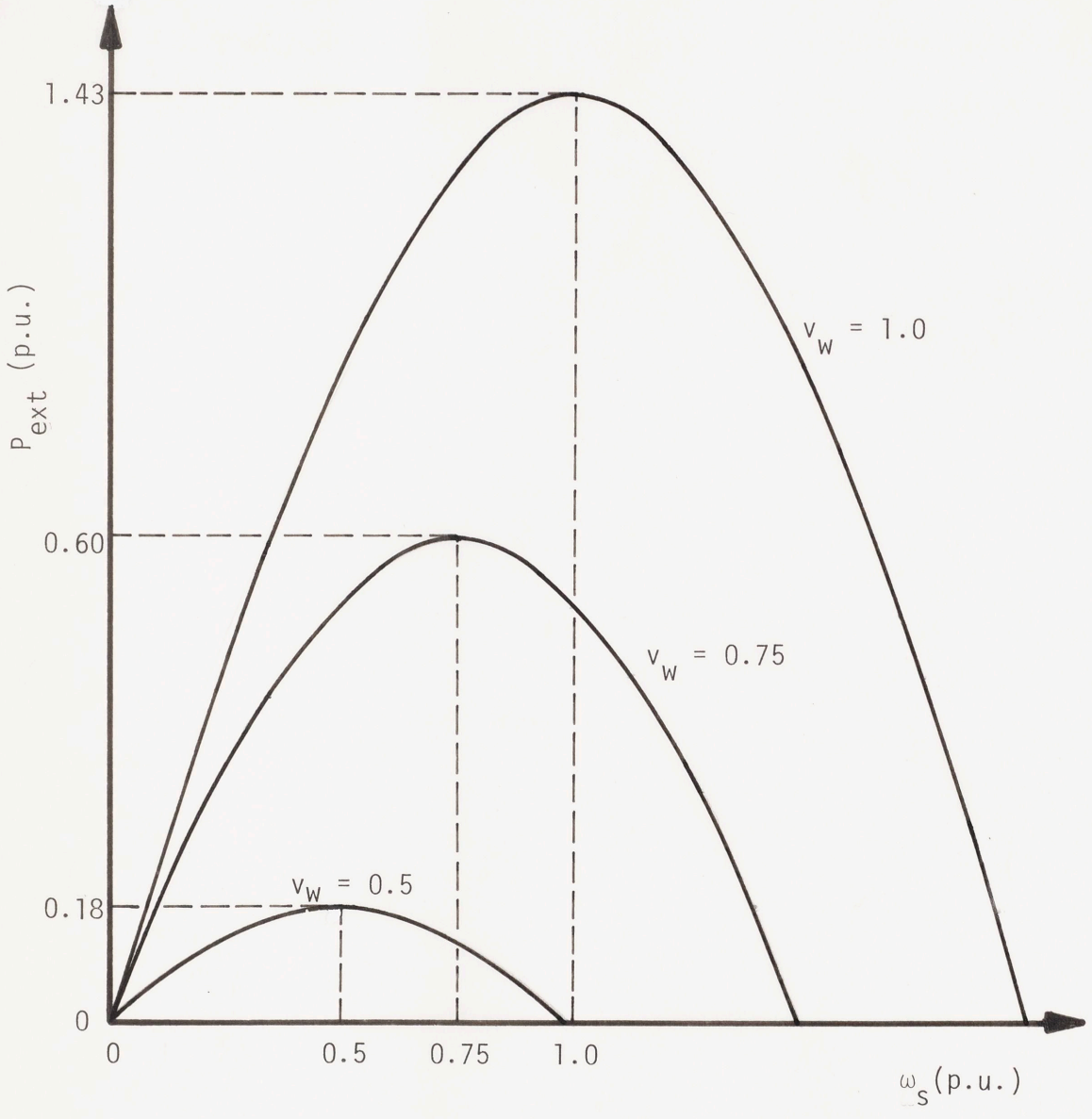

Figure B.3 Wind-Power Extraction Characteristic Designed for Physical Scale Model System.

over time to determine the kinetic energy of the shaft at rated shaft-speed. The quotient of this result and the base generator power then determines the H constant for the system. By carrying out the above procedure the H constant of the physical model system was determined to be

$$H = 2 \text{ seconds} \qquad \text{(B.11)}$$

APPENDIX C

BATTERY BANK DESCRIPTION AND CHARACTERISTICS

The purpose of this appendix is to choose nominal battery bank parameters, i.e., internal voltage and resistance, such that Eq. B.4 is satisfied.

The resulting battery bank employed in the windmill power system consists of sixteen 6V batteries connected in series. These batteries have a measured capacity of 60 ampere-hours based on a 12-hour rate. For the model simulations described in the main text, the battery bank is separated into two sections of eight batteries.

Detailed measurements were made of the internal voltage and resistance of one of the battery sections as a function of battery state-of-charge. These measurements were taken as a source voltage was instantaneously impressed onto the battery section. However, after every period of discharge, the batteries were allowed to recharge at a nominal rate for a short period of time (a few minutes) prior to making new measurements. This was to allow the electrochemical reactions in the cells to settle to a quasi-equilibrium associated with battery charging conditions.

The results of the internal battery parameter measurements are summarized in Table C.1. The resistance measurements are approximate, ±10 to 20%, the worst case being for the smaller resistance values.

TABLE C.1

INTERNAL BATTERY PARAMETER MEASUREMENTS

Battery Section State-of-Charge	Open-Circuit Voltage (Volts)	Charging Current (amps)	Measured Internal Resistance (ohms)
Fully Charged	56 ± 0.5	3.5	0.9
		7.0	0.5
		10.5	0.5
		12.5	0.5
5 Amps Out for 3 Hours	52.5 ± 0.5	4.0	0.1
		7.5	0.1
		11.0	0.1
		15.0	0.1
5 Amps Out for 6 Hours	51 ± 0.5	"	0.1
5 Amps Out for 9 Hours	50 ± 0.5	"	0.1
5 Amps Out for 12 Hours	48.5 ± 1.5	"	0.2

During the last hour of discharge, the internal voltage of the batteries falls drastically. However, this voltage returns rapidly to the level indicated in Table C.1, i.e., 48.5V, after only a few minutes of battery recharging. Thus, the assumption is made that the lowest state of battery charge is represented by the last readings in Table C.1

Since the voltage and resistance measurements listed in Table C.1 are only for one battery section, these values must be doubled if the full battery bank is taken into account. Per-unitizing

these parameter values for the full bank and relating them to the state-of-charge variable, soc, results in the values indicated in Table C.2. Base quantities are given in Eq. B.21.

TABLE C.2

PER-UNIT BATTERY BANK PARAMETERS AS A FUNCTION OF BATTERY STATE-OF-CHARGE

State-of-Charge (soc)	Internal Voltage (p.u.)	Internal Resistance (p.u.)
1.0	0.97	0.27 (Low Charging Current)
		0.15 (Intermediate and High Charging Current)
0.75	0.92	0.03
0.5	0.89	0.03
0.25	0.87	0.03
0	0.84	0.06

As seen from Table C.2, "soc" varies from 0 to 1 depending on the state-of-charge, i.e., fully discharged to fully charged, of the battery bank. Also seen from Table C.2 is that Eq. B.4 is satisfied for a battery state of charge somewhere between $0.5 \leq \text{soc} \leq 0.75$. Thus, the nominal values for the battery bank parameters are chosen to be

$$V_{BN(NOM)} = 0.91 \tag{C.1}$$

$$R_{BN(NOM)} = 0.03$$

Using Table C.2 and Eq. C.1, the variation of internal battery parameters away from their nominal values can be expressed in the manner shown in Eq. 36 (Section II.3),* where ε_1 and ε_2 are related to the battery state-of-charge variable, soc. Figures C.1(a) and C.1(b) show these calculated relationships for ε_1(soc) and ε_2(soc). From these figures, nominal battery state-of-charge occurs where $\varepsilon_1 = \varepsilon_2 = 0$, i.e., where soc = 0.7.

The modeling of the battery bank is now complete. Equation C.1 models the nominal values of the battery bank parameters and Figures C.1(a) and (b) show the variation in these parameters, for one of the two battery sections, as a function of battery state-of-charge.

*Remember that $V_{BS(NOM)} = \frac{V_{BN(NOM)}}{2}$ and $R_{BS(NOM)} = \frac{R_{BN(NOM)}}{2}$ since only two battery sections make up the battery bank in this power system.

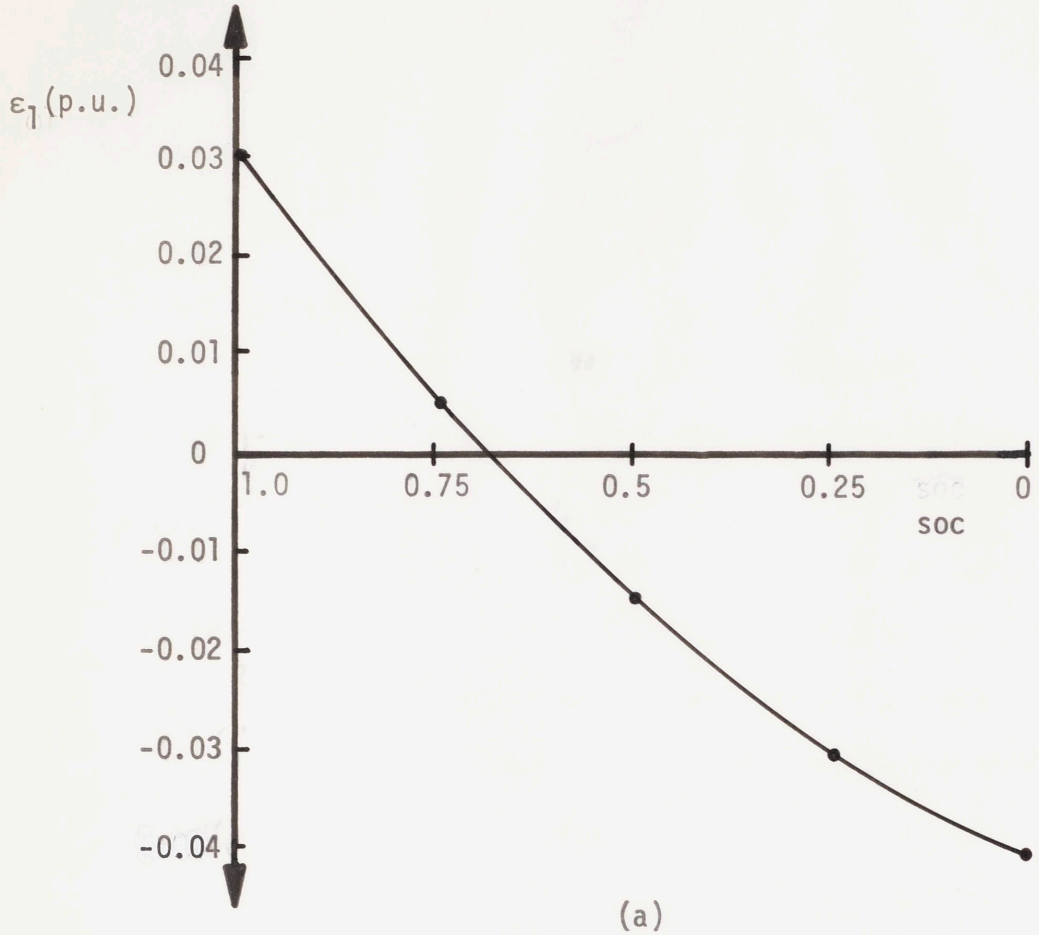

(a)

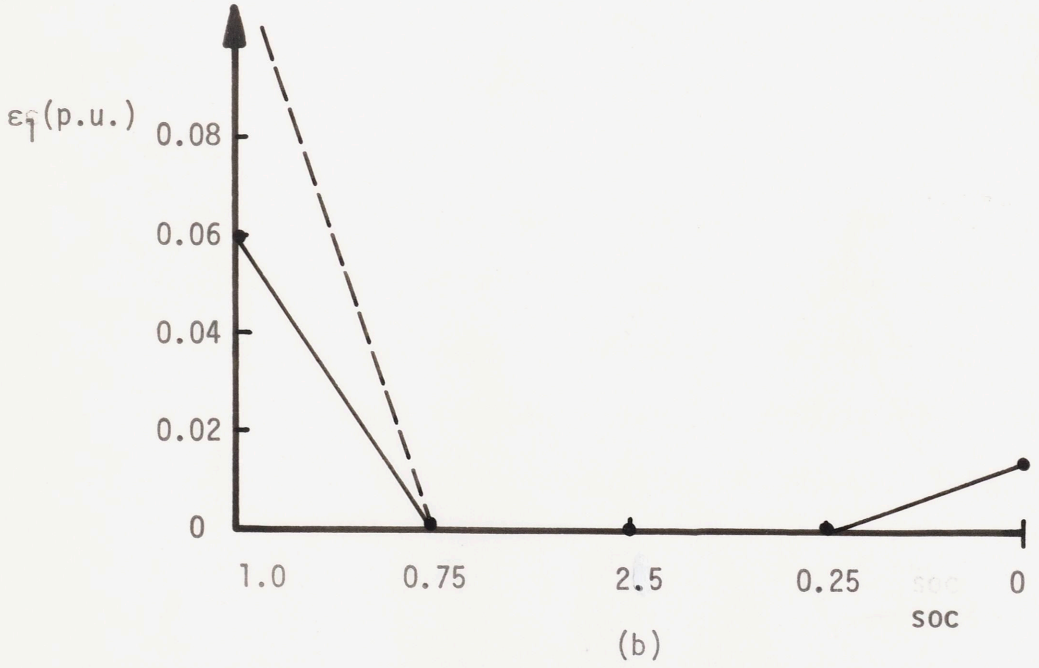

(b)

Figure C.1 Variation in Battery Bank Parameters, Away from Nominal Values, as a Function of Battery State-of-Charge

APPENDIX D

WINDMILL SIMULATION AND SIMULATOR CHARACTERISTICS

D.1 Windmill Simulation

This section describes the simulation of the windmill power-speed characteristics by a dc motor. A dc motor is chosen because of its ease of control over a wide range of operating speeds.

The objective of this windmill simulation is to produce the parabolic windmill characteristic shown in Fig. B.3 and described by Eq. 29 in Section II.1. In the simulation, the air gap power in the motor will model the power extracted from the wind by the windmill. Thus the power input to the motor must be related to a simulated wind speed variable.

The schematic representation of a separately excited dc motor is shown in Fig. D.1. All circuit inductances in the motor model have been removed since only steady-state motor operation is considered. Table D.1 describes the variables.

The field current excitation in the motor produces a magnetic flux in the air-gap of the machine. An emf, or speed voltage, is produced by the rotating armature coils cutting this magnetic field. In per-unit, this speed voltage is given by the product of per-unit motor field flux level and per-unit motor shaftspeed. Thus,

$$e_a = \phi_M \omega_{sM} \tag{D.1}$$

From Fig. D.1, the equation describing the armature circuit is

$$v_a = R_a i_a + e_a$$

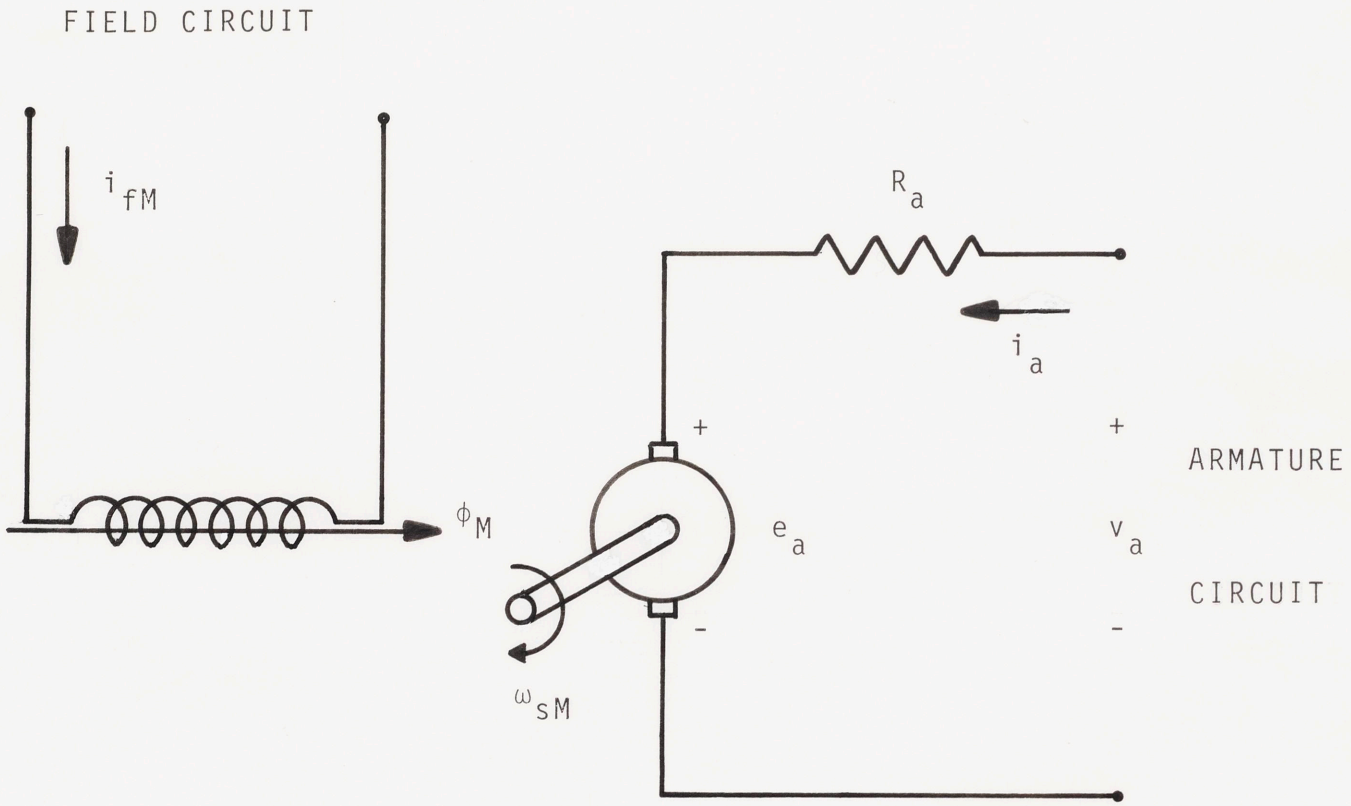

Figure D.1 DC Motor Circuit Model.

TABLE D.1

MOTOR PARAMETERS

R_a - Armature Circuit Resistance (winding and added external circuit resistance)

v_a - Armature Circuit Terminal Voltage

i_a - Armature Circuit Current

i_{fM} - Field Circuit Current

ω_{sM} - Shaftspeed

e_a - Speed Voltage or Open-Circuit Armature Voltage

Rearranging $i_a = \dfrac{v_a - e_a}{R_a}$

and using Eq. D.1

$$i_a = \frac{v_a - \phi_M \omega_{sM}}{R_a} \tag{D.2}$$

From the model of Fig. D.1 the air gap power is the product of armature current and speed voltage. Thus,

$$\text{Air Gap Power} \equiv P_M = e_a i_a$$

$$= \frac{(\phi_M)^2}{R_a} \left(\frac{v_a}{\phi_M} \omega_{sM} - \omega_{sM}^2\right) \tag{D.3}$$

where both Eqs. D.1 and D.2 have been used. The motor power-speed

characteristic described by Eq. D.3 exhibits the same shaftspeed behavior as the desired windmill power extraction characteristic given by Eq. 29 (Section II.1). These two equations become equivalent if the following assignment is made:

$$v_a(\text{p.u.}) = 2(P_{RW}R_a)^{1/2} \cdot v_w^{3/2} \tag{D.4}$$

$$\phi_M(\text{p.u.}) = (P_{RW}R_a)^{1/2} \cdot v_w^{1/2} \tag{D.5}$$

where v_w is now the simulated wind speed variable and P_{RW} is the peak value, in per unit, of the wind power extraction characteristic for a wind speed of 1 per unit. By way of the simulation, P_{RW} is now also the peak value of the motor air-gap power at rated, i.e., 1 per unit, simulated wind velocity.

If the terminal voltage, v_a, and motor field flux level, ϕ_M, are controlled with respect to simulated wind speed, v_w, in the manners described in Eqs. D.4 and D.5, then the dc motor simulates the power-speed characteristic of a windmill. Also, if the assignment, $R_a=1/P_{RW}$, is made then the windmill simulation equations become

$$v_a(\text{p.u.}) = 2v_w^{3/2} \tag{D.6}$$

$$\phi_M(\text{p.u.}) = v_w^{1/2} \tag{D.7}$$

$$R_a(\text{p.u.}) = 1/P_{RW} \tag{D.8}$$

The constraint imposed by Eq. D.8, i.e., implementing the equivalent of this resistance in the motor armature winding, guarantees that at rated simulated wind speed, i.e., v_w = 1 per unit, the dc

machine's flux level is at its base value, i.e., $\phi_M = 1$ from Eq. D.7. The choice of base quantities for the motor used in the simulation is discussed in the following section.

D.2 Motor Specifications and Choice of Base Quantities

The motor used in the windmill simulation is a Long Island dc motor. The motor's ratings are listed in Table D.2.

TABLE D.2

MOTOR RATINGS

Rated Armature Voltage	120V dc
Rated Armature Current	30A dc
Rated Shaftspeed	3600rpm
Rated Power	3.5kw
Field Current Necessary to Produce Rated Armature Voltage at Rated Shaftspeed	1.05A dc

Three base assignments are necessary to completely define a per-unit system for the motor. However, since the per-unit power, P_{RW}, is already expressed on the generator power base, the assignments in Eqs. D.4 and D.5 are not valid unless the base powers for the motor and generator are equal. Thus the power base for the motor is chosen equal to the generator base power. The remaining two base assignments are made in terms of motor shaftspeed and voltage. The base motor shaftspeed is chosen to be the same as the generator base,

i.e., 3600rpm. The base voltage is chosen to be the machine rating, or 120V dc. From these three assignments, i.e., power, voltage and speed, the remainder of the motor base quantities can be calculated. These base quantities are shown in Table D.3.

TABLE D.3

MOTOR BASE QUANTITIES

Base Power	2kw
Base Armature Voltage	120V dc
Base Shaftspeed	3600rpm
Base Armature Current	16.7A dc
Base Field Flux	0.32V-sec
Base Field Current	1.05A dc
Base Armature Resistance	7.2Ω

The base field flux in Table D.3 is the quotient of base armature voltage and base shaftspeed. The base field current is that field current necessary to produce this base field flux or, equivalently, to produce base armature voltage at base shaftspeed. The base armature current is simply the quotient of base power and base armature voltage. Finally, the base armature resistance is the quotient of the square of the base armature voltage and base power.

Now that base quantities have been chosen, the implementation

of Eqs. D.6 to D.8 is possible. From Eq. D.6 the terminal voltage, v_a, is driven in proportion to wind velocity to the three-halves power. At rated wind velocity v_a is 2 per unit, or 240V from Table D.3. From Eq. D.7 the field flux level is driven proportional to the square root of the simulated wind velocity and at rated wind speed this flux is at its base, or rated, value, i.e. 0.32V-sec from Table D.3. If the per-unit value of R_a, i.e., the lumped sum of the interval armature winding resistance and an added external resistor in series with the winding, is chosen according to Eq. D.8, then the power across the air gap of the motor, Eq. D.3, as a function of simulated wind speed, is

$$P_M = P_{RW} v_w (2 v_w \omega_{sM} - \omega_{sM}^2) \qquad (D.9)$$

where Eqs. D.6 to D.8 have been substituted into Eq. D.3. Equation D.9 is precisely the desired parabolic windmill characteristic shown in Fig. B.3.

The circuit implementation of Eqs. D.6 through D.8 on the dc motor has been previously realized (see Appendix C.9 of Reference 1) and is not reproduced here.

D.3 Motor Power Loss Measurements

The purpose of this section is to estimate motor power losses and to express these losses in terms of the loss mechanisms modeled for an actual windmill. Section I.1.b described the loss mechanisms associated with a windmill. Equation 3 in that section models these losses. The objective now is to find expressions for the windmill

loss coefficients, C_{w1} and C_{w2}, from the loss measurements made on the windmill simulator, i.e., dc motor.

The dc magnetization curve for the motor is shown in Fig. D.2. This curve is needed to relate motor field current excitation to the flux level within the machine. The axis of the figure are marked in per unit, based on the values in Table D.3. The per-unit field flux level is determined by taking the quotient of the measured per-unit open-circuit armature voltage and the per-unit shaftspeed at which the voltage measurement was made. Hysteresis effects produced a variation in this open-circuit voltage of no more than 0.03 per unit over the entire measured voltage range.

Detailed loss measurements were made for the dc motor. However, unlike a windmill, a dc machine exhibits not only mechanical power losses but also magnetic-core power losses, i.e. hysteresis and eddy current losses. Other sources of power loss, such as stray losses, are considered negligible for a dc machine and are thus ignored for this analysis. I^2R power losses in the motor armature winding are irrelevant in this case because, as previously discussed, the motor armature resistance has been lumped into the resistance added externally to the motor.

A no-load torque-speed curve was measured for the dc machine. These measurements were made at two different motor field excitations. The results are shown in Fig. D.3; the solid line approximates the measured values; the dashed line will be discussed later. Per-unit torque, plotted on the vertical axis of the figure, is defined as the quotient of per-unit power into the unloaded machine and the per-unit

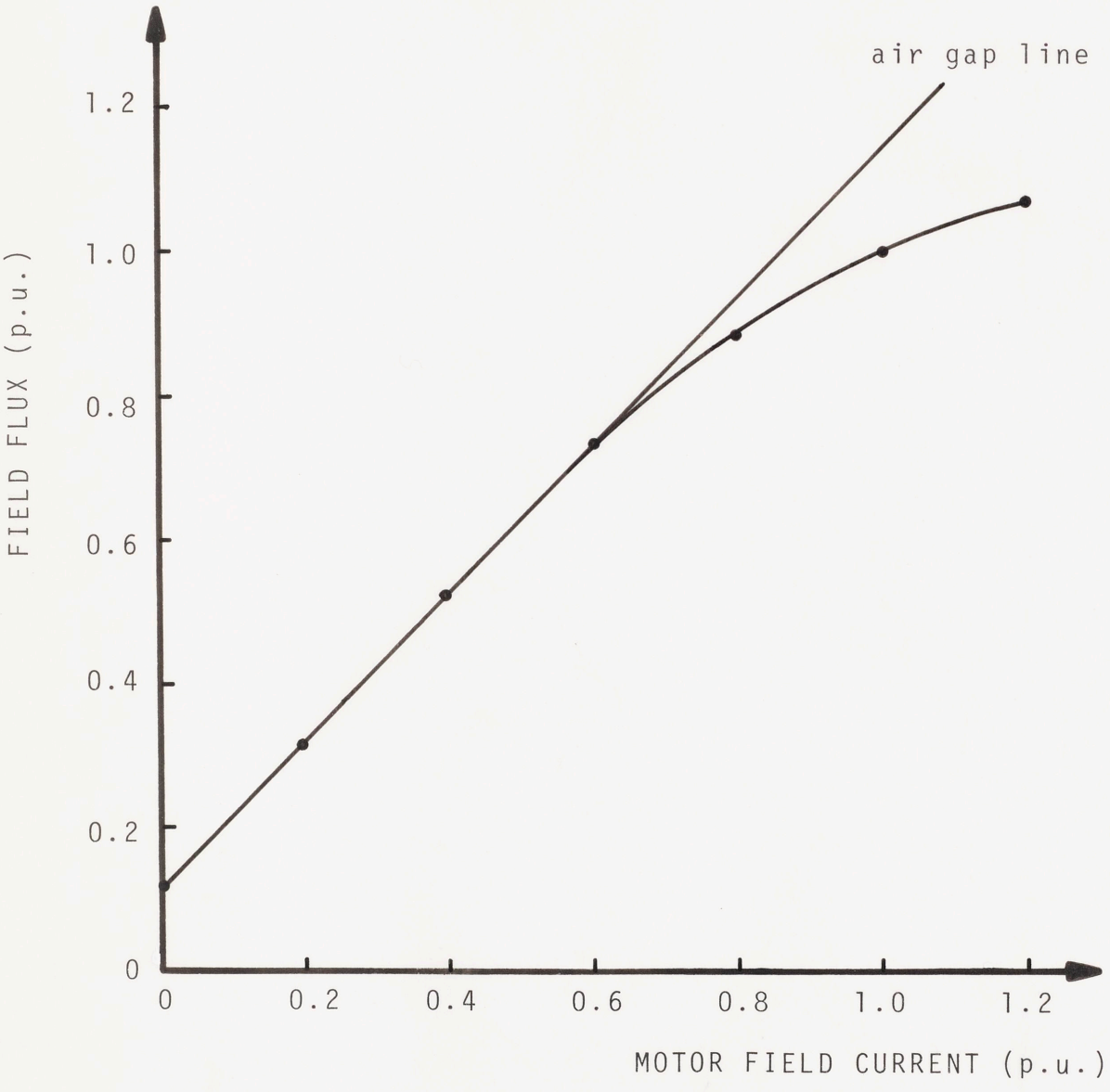

Figure D.2 DC Motor Magnetization Curve.

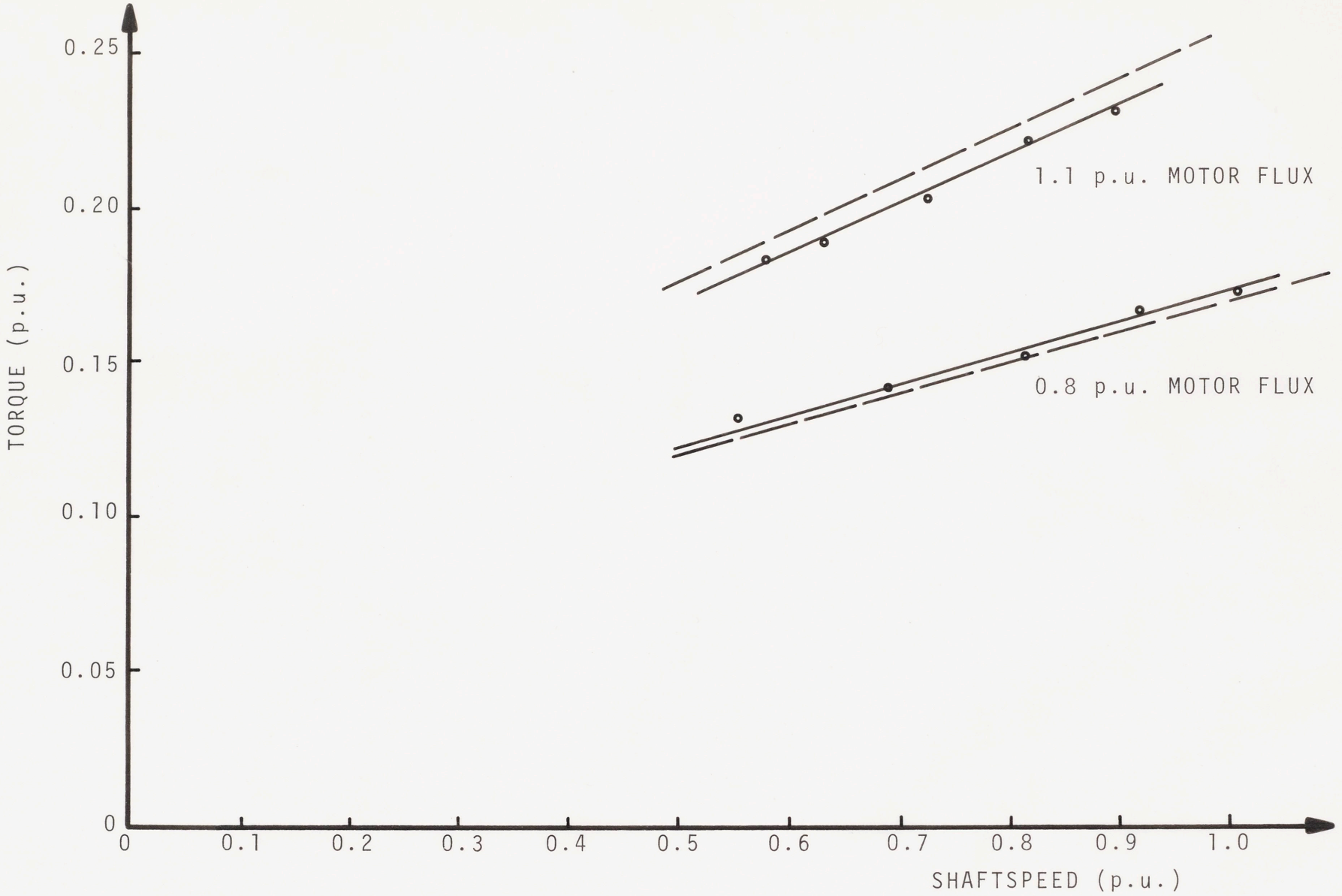

Figure D.3 No-Load Motor Torque-Speed Characteristics

shaftspeed at which the measurement was taken. Since the measured torque-speed curve in Fig. D.3 is linear, the mechanical power losses of the machine, i.e., the product of this no-load torque and shaft-speed, depend on shaftspeed in the predicted linear and squared manner as described by Eq. 3.

Figure D.4 shows a linear relationship between no-load power losses and the square of motor field flux level at constant shaftspeed. The two plots shown are for measurements at two different values of shaftspeed. Note that this linear relationship in Fig. D.4 is the behavior predicted by the magnetic-core power loss model of Section I.2.d (Eqs. 12 and 13).

From Figs. D.3 and D.4 the loss coefficients for the dc motor can be determined by relating the measured results to the power loss models developed in Chapter I. As shown in Chapter I, these no-load losses are the sum of three power-loss components

$$\begin{aligned}\text{Motor Power Losses} \equiv P_{LM} &= \text{Mechanical Power Losses} \\ &+ \text{Hysteresis Power Losses} + \text{Eddy-Current Power Losses} \\ &= C_1\phi_M^2\omega_{sM}^2 + C_2\phi_M^2\omega_{sM}^2 + C_3\omega_{sM} + C_4\omega_{sM}^2 \qquad \text{(D.10)}\end{aligned}$$

where C_1 through C_4 are the power loss coefficients for the dc motor. (Note that C_1 through C_4 are per-unit quantities.)

From the equations of the solid lines in Figs. D.2 and D.3, C_1 through C_4 can be estimated. Sufficient information exists in each figure to independently determine the values of these loss coefficients. Calculating these constants from each figure and averaging the two

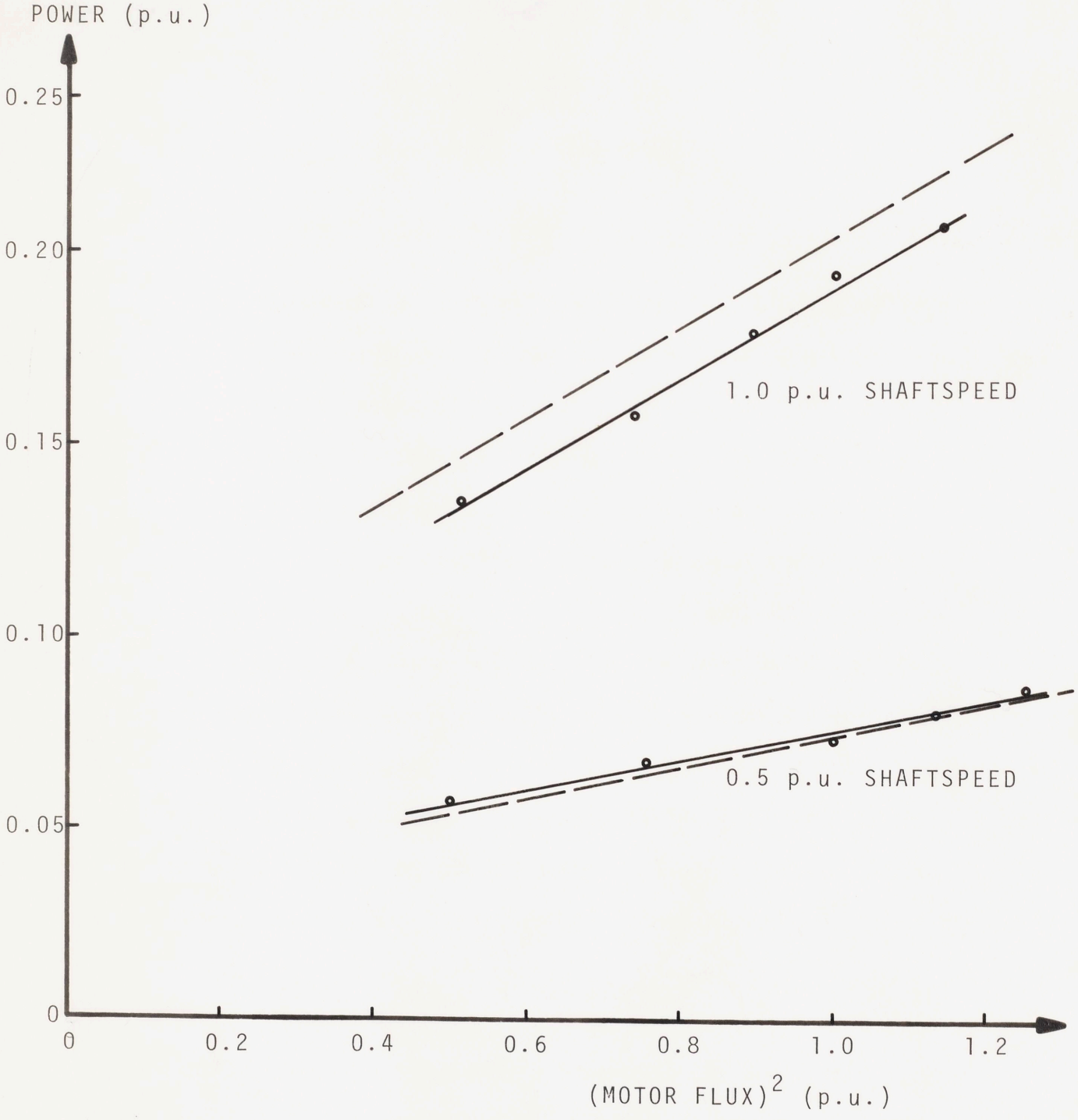

Figure D.4 No-Load Motor Losses as a Function of the Square of Motor Field Flux Level.

results yields the following values for C_1 through C_4:

$$C_1 = 0.09;\ C_2 = 0.04;\ C_3 = 0.045;\ C_4 = 0.04 \qquad (D.11)$$

Substituting Eq. D.11 into Eq. D.10 yields

$$P_{LM} = (0.045+0.04\phi_M^2)\omega_{sM} + (0.04+0.09\phi_M^2)\omega_{sM}^2 \qquad (D.12)$$

Since the values of the coefficients in Eq. D.12 are the average value of two results, this equation may not correspond exactly to the solid line joining the measured points in Figs. D.2 and D.3. Thus, Eq. D.12 has been plotted in these figures (dashed line) for the same conditions that resulted in the measured loss curves. The discrepancy between the measured results and the model described by Eq. D.12 is no more than 0.014 p.u. in the worst case, i.e., measurement made at 1 p.u. shaftspeed in Fig. D.4. However, the discrepancy between the remaining measured results in Figs. D.3 and D.4 and the model equation is negligible.

In the windmill simulation the motor's field flux level is excited as a function of the simulated wind velocity; Eq. D.7 shows the relation. Substituting Eq. D.7 into Eq. D.12 yield

$$P_{LM} = (0.045+0.04v_w)\omega_{sM} + (0.04+0.09v_w)\omega_{sM}^2 \qquad (D.13)$$

Because the motor is simulating a windmill, the power loss expressed by Eq. D.13 is analogous to the windmill mechanical power losses expressed in Eq. 3 (Section I.1.b). Since the base shaftspeeds of both the motor and generator are the same, $\omega_{sM} = \omega_s$ and thus the coefficients in Eq. 3 can be directly related to the

bracketed terms in Eq. D.13:

$$C_{w1} = 0.045 + 0.04v_w$$
$$C_{w2} = 0.04 + 0.09v_w \qquad \text{(D.14)}$$

Equation D.14 shows that the loss coefficients of the simulated windmill vary as a function of the simulated wind velocity. However, in an actual windmill C_{w1} and C_{w2} are constants. Thus, in terms of power losses a dc motor does not accurately simulate a windmill. This inaccuracy can, however, be considered negligible since the power losses associated with these variations in C_{w1} and C_{w2} correspond to only a very small percentage of the motor's air gap power.

To determine the value of P_{RW} in Eq. 26, Section II.1, values for C_{w1} and C_{w2} under rated system conditions are required. At rated wind velocity Eq. D.14 becomes

$$C_{w1} = 0.085$$
$$C_{w2} = 0.13 \quad ; v_w = 1 \qquad \text{(D.15)}$$

Equation D.15 can now be substituted into Eq. 26 to determine P_{RW}. Once P_{RW} is known, a value for R_a, the lumped sum of internal and external motor armature resistances, can be determined from Eq. D.8. With R_a known, the windmill simulation on the dc motor becomes complete.

APPENDIX E

GENERATOR POWER LOSS MEASUREMENTS

The purpose of this appendix is to determine all the power losses associated with the generator employed in the physical scale model simulation of the windmill power system. These loss measurements are used to determine values for the loss coefficients and effective armature resistance modeled in Equations 11 through 14 of Section I.2.d.

Three power loss mechanisms associated with the generator are considered in this appendix. These loss mechanisms are 1) mechanical power losses, 2) magnetic-core power losses, and 3) stray losses.

E.1 Mechanical Power Losses

Figure E.1 shows the results of no-load torque-speed measurements made for the generator. The data points in Figure E.1 were determined by measuring the power into the motor with the motor's shaft coupled to the generator. The power losses associated with the motor (see Appendix D) were then subtracted from this measurement yielding the mechanical losses associated with the generator shaft and motor-generator coupling system. (The latter power losses are considered negligible since no gearing system was necessary in coupling the motor and generator.) Lastly, calculating the quotient of these mechanical losses and the shaftspeed at which the loss measurements were obtained, resulted in the torque-speed values plotted in Figure E.1. Base quantities are obtained from Table B.2.

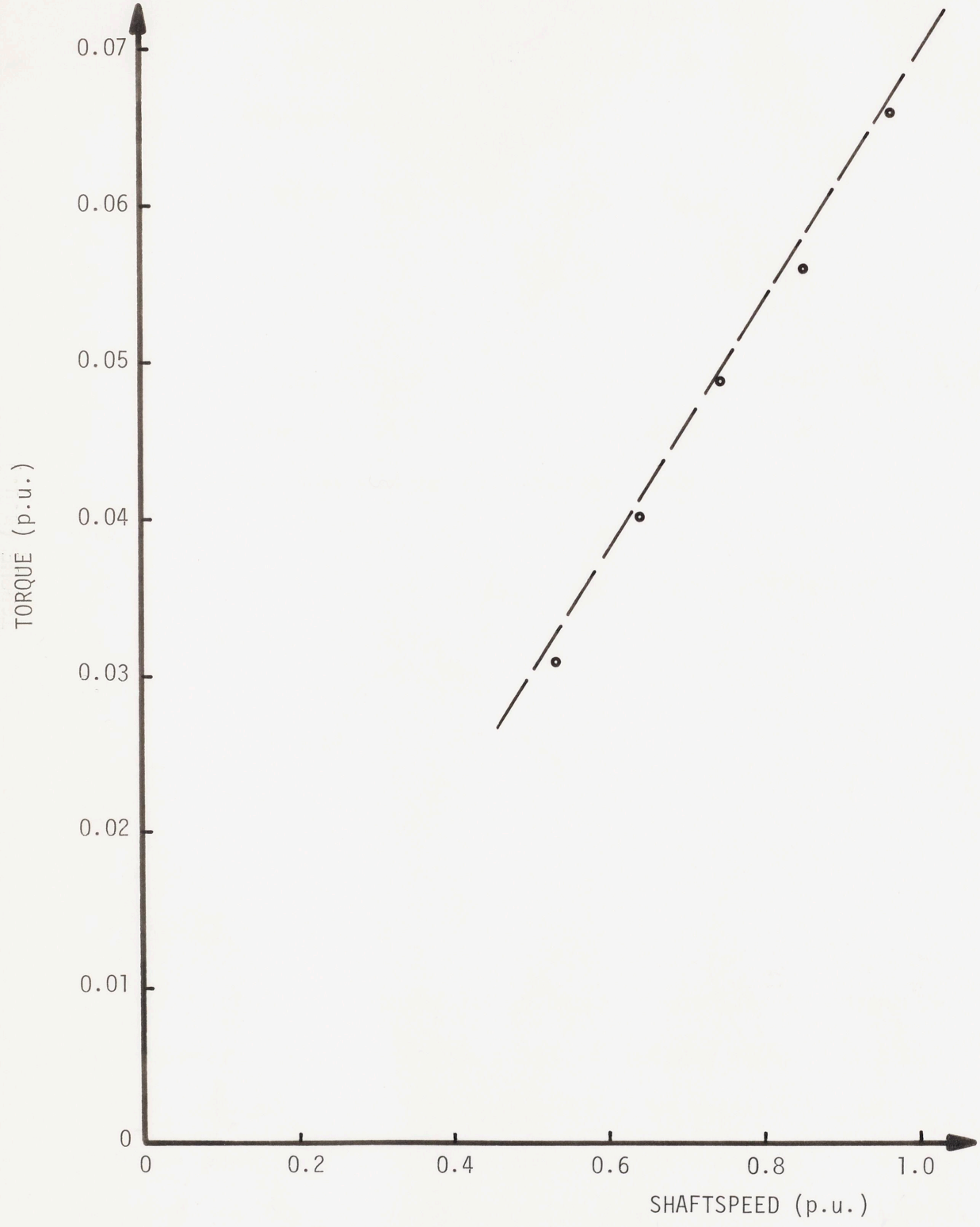

Figure E.1 No-Load Generator Torque-Speed Characteristic

A straight line was fitted to the measured values in Figure E.1, resulting in the following equation relating generator mechanical power losses to generator shaftspeed:

$$\text{Generator Mechanical Power Losses} \equiv P_{\ell gm}$$

$$= - 0.01\ \omega_s + 0.08\ \omega_s^2 \qquad \text{(E.1)}$$

The form of Eq. E.1 predicts negative power losses at low enough shaftspeeds. However, this equation is only considered valid in that shaftspeed range where the measurements were taken, i.e., $0.5 < \omega_s < 1.0$ from Figure E.1.

Relating Eq. E.1 to the mechanical-power-loss coefficients defined in Eq. 11 (Section I.2.d) results in

$$C_{g1} = - 0.01$$

$$C_{g2} = 0.08 \qquad \text{(E.2)}$$

E.2 Magnetic-Core Losses

Figure E.2 shows the results of measurements made to determine the generator core power losses. These losses are plotted as a function of the square of the flux level within the machine for two different generator shaftspeeds. The values were obtained by noting the power into the coupled generator and motor as a function of generator field excitation. From this result the measured losses of the motor and the measured mechanical losses of the generator were

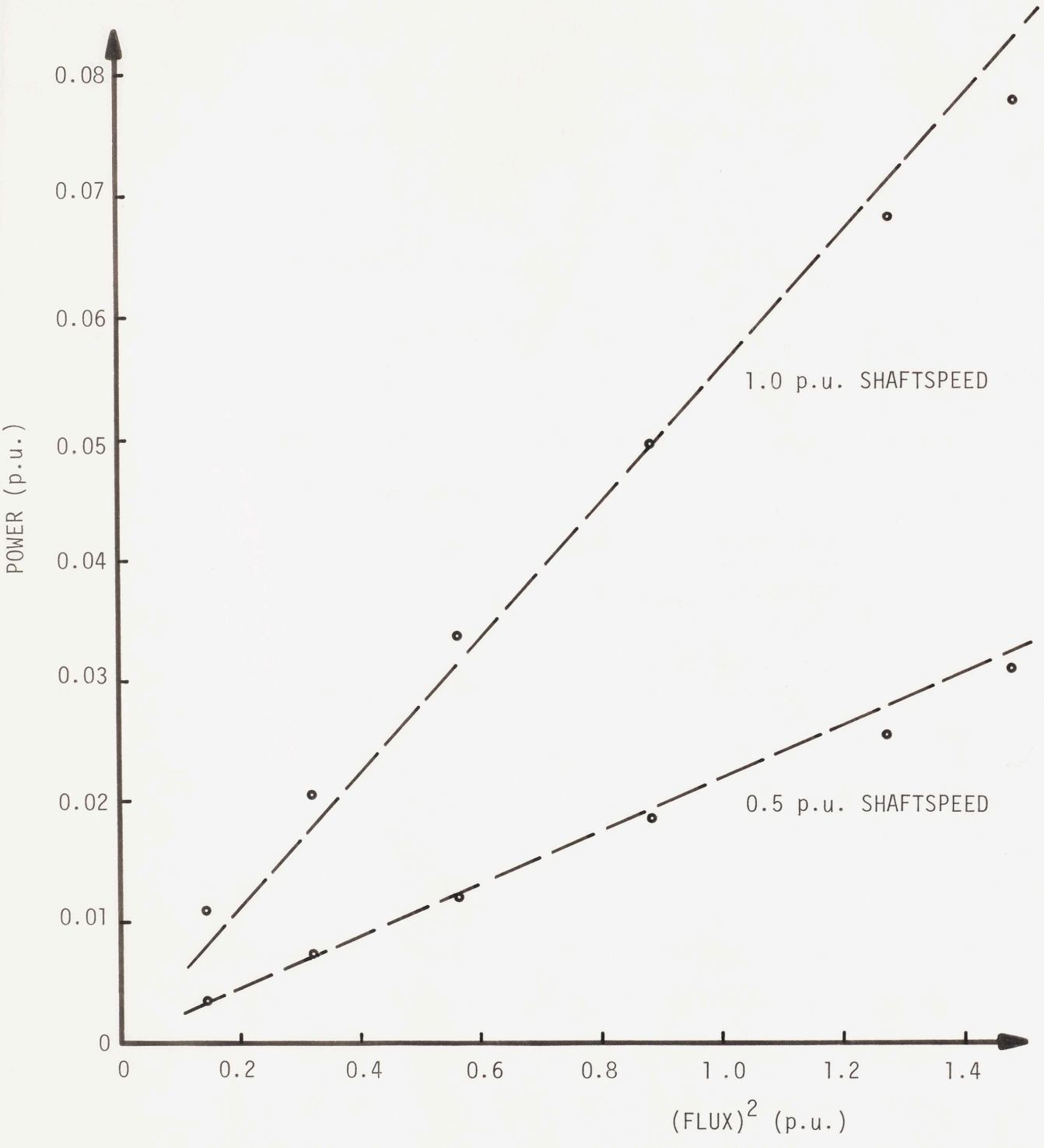

Figure E.2 Generator Core Losses as a Function of the Square of Generator Field Flux Level

subtracted yielding only those losses associated with the generator core. Using the magnetic-core loss model described in Section I.2.d, the following equation can be fitted to the measured losses of Figure E.2

$$\text{Generator-Core Power Losses} \equiv P_{\ell gc} = P_{\ell e} + P_{\ell h}$$

$$= 0.025\phi^2\omega_s^2 + 0.03\phi^2\omega_s \qquad \text{(E.3)}$$

Eq. E.3 is plotted in Figure E.2 to show the correlation between this equation and the measured losses.

Relating the coefficients in Eq. E.3 to the coefficients defined in Eqs. 12 and 13 yields

$$C_e = 0.025$$

$$C_h = 0.03 \qquad \text{(E.4)}$$

E.3 Stray Losses

As discussed in Section I.2.d, stray losses are the result of both nonuniform current distributions in the copper windings of the machine and core losses produced by the distortion of the magnetic flux wave when the machine is under electrical load. These losses are difficult to determine accurately. However, they can be estimated by performing a short-circuit load test on the generator.

The constraints imposed by the charging circuit produce an armature current with a high harmonic component, i.e., the armature

current waveform is approximately a square wave. These harmonics result in additional stray losses in the machine. With this consideration, the short-circuit test was conducted by shorting the battery side of the rectifier bridge circuit with the smoothing choke remaining in the circuit. The stray loss was measured by noting the power into the motor during the generator short-circuit test. Subtracted from this motor power input were the no-load losses associated with both the motor and generator. (The core loss caused by the resultant magnetic flux in the generator is neglected.) Also subtracted from the motor's input power were both the power losses associated with the charging circuit, i.e., both rectifier power losses and I^2R losses in the smoothing choke, and the power losses associated with the generator armature resistance. The result is the power loss attributed to generator stray losses. This loss can be modeled as a resistive component in the generator armature circuit. This stray-loss resistance is calculated by taking the quotient of the measured stray loss and the square of the armature current when the short-circuit test was performed.

The results of the stray-loss measurements are shown in Figure E.3. In this figure, the calculated stray-loss resistance is plotted as a function of the shaftspeed at which the short-circuit test was conducted. Note the approximate linear relationship between stray-loss resistance and shaftspeed. Thus, this resistance can be approximately modeled as

$$\text{Stray-Loss Resistance} \equiv R_{ST} \simeq 0.03\,\omega_s \qquad \text{(E.5)}$$

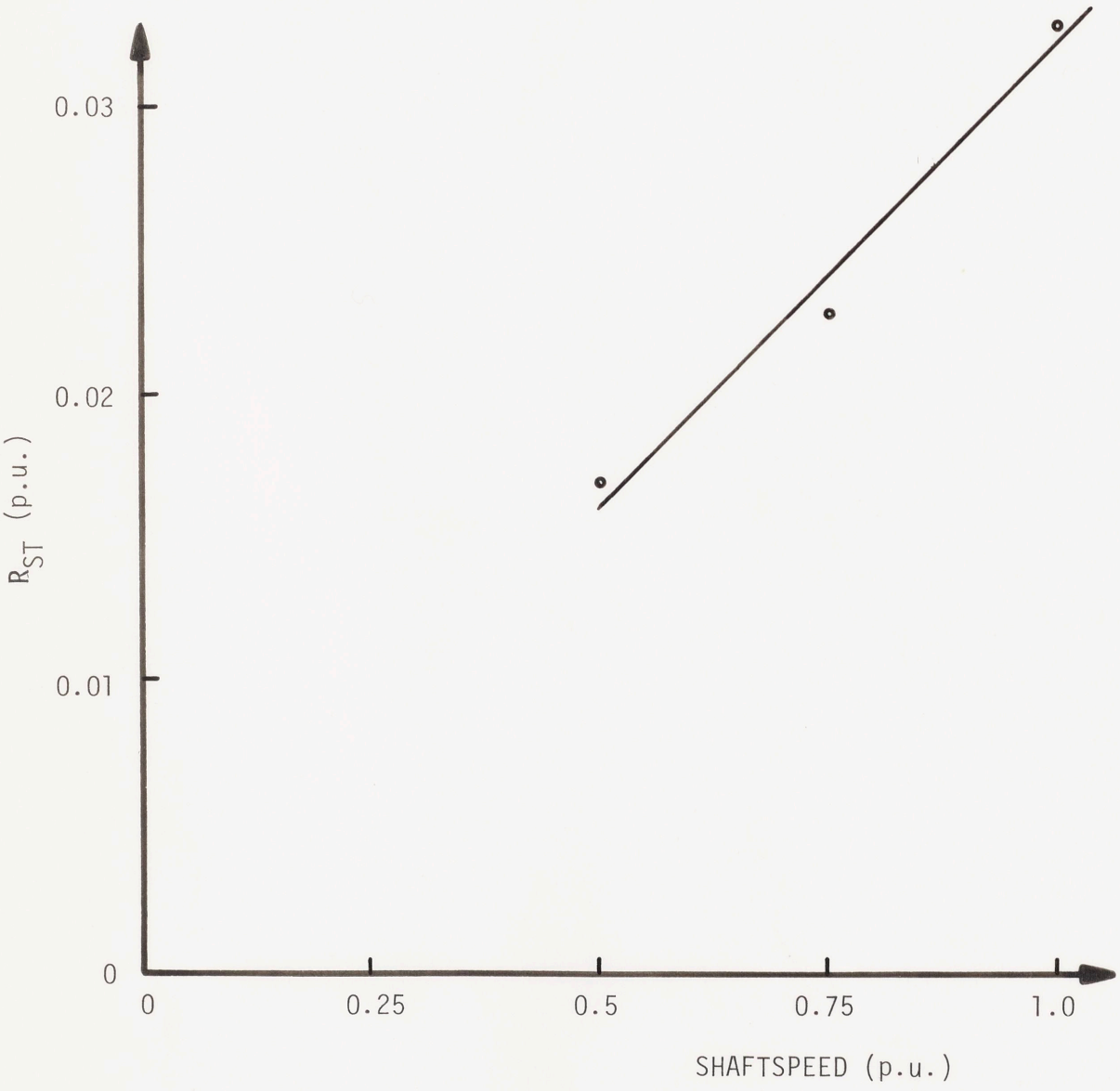

Figure E.3 Equivalent Generator Stray-Loss Resistance as a Function of Shaftspeed.

Insufficient variation in stray-loss resistance as a function of armature current was noted to warrent modeling this dependence.

APPENDIX F

DYNAMIC SYSTEM COMPUTER SIMULATION

The purpose of this appendix is to present the digital computer program employed in the dynamic simulation of the windmill power system. The dynamic model was presented in Section II.3 and is shown in Figure 14. The model is simulated for the physical scale model system described in Appendices B through E.

The computer program used in this dynamic simulation is shown at the end of this appendix. The computing procedure employed is Dynstart which performs a first-order Runge-Kutta integrating routine. The language used is Dynamo II.[4] The variables employed in the computer program do not exactly correspond to the variables described in the text. Thus Table F.1 has been created to relate the program variables to the variables in the text. For convenience, a description of each variable is also given in Table F.1. Note that all variables in the program are per-unit variables with base quantities given in Table B.2.

Present in the computer program is the inertia model developed in Section II.3 (Eq. 38). Components of this model are wind power extraction, generator power output and all windmill and generator power losses. These power components are shown in Eq. 35. Since, in the physical simulation, a dc motor is used instead of an actual windmill, the magnetic-core power losses associated with the motor have been added into the program equations that model mechanical losses in the system. Appendix D showed that this motor component of the power losses can be modeled as being proportional to wind speed (see Eq. D.12).

The system H constant (I in program) was calculated by measuring the shaftspeed profile as the coupled motor-generator slowed down from rated shaftspeed under the influence of mechanical power losses alone. The speed profile was then analytically approximated and weighted by the mechanical power loss equations (sum of Eqs. 3 and 11). The resulting function was then integrated over time to determine the kinetic energy of the shaft at rated shaftspeed. The quotient of this result and base generator power then determines the H constant of the machine.

The "generator electrical output" equations in the program are simply Eqs. 7, 8 and 9 in the text. The battery characteristic" equations are given by Eq. 36 where VSOC[ε_1] and RSOC[ε_2] are obtained from Figure C.1.* The "wind characteristics" simulate steady-state and dynamic wind speed profiles. The dynamic profiles include a ramp, a step and an oscillating wind speed component. The "field current control" equations simulate the three modes of generator field current control, shown schematically in Figure 14 and described in the related text. The calculation of desired shaftspeed, i.e., WSO[ω_{so}], was described in Section IV.1.a.

Initiating a change in field current time constant, TF[τ_f], at the occurrence of battery voltage switching is achieved by the "field

*The variables in brackets correspond to the variables in the text. The variables not in brackets correspond to the variables in the program.

current time constant control" equations. Immediately after battery voltage switching, these equations in the program cause a change in value of field current time constant from TF2 to TF1 for a duration of time given by TFCT.

Lastly, the "battery section control" equations implement the battery voltage switching algorithms described in Section IV.1.b.

TABLE F.1

DESCRIPTION OF COMPUTER PROGRAM VARIABLES AND THEIR RELATION TO VARIABLES USED IN THE TEXT

Program Variable	Text Variable	Description
B	P_{RW}[or b]	Maximum wind-power extraction at rated wind velocity.
C1	C_1	Loss coefficient associated with motor eddy-current power losses.
C2	C_2	Loss coefficient (motor hysteresis power losses).
C3	$C_{w1} + C_{g1}$	Loss coefficients (motor and generator mechanical power losses).
C4	$C_{w2} + C_{g2}$	
CE	C_e	Loss coefficient (generator eddy-current power losses).
CH	C_h	Loss coefficient (generator hysteresis power losses).
EF	E_f	Internal generator voltage.
F	ϕ	Generator field flux level.
I	$\frac{1}{2}J \frac{\omega_{s(base)}^2}{P_{t(base)}}$	H constant of machine.
IAFD	$\lvert i_t \rvert$	Generator rms armature current (fundamental component).
IARMS	None	Actual generator rms armature current.
IB	i_b	Battery charging current.
IF	i_f	Generator field current.
IFIN	i_{fs}	Switching-point field current.
IFM	i_{fm}	Maximum field current.

TABLE F.1 (Continued)

Program Variable	Text Variable	Description
NS	M	Number of charging battery sections.
PE	P_t	Generator electric power output.
PL	None	System power losses (windmill and generator).
PLG	None	Generator power losses (not including mechanical).
PLGC	$P_{\ell gc}$	Generator core losses.
PLGSR	None	Stray power losses.
PLWM	$P_{\ell wm} + P_{\ell gm}$	Windmill and generator mechanical losses.
PM	P_{ext}	Wind power extraction.
RA	R_a	Generator armature winding resistance.
RB	R_{BM}	Internal battery resistance of M battery sections.
RBO	$R_{BS(NOM)}$	Nominal internal battery section resistance.
REFF	R_{eff}	Effective armature resistance.
RS	R_S	Smoothing choke resistance.
RSOC	ε_2	Variation in battery section resistance as a function of battery state-of-charge.
RST	$R_{st}(\omega_s = 1)$	Equivalent stray-loss resistance at rated shaftspeed.

TABLE F.1 (Continued)

Program Variable	Test Variable	Description
SOC	soc	Battery state-of-charge variable.
TA	τ_{ac}	Armature current limiter time constant.
TF	τ_f	Field current time constant.
VB	V_{BM}	Internal battery voltage of M battery sections.
VBO	$V_{BS(NOM)}$	Nominal internal battery section voltage.
VD	$4v_d$	Diode voltage drops.
VSOC	ε_1	Variation in battery section voltage as a function of battery state-of-charge.
VTG	$\|v_t\|$	Generator rms terminal voltage.
VW	v_w	Wind velocity
W	ω_s^2	Square of shaftspeed.
WS	ω_s	Shaftspeed.
WSO	ω_{so}	Desired shaftspeed operating point.
WSS	ω_{ss}	Switching-point shaftspeed.
X	X	Generator armature winding reactance.

WINDMILL DYNAMIC SIMULATION

```
          NOTE      WINDMILL2
NOTE
NOTE   WINDMILL SYSTEM EQNS
NOTE
NOTE    INERTIA MODEL EQN
L         W.K=W.J+DT*PP.JK/I
C         I=2
A         WS.K=SQRT(W.K)
R         PP.KL=PM.K-PE.K-PL.K
NOTE    WIND POWER EXTRACTION EQN
A         PM.K=PMMM.K
A         PMMM.K=MAX(0,PMM.K)
A         PMM.K=B*VW.K((2*VW.K*WS.K)-(WS.K*WS.K))
C         B=1.43
NOTE
NOTE   SYSTEM POWER LOSSES
NOTE
A         PL.K=PLWM.K+PLG.K
NOTE   MECHANICAL LOSSES
A         PLWM.K=(G1.K*WS.K)+(G2.K*WS.K*WS.K)
A         G1.K=(C2*VW.K)+C3
A         G2.K=(C1*VW.K)+C4
C         C1=.09
C         C2=.04
C         C3=.035
C         C4=.12
NOTE   GENERATOR LOSSES
A         PLG.K=PLGC.K+PLGSR.K
NOTE    CORE LOSSES
A         PLGC.K=(CE*WS.K+CH)(F.K*F.K*WS.K)
C         CE=.026
C         CH=.030
A         F.K=TABHL(FX,IF.K,0,1.5,.25)
T         FX=0,.31,.58,.82,1.0,1.14,1.23
NOTE    I2R + STRAY LOSSES
A         PLGSR.K=REFF.K*IARMS.K*IARMS.K
A         REFF.K=RA+RST*WS.K
C         RA=.03
C         RST=.03
NOTE
NOTE   GENERATOR ELECTRICAL OUTPUT EQNS
NOTE
A         PE.K=MAX(.0001,VTG.K*IAFD.K)
A        VTG.K=SQRT(EF.K*EF.K-X.K*X.K*IAFD.K*IAFD.K)-REFF.K*IARMS.K
A         IAFD.K=IB.K
A         IARMS.K=1.11*IB.K
A         X.K=TABHL(XA,IF.K,0,1.5,.5)*WS.K
T         XA=.7,.7,.62,.5
A         EF.K=MAX(0,F.K*WS.K)
A         IB.K=MAX(0,IBB.K)
```

WINDMILL DYNAMIC SIMULATION (Continued)

```
A           IBB.K=(-VBD.K*RX.K+SQRT(VX.K))/RSX.K
A           VX.K=MAX(0,VXX.K)
A           VXX.K=EF.K*EF.K*RSX.K-VBD.K*VBD.K*X.K*X.K
A           RSX.K=RX.K*RX.K+X.K*X.K
A           VBD.K=VB.K+VD
A           RX.K=1.235*REFF.K+(RS+RB.K)
C           RS=.03
C           VD=.03
NOTE
NOTE   BATTERY CHARACTERISTIC EQNS
NOTE
A           VB.K=(VBO+VSOC.K)*NS.K
C           VBO=.455
A           VSOC.K=TABHL(VO,SOC,0,1,.25)
T           VO=-.035,-.025,-.015,.005,.03
A           RB.K=(RBO+RSOC.K)*NS.K
C           RBO=.015
A           RSOC.K=TABHL(RO,SOC,0,1,.25)
T           RO=.015,0,0,0,.075
C           SOC=.7
NOTE
NOTE   WIND CHARACTERISTICS
NOTE
A           VW.K=VWND+RAMP(SLP,STRT)+STEP(HGT,TM)+SIN(TI.K)*AP
C           AP=0
L           TI.K=TI.J+DT*TIM.JK
R           TIM.KL=TIMM.K
A           TIMM.K=TME
C           TME=1
N           TI=0
C           VWND=0
C           SLP=0
C           STRT=0
C           HGT=0
C           TM=0
NOTE
NOTE   FIELD CURRENT CONTROL
NOTE
L             IF.K=IF.J+DT*IFCLT.JK
NOTE    FIELD CURRENT LIMIT
R             IFCLT.KL=CLIP(IFCA.K,IFC.K,1.5,IF.K)
A             IFC.K=(1.5-IF.K)/DT
NOTE    BATTERY CURRENT LIMIT
A             IFCA.K=CLIP(IFCD.K,IFCE.K,IB.K,1)
A             IFCD.K=(1-IB.K)/TA
C             TA=.1
NOTE    THEORETICAL MAXIMUM AVAILABLE POWER CONVERSION CRITERION
A             IFCE.K=(WS.K-WSO.K)/TF.K
A             WSO.K=WV*VW.K
C             WV=.82
```

WINDMILL DYNAMIC SIMULATION (Continued)

```
NOTE    FIELD CURRENT TIME CONSTANT CONTROL
L         TFC.K=TFC.J+DT*CTFC.JK+CHN.J
R         CTFC.KL=-TFC.K/TFCT
C         TFCT=.5
A         TF.K=CLIP(TF1,TF2,TFCC.K,EXP(-1))
A         TFCC.K=CLIP(TFC.K,-TFC.K,TFC.K,0)
C         TF1=.05
C         TF2=1
N         TFC=0
NOTE
NOTE   BATTERY SECTION CONTROL
NOTE
L         NS.K=NS.J+DT*CN.JK
R         CN.KL=CHN.K/DT
NOTE   BATTERY SECTION INCREMENT:
NOTE    MAXIMUM BATTERY CURRENT CRITERION
A         CHN.K=CLIP(CA.K,CHAN.K,IB.K,1)
NOTE    FIELD CURRENT CRITERION
A         CA.K=CLIP(0,1,IF.K,IFIN)
C         IFIN=.875
NOTE   BATTERY SECTION DECREMENT:
NOTE    MAXIMUM FIELD CURRENT CRITERION
A         CHAN.K=CLIP(CNS.K,0,IF.K,IFM)
C         IFM=1.49
NOTE    SHAFTSPEED CRITERION
A         CNS.K=CLIP(0,-1,WS.K,WSS)
C         WSS=.825
NOTE
NOTE   INITIALIZATION AND CONTROL CARDS
N         W=WI
C         WI=0
N         IF=IFI
C         IFI=0
N         NS=NSI
C         NSI=0
C         DT=.1
C         PLTPER=.2
C         LENGTH=0
PLOT      VW=V/WS=W/IF=I
RUN
OF DATA
```

APPENDIX G

SMOOTHING CHOKE INDUCTANCE CALCULATION

The purpose of this appendix is to calculate an acceptable value for the inductance of the smoothing choke in the battery charging circuit. The objective is to maintain both low ripple in the charging current and rapid current reduction when the SCR's in the bridge rectifier are turned off. Figure 31 shows the battery charging circuit with all resistances removed. However, since only an approximate value for the choke inductance is desired, the circuit of Figure 31 will be further simplified by removing the generator armature inductance. The resulting circuit is remodeled in Figure G(a). In this circuit, the battery bank and diode voltage drops have been replaced by a single voltage source, V_B. Also the input waveform, e_f, to the charging circuit is now just the full-wave rectified voltage of the generator armature terminals. e_f is shown in Figure G(b). Lastly, the switch, SW, simulates the "turning on" and "turning off" of the bridge rectifier.

From Figure G(a) the battery charging current waveform, i_b, can be calculated. With switch SW closed i_b can be calculated from

$$\frac{di_b}{dt} = \frac{\hat{E}_f \sin\omega_e t - V_B}{L_S} \quad ; \quad 0 \leq t \leq \frac{\pi}{\omega_e} \tag{G.1}$$

where $\hat{E}_f$ is the peak value of e_f, L_S is the inductance of the smoothing choke in the circuit and ω_e is the frequency of the generator armature terminal voltage. Under steady-state conditions no average voltage

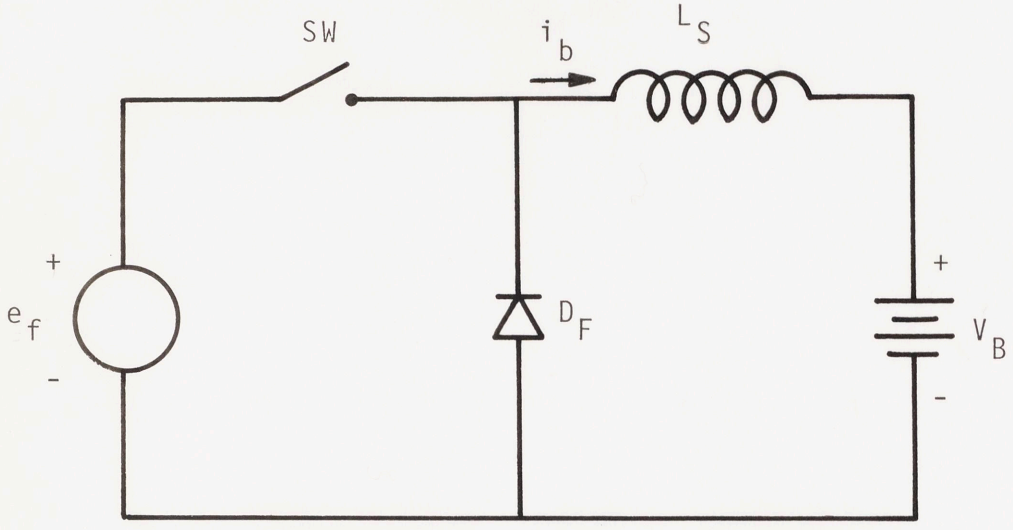

(a)

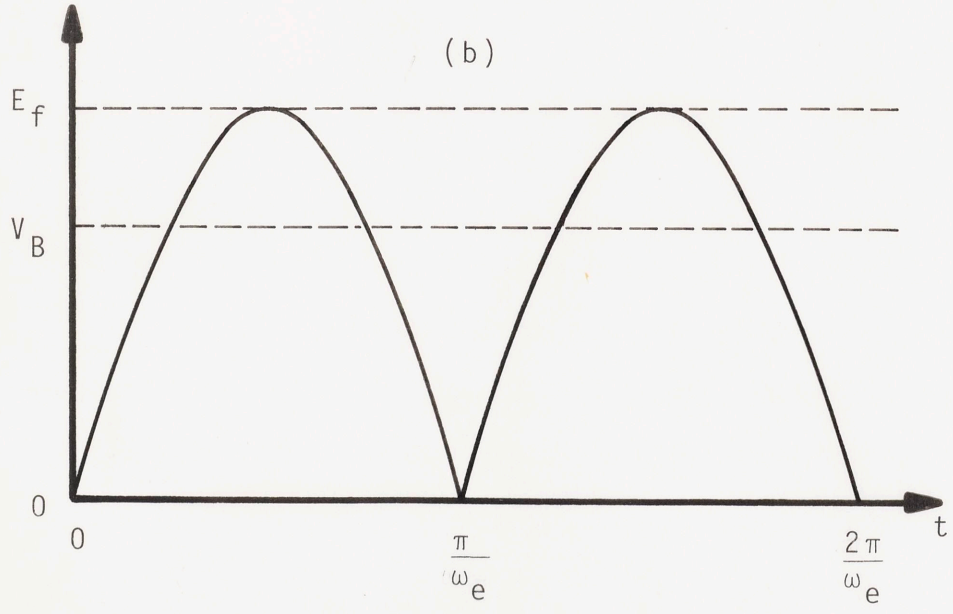

Figure G Remodeled Charging Circuit and Input Waveform

exists across L_S resulting in $< e_f > = V_B$, where $< e_f >$ is the average value of e_f. Since the average value of a full-wave rectified sine wave is $2/\pi$ times its peak value,

$$< e_f > = \frac{2\hat{E}_f}{\pi} = V_B$$

$$\text{or} \quad \hat{E}_f = \frac{\pi V_B}{2} \tag{G.2}$$

Substituting Eq. G.2 into Eq. G.1 and solving for i_b yields

$$i_b = -\frac{V_B}{L_S}\left(\frac{\pi}{2\omega_e}\cos \omega_e t + t\right) + C \quad ; \; 0 \leq t \leq \frac{\pi}{\omega_e} \tag{G.3}$$

where C is a constant of integration. Finding the average value of i_b and setting that value to a constant, i_o, results in $C = i_o + \pi V_B/2\omega_e L_S$. Substituting this value of C into Eq. G.3 yields

$$i_b = \frac{\pi V_B}{2\omega_e L_S}(1 - \cos \omega_e t) - \frac{V_B t}{L_S} + i_o \quad ; \; 0 \leq t \leq \frac{\pi}{\omega_e} \tag{G.4}$$

To find the ripple in i_b requires finding the maximum and minimum values of i_b. From differentiating Eq. E.4 and setting the result to zero the location of the extrema of i_b are found. Employing the second derivative test to find which extrema are maxima and which are minima yields

maximum of i_b at: $t = (\pi - \sin^{-1}(\frac{2}{\pi}))/\omega_e \simeq 2.45/\omega_e$

minimum of i_b at: $t = \sin^{-1}(\frac{2}{\pi})/\omega_e \simeq 0.69/\omega_e$

Substituting the above results into Eq. G.4 yield the maximum and minimum values of i_b, i.e., $i_{b(max)}$ and $i_{b(min)}$, respectively.

$$i_{b(max)} \simeq \frac{0.33V_B}{\omega_e L_S} + i_o \tag{G.5}$$

$$i_{b(min)} \simeq i_o - \frac{0.17V_B}{\omega_e L_S} \tag{G.6}$$

The ripple in i_b is the quotient of the difference between maximum and minimum values of i_b and the average current, i_o. Thus,

$$\text{Ripple in } i_b \equiv R_i = \frac{i_{b(max)} - i_{b(min)}}{i_o} \tag{G.7}$$

$$\simeq \frac{0.5V_B}{\omega_e L_S i_o}$$

where Eqs. G.5 and G.6 have been used.

The inductance L_S in Eq. G.7 has been chosen to limit R_i to 15% under rated generator operation and rated battery load. These rated conditions are given in Appendix B and are

V_B = Full Nominal Battery Voltage + Diode Voltage Drops $\simeq$ 115V

i_o = Rated Battery Charging Current = 17.4A

ω_e = Generator Armature Voltage Frequency at Rated Shaftspeed $\simeq 26.2 \times 10^2$ sec^{-1}

Substituting these values and $R_1 = 0.15$ into Eq. G.7 and solving for L_S yields $L_S \simeq 8.5$mH.

Now that L_S has been chosen, the decay time of the charging current after bridge "turn off" can be calculated. Figure G(a) shows that when switch SW is open the charging current commutates to the free wheeling diode, D_F, and then decays linearly to zero due to the back emf of the battery. This decay time, defined as τ_d, can be calculated from $V_B = L_S \frac{di_b}{dt}$ with initial conditions $i_b(t = 0) = i_{bo}$, where switch SW has been opened at t = 0. Therefore,

$$\tau_d = \frac{L_S i_{bo}}{V_B} \qquad (G.8)$$

The largest value for τ_d occurs during battery sections rotation when the charging current is at rating. In this case, i_{bo} is approximately the rated average charging current and V_B is half the rated battery voltage. Using the value for these quantities cited above and using the value of L_S claculated above yield $\tau_d = 2.6$msec or, under these conditions, approximately two cycles of the armature current waveform (see test results, Figure 34 in text). This decay time is acceptable to "good" system performance since it results in minimal shaft dynamics during the times that the generator's power output is reduced to zero, i.e., when battery charging current is removed.

REFERENCES

1. Harvey R. Simkovits, "Control of a Variable Shaftspeed Electromechanical Energy Conversion System", S.B. Thesis, Massachusetts Institute of Technology, June 1976.

2. Harvey R. Simkovits and John G. Kassakian, "Control and Dynamic Analysis of a Wind Energy Conversion and Storage System Operating at Constant Velocity Ratio," Energy Development III, IEEE Power Engineering Society Papers, 1977, 77CH1215-3-PWR, pp. 48-55.

3. Fitzgerald and Kingsley, Electrical Machinery, McGraw-Hill Inc., 1961.

4. Alexander L. Pugh III, Dynamo II User's Manual, Fourth Edition, The MIT Press, 1973.